UCTEA Turkish Chamber of Civil Engineers
TMMOB İnşaat Mühendisleri Odası

Turkish Journal of Civil Engineering

formerly
Teknik Dergi

Volume 35
Issue 6
November 2024

Turkish Journal of Civil Engineering (formerly Teknik Dergi) Publication Principles

Turkish Journal of Civil Engineering (TJCE), a non-profit, open access scientific and technical periodical of UCTEA Chamber of Civil Engineers, publishes papers reporting original research work and major projects of interest in the area of civil engineering. TJCE annually publishes six issues and is open to papers in English and Turkish. It should be noted that TJCE (formerly, Teknik Dergi/ Technical Journal of Turkish Chamber of Civil Engineers) is being published regularly for more than 30 years since 1990. Main publication principles of TJCE are summarized below:

1. Articles reporting original scientific research and those reflecting interesting engineering applications are accepted for publication. To be classified as original, the work should either produce new scientific knowledge or add a genuinely new dimension to the existing knowledge or develop a totally new method or substantially improve an existing method.
2. Articles reporting preliminary results of scientific studies and those which do not qualify as full articles but provide useful information for the reader can be considered for publication as technical notes.
3. Discussions received from the readers of the published articles within three months from publication are reviewed by the Editorial Board and then published together with the closing remarks of the author.
4. Manuscripts submitted for publication are evaluated by two or three reviewers unknown to the authors. In the light of their reports, final decision to accept or decline is taken by the Editorial Board. General policy of the Board is to get the insufficient manuscripts improved in line with the reviewers' proposals. Articles that fail to reach the desired level are declined. Reasons behind decisions are not declared.
5. A signed statement is taken from the authors, declaring that the article has not been published as a "journal article or book chapter". In case the Editorial Board is in the opinion that the article has already been published elsewhere with minor changes or suspects plagiarism or a similar violation of ethics, then not only that article, but none of the articles of the same authors are published.
6. Papers reporting works presented as conference papers and developed further may be considered for publication. The conference it was presented to is given as a footnote in the first page.
7. Additionally, a document signed by all authors, transferring the copyright to UCTEA Chamber of Civil Engineers is submitted together with the manuscript.

UCTEA Turkish Chamber of Civil Engineers
TMMOB İnşaat Mühendisleri Odası

Turkish Journal of Civil Engineering

formerly
Teknik Dergi

Volume 35
Issue 6
November 2024

UCTEA Turkish Chamber of Civil Engineers
TMMOB İnşaat Mühendisleri Odası
Necatibey St. No: 57, Kızılay 06440 Ankara, Turkey
Tel: +90.312.294 30 00 - Faks: +90.312.294 30 88
E-mail: imo@imo.org.tr - www.imo.org.tr

Publisher *(Sahibi)*:
Nusret SUNA
On behalf of UCTEA Turkish Chamber of Civil Engineers

Administrative Officer *(Yazı İşleri Müdürü)*:
Bülent TATLI

Volume 35 - Issue 5 - November 2024 *(Cilt 35 - Sayı 6 - Kasım 2024)*
Published bi-monthly. Local periodical. *(İki ayda bir yayınlanır, yerel süreli yayın)*
Date of Print: November 1, 2024 *(Baskı Tarihi: 1 Kasım 2024)*

ISSN: 2822-6836

Turkish Journal of Civil Engineering (formerly Teknik Dergi) is indexed by

- Science Citation Index Expanded
- Scopus
- Journal Citation Reports / Science Edition
- Engineering Index
- Concrete Abstracts (American Concrete Institute)
- National Technical Information Service (US NTIS)
- CITIS
- Ulrich's International Periodical's Directory
- Google Scholar
- TR Index

Turkish Journal of Civil Engineering (formerly Teknik Dergi) is a peer reviewed open access periodical publishing papers of original research and interesting practice cases. It addresses both the research community and the practicing engineers.

Printed by *(Baskı)*:
Ankamat Matbaacılık San.
İvedik OSB. 1344. Sok. Yenimahalle / Ankara - Tel: 0.312.394 54 64
Sertifika No: 46700

Reviewers:

This list is renewed each year and includes reviewers who served in the last two years of publication.

Şükran AÇIKEL
Kamil Bekir AFACAN
Bülent AKBAŞ
Sami Oğuzhan AKBAŞ
Zülal AKBAY ARAMA
Rıfat AKBIYIKLI
Sarven AKCELYAN
Burcu AKÇAY ALDANMAZ
Cihan Taylan AKDAĞ
Bekir AKGÖZ
Cem AKGÜNER
Fevziye AKÖZ
Erkan AKPINAR
Muhammet Vefa AKPINAR
Atakan AKSOY
Hafzullah AKSOY
Tülay AKSU ÖZKUL
Uğurhan AKYÜZ
Alper ALDEMİR
Cenk ALHAN
Gülay ALTAY
Sinan ALTIN
Adlen ALTUNBAŞ
Yalçın ALVER
Mustafa M. ARAL
Davit ARDITI
Yalın ARICI
Deniz ARTAN İLTER
Deepankar Kumar ASHISH
Ayşegül ASKAN GÜNDOĞAN
Ali Osman ATAHAN
Hakan Nuri ATAHAN
Güzide ATASOY ÖZCAN
Ali Osman ATEŞ
Özgür AVŞAR
Cem AYDEMİR
Metin AYDOĞDU
Ülker Güner BACANLI
Selim BARADAN
Eray BARAN
Özgür Uğraş BARAN
Türkay BARAN
Efe BARBAROS
Bekir Oğuz BARTIN
Zeynep BAŞARAN BUNDUR
Mustafa Gökçe BAYDOĞAN
Cüneyt BAYKAL
Mehmet BERİLGEN
Katrin BEYER
Niyazi Özgür BEZGİN
Ozan BİLAL
Senem BİLİR MAHÇİÇEK
İlknur BOZBEY
Ali BOZER
Mehmet Bakır BOZKURT
Zafer BOZKUŞ
Zekai CELEP
Cihan CENGİZ
Halim CEYLAN
Joao Ramoa CORREIA
Ali Fırat ÇABALAR
Barlas Özden ÇAĞLAYAN
Ferit ÇAKIR
Melih ÇALAMAK
Gülben ÇALIŞ
Umut ÇALIŞKAN
Süheyla Pelin ÇALIŞKANELLİ
Mehmet Alper ÇANKAYA
Serdar ÇARBAŞ
Dilay ÇELEBİ
Tevfik Kutay ÇELEBİOĞLU
Ahmet Ozan ÇELİK
Oğuz Cem ÇELİK
Ozan Cem ÇELİK
Hilmi Berk ÇELİKOĞLU
Kemal Önder ÇETİN
Mecit ÇETİN
Elif ÇİÇEK
Emin ÇİFTÇİ
Hüseyin ÇİLSALAR
Erdal ÇOKÇA
Semra ÇOMU
Turgay ÇOŞGUN
Atilla DAMCI
Yakup DARAMA
Kutlu DARILMAZ
Tayfun DEDE
Cem DEMİR
Selçuk DEMİR
Uğur DEMİR
Ender DEMİREL
Mehmet Cüneyd DEMİREL
Murat DİCLELİ
Seyyit Ümit DİKMEN
Ahmet Anıl DİNDAR
Mustafa DOĞAN
Marco DOMANESCHİ
Gökhan DÖK
Cemalettin DÖNMEZ
İsmail DURANYILDIZ
Cengiz DÜNDAR
Nurhan ECEMİŞ ZEREN
Özgür EKİNCİOĞLU
Serkan ENGİN
Murat Altuğ ERBERİK
Ali ERCAN
Barış ERDİL
Sinan Turhan ERDOĞAN
Şakir ERDOĞDU
Esin ERGEN PEHLEVAN
Yusuf Çağatay ERŞAN
Kağan ERYÜRÜK
Esra Ece ESELLER BAYAT
Tuğba ESKİŞAR TEFÇİ
Burak FELEKOĞLU
Mahmut FIRAT
Onur GEDİK
Abdullah GEDİKLİ
Ergun GEDİZLİOĞLU
Ahmet Talha GEZGİN
Sadık Can GİRGİN
Zehra Canan GİRGİN
Saadet Gökçe GÖK
Tansu GÖKÇE
Serdar GÖKTEPE
Semih GÖNEN
Rahmi GÜÇLÜ
Ali GÜL
Fazlı Erol GÜLER
Ilgın GÜLER
M. Fethi GÜLLÜ
Adil GÜLTEKİN
Fırat GÜMGÜM
Gürkan GÜNAY
Taylan GÜNAY
Murat GÜNAYDIN
Samet GÜNER
Burcu GÜNEŞ
Oğuz GÜNEŞ
Mehmet Şükrü GÜNEY
Tuba GÜRBÜZ BÜYÜKKAYIKÇI
Aslı Pelin GÜRGÜN
Tefarruk HAKTANIR
Soner HALDENBİLEN
Murat HAMDERİ
Ingo A. HANSEN
Umut HASGÜL
Emre HASPOLAT
Mustafa HATİPOĞLU
Lucas HOGAN
Zeynep IŞIK
Sabriye Banu İKİZLER
Okan İLHAN
Erol İSKENDER
Medine İSPİR ARSLAN
Recep İYİSAN
Nuray Işık KABDAŞLI
Volkan KALPAKÇI
Muhammet KAMAL
Reza KAMGAR
Hakan Alper KAMİLOĞLU
Elif Çağda KANDEMİR
Tanay KARADEMİR
Hüseyin Faruk KARADOĞAN
Ümit KARADOĞAN
Mustafa Erkan KARAGÜLER
Halil KARAHAN
Oğuz KAYABAŞI
İlker KAZAZ
Saeid KAZEMZADEH AZAD
Mustafa Kubilay KELEŞOĞLU
Elçin KENTEL
Hadi KHANBABAZADEH
Ufuk KIRBAŞ
Veysel Şadan Özgür KIRCA
Mehmet Anıl KIZILASLAN
Esat Selim KOCAMAN
Salih KOÇAK
Baha Vural KÖK
Mete KÖKEN
Özgür KURÇ
Hasan KURTARAN
Murat KURUOĞLU
Akif KUTLU
Merih KÜÇÜKLER
Abdullah KÜRKÇÜ
Todd LİTMAN
Faqih MAARİF
Müslüm Murat MARAŞ
Halit Cenan MERTOL
Mahmoud MIARI
Mehmet Murat MONKUL
Nihat MOROVA
Yetiş Şazi MURAT
Sepanta NAİMİ
Salih OFLUOĞLU
Fuad OKAY
Didem OKTAY
Derviş Volkan OKUR
Sezan ORAK
Engin ORAKDÖĞEN
Şeref ORUÇ
Okan ÖNAL
Akın ÖNALP
Bihrat ÖNÖZ
Cihan ÖSER
Yiğit ÖZÇELİK
Gökhan ÖZDEMİR
Zuhal ÖZDEMİR
Murat ÖZEN
Pelin ÖZENER
Ekin ÖZER
Hasan ÖZER
Hakkı Oral ÖZHAN
Mehmet Fatih ÖZKAL
Zeynep Huri ÖZKUL BİRGÖREN
Aşkın ÖZOCAK
Sadık ÖZTOPRAK
Turan ÖZTURAN
Gözde Başak ÖZTÜRK
Mustafa ÖZUYSAL
Tolga Yılmaz ÖZÜDOĞRU
Atilla ÖZÜTOK
Nilüfer ÖZYURT ZİHNİOĞLU
Erhan Burak PANCAR
Seval PINARBAŞI ÇUHADAROĞLU
Elişan Filiz PİROĞLU
Bora POLATSU
Shehata E. Abdel RAHEEM
Selçuk SAATÇİ
Selman SAĞLAM
Mehmet SALTAN
Altuğ SAYGILI
Serdar SELAMET
Nuri SERTESER
Halil SEZEN
Alper SEZER
Metin SOYCAN
Kurtuluş SOYLUK
Serdar SOYÖZ
Rifat SÖNMEZ
Tayfun Altuğ SÖYLEV
Haluk SUCUOĞLU
Erol ŞADOĞLU
Yuşa ŞAHİN
Zekai ŞEN
Burak ŞENGÖZ
Gülüm TANIRCAN
Serhan TANYEL
Mucip TAPAN
Ergin TARI
Yüksel TAŞDEMİR
Ali Şahin TAŞLIGEDİK
Hasan TATLI
Gökmen TAYFUR
Serdal TERZİ
Berrak TEYMUR
Hüseyin Onur TEZCAN
Mesut TIĞDEMİR
Salih TİLEYLİOĞLU
Onur Behzat TOKDEMİR
Nabi Kartal TOKER
Ali TOPAL
Cem TOPKAYA
Kamile TOSUN FELEKOĞLU
Gökçe TÖNÜK
Erkan TÖRE
Kemal Dirgen TÖZER
Nursu TUNALIOĞLU
Gürsoy TURAN
Hasan Nuri TÜRKMENOĞLU
Cüneyt TÜZÜN
Eren UÇKAN
Latif Onur UĞUR
Mehmet Baran ULAK
Dilay UNCU
Berna UNUTMAZ
Mehmet UTKU
Volkan Emre UZ
İbrahim Mert UZUN
Deniz ÜLGEN
Mehmet Barış Can ÜLKER
Yurdanur ÜNAL
Ali ÜNAY
Cüneyt VATANSEVER
Ahmet YAKUT
Erkut YALÇIN
Aslı YALÇIN DAYIOĞLU
Mustafa Sinan YARDIM
Anıl YAZICI
Gökhan YAZICI
Halit YAZICI
Cem YENİDOĞAN
Mehmet YETMEZ
İrem Zeynep YILDIRIM
Berivan YILMAZER POLAT
Ercan YÜKSEL
Yeliz YÜKSELEN AKSOY
Ahmet Şahin ZAİMOĞLU
Abdullah Can ZÜLFİKAR

Turkish Journal of Civil Engineering (formerly Teknik Dergi)

Volume 35 Issue 6 November 2024

CONTENTS

RESEARCH ARTICLE

Turkish Journal of Civil Engineering, 2024 1-18, Paper 785, ***Research Article***

Investigation of Rheological and Physical Properties of SBS and WCO Composite Modified Bitumen

Erman ÇAVDAR[1*]
Aytuğ KUMANDAŞ[2]
Neslihan ŞAHAN[3]
Ersoy KABADAYI[4]
Şeref ORUÇ[5]

ABSTRACT

Nowadays, the use of waste materials in various industries is becoming widespread in order to promote waste recycling. Thus, scientists are researching the use of waste materials in bitumen modification. In this study, it was aimed to investigate the effect of waste cooking oil (WCO) on the physical and rheological properties of unaged Styrene-Butadiene-Styrene modified bitumen (SBSMB) by adding WCO at different ratios (1, 3, 5, 7, and 9%) to SBS modified bitumen. Accordingly, rotational viscosity (RV) tests and rheological tests with dynamic shear rheometer (DSR) based on the determination of complex shear modulus (|G*|) and phase angle (δ) were conducted along with the traditional bitumen tests. As a result of the experimental study, it was observed that adding WCO increased the workability and fatigue resistance of SBSMB, however, decreased its rutting resistance. Therefore, the mixing and compaction temperatures of SBSMB can be decreased by adding low amounts of WCO without excessive performance loss. Thus, during the construction of asphalt pavements, environmental damage can be reduced by utilizing waste materials and reducing CO_2 emissions.

Keywords: Styrene-butadiene-styrene, polymer modified bitumen, waste cooking oil, workability, rheology.

Note:
- This paper was received on November 20, 2023 and accepted for publication by the Editorial Board on May 23, 2024.
- Discussions on this paper will be accepted by January 31, 2025.
- https://doi.org/10.18400/tjce.1393363

1 Karadeniz Technical University, Department of Civil Engineering, Trabzon, Türkiye
ermancavdar@ktu.edu.tr - https://orcid.org/0000-0002-0238-5245

2 Ondokuz Mayıs University, Department of Civil Engineering, Samsun, Türkiye
aytug.kumandas@omu.edu.tr - https://orcid.org/0000-0003-1765-9963

3 Kırşehir Ahi Evran University, Department of Civil Engineering, Kırşehir, Türkiye
neslihan.sahan@ahievran.edu.tr - https://orcid.org/0000-0003-3904-6527

4 Giresun University, Department of Construction Technology, Keşap Vocational School, Giresun, Türkiye
ersoy.kabadayi@giresun.edu.tr - https://orcid.org/0000-0003-4062-3117

5 Karadeniz Technical University, Department of Civil Engineering, Trabzon, Türkiye
oruc@ktu.edu.tr - https://orcid.org/0000-0001-5788-890X

* Corresponding author

1. INTRODUCTION

Styrene-butadiene-styrene (SBS) additive is the most commonly used polymer type in bitumen modification. When SBS is added to the base bitumen, the rutting, fatigue and stripping resistance as well as the elasticity and viscosity of the bitumen increase [1-6]. However, due to the increase in viscosity, the mixing and compaction temperatures of bitumen also increase [7]. Therefore, during application, energy consumption increases, arising the additional costs to achieve the required workability, and the construction time is extended.

Warm mix asphalt (WMA) technology is widely used to eliminate the negative effect of SBS on the workability of bitumen. WMA additives can reduce the viscosity of styrene-butadiene-styrene modified bitumen (SBSMB) and increase its workability [8, 9]. On the other hand, waste oils have a similar effect on bitumen. Regarding sustainability and environmental awareness, using waste oils as a bitumen modifier is more interesting than other additives. Accordingly, when the studies in the literature in which waste oils are used as a bitumen modifier were examined, it was seen that it is generally used as a rejuvenating or softening material [10-22].

Studies using waste oil with SBS are also available in the literature. However, the main goal in these studies was not to increase the workability of bitumen. Generally, waste oils were used as rejuvenators [23-25] or compatibilizers [26] of SBSMB. In addition, there are studies aiming to examine the effects of waste oils on fatigue life [27], aging resistance [28], and chemical and rheological properties [29-32] of SBSMB. In these studies, it was observed that some performance losses could be recovered by adding waste oils to aged bitumen. It was stated that it would be suitable for use in recycled asphalt pavements (RAP) applications [25]. In addition, it has been noted that adding waste oil can increase aging and fatigue resistance [27, 28, 33].

Waste oils are a broad concept and include various oil types such as bio-oil, waste engine oil, waste vegetable oil, and waste soybean oil. In this study, the oil used was the waste cooking oil (WCO) and it was subjected to filtration and dehydration processes. Besides, studies in which SBS and WCO were used together were also examined in the literature and it was observed that the number of studies was relatively low. In addition, in these studies, it was determined that the rejuvenation feature of WCO was especially benefited from [25, 28]. In other studies, involving SBS and WCO, other polymers were used in addition to SBS, and a composite modification was investigated [34, 35]. Thus, to the best of authors' knowledge, there was no study to add WCO to increase the workability of an unaged SBSMB. Therefore, this study is aimed to close the relevant gap in the literature.

In this study, it was aimed to examine the effect of WCO additive added to increase the workability of SBSMB on physical and rheological properties. Accordingly, WCO was added to 5% SBSMB at the ratios of 1%, 3%, 5%, 7% and 9%, in addition to the studies in the literature, to comprehensively evaluate the effect of WCO on SBSMB on a wide scale. Then, penetration, softening point, ductility, Nicholson stripping, rolling thin film oven (RTFO), rotational viscosity (RV), and rheological tests were carried out. Thus, the workability, high-temperature performance, adhesion capacity, and aging resistance of the composite-modified bitumen were investigated.

2 MATERIALS AND METHODS

2.1. Materials and Sample Preparation

SBSMB, which has high resistance to rutting, has become increasingly common in Türkiye. SBSMB, which was prepared by adding 5% SBS by weight to 50/70 penetration grade base bitumen, was obtained from Isfalt Company. In addition, the company stated that the performance grade of SBSMB is PG76-16. The physical properties of SBSMB and limit values of these physical properties specified in the Highways Technical Specification [36] for modified bitumens are given in Table 1. From this table, it can be seen that the physical properties of SBSMB meet the specification limits.

Table 1 - Physical properties of the SBSMB.

Properties	Value	Specification limits	Specification
Penetration @ 25°C, dmm	35	25-55	TS EN 1426 [37]
Softening point, °C	65.5	≥60	TS EN 1427 [38]
Ductility @ 25°C, cm	100+	-	TS EN 13589 [39]
Specific gravity @ 25°C, g/cm^3	1.034	1.0-1.1	TS EN 15326 [40]
Flash point, °C	340	≥220	TS EN ISO 2592 [41]
Mass loss, %	0.23	0.8	TS EN 12607-1 [42]
Increase in softening point, °C	0.5	≤10	TS EN 1427 [38]
Retained penetration, %	91.4	≥45	TS EN 1426 [37]
Viscosity @ 135°C, cP	1850	-	ASTM D4402 [43]
Viscosity @ 165°C, cP	450	-	ASTM D4402 [43]

WCO was used as variable additive of the composite modified bitumen. The WCO used was obtained from Degam Company. This company collects WCOs from all over Türkiye and purifies them from pollutants, oxidant products, and particles. WCO, which had undergone these processes, was added to the SBSMB at different ratios (1%, 3%, 5%, 7%, and 9%) by weight of the SBSMB.

Table 2 - Physical properties of the aggregates.

Properties	Value	Specification
Volume specific gravity, g/cm^3	2.580	TS EN 1097-6 [44]
Apparent specific gravity, g/cm^3	2.645	TS EN 1097-6 [44]
Absorption, %	1.41	TS EN 1097-6 [44]
Polishing value	61.7	TS EN 1097-8 [45]

To prepare the composite modified bitumen samples, WCO was added to SBSMB samples at 150°C, as it is a material that can easily mix with bitumen, by using a mechanical stirrer at a rotation speed of 1000 rpm for 30 minutes. In addition, since it was predicted that composite modified bitumens may age due to the effect of temperature during the preparation process, the same mixing procedure was applied to the control sample (SBSMB). Then, the preparation of composite modified bitumens and control sample for testing was completed.

Basalt aggregates with dimensions between 4.75-9.50 mm were used to evaluate the adhesion between composite modified bitumen and aggregate. The physical properties of the aggregates are given in Table 2.

2.2. Methods Used to Evaluate Binder Performance

The penetration test is carried out to determine the hardness of bitumen samples at 25°C following the ASTM D5 [46] standard. An increase in the penetration value of a bitumen sample is an indication of its softening. Similarly, the softening point test can be used to determine the consistency of bitumen. In this test, ring and ball test apparatus conforming to ASTM D36-14 [47] standard is used. Bitumen sample is placed in the test apparatus and heated in a water bath at a heating rate of 5°C/min. The temperature value when the bitumen-coated ball touches the bottom plate is recorded as the softening point.

Since bitumen is a thermoplastic material, it softens with an increase in temperature and hardens with a decrease in temperature. This behavior is called temperature sensitivity. The penetration index (PI) of a bitumen sample gives an idea of the temperature sensitivity of that sample. High PI values indicate that bitumen has low-temperature sensitivity. The PI value is calculated with the help of Equation (1):

$$PI = \frac{1952 - 500 \times \log(Pen25) - 20 * SP}{50 \times \log(Pen25) - SP - 120} \quad (1)$$

where SP is the softening point temperature, and Pen25 is the penetration of the bitumen sample at 25°C.

Ductility test carried out following the ASTM D113 [48] standard. In this test, a tensile force at a speed of 5 cm/min at 25°C is applied to the bitumen samples placed in certain molds, and the distance the samples can extend without breaking is measured. This distance is recorded in cm as ductility value.

RTFO test performed following the ASTM D2872 [49] standard. With this test, short-term aging of the bitumen is simulated. The mass loss is determined with the help of Equation (2). It occurs due to the loss of volatile substances in the bitumen samples due to high temperatures. It is thought that the higher this value, the more the bitumen will be affected by the short-term aging.

$$Mass\ Loss, \% = \frac{Unaged\ Mass - Aged\ Mass}{Unaged\ Mass} \times 100 \quad (2)$$

PAV test was performed according to ASTM D6521 [50] to simulate the long-term aging that bitumen is exposed to due to climate and oxidation effects during its service life. For this

test, 50±0.5 g of bitumen was taken from RTFO-aged samples and placed in test vessels. Then, the samples were aged for 20 h at 100◦C under a pressure of 2.10 MPa.

The Nicholson stripping test is used to determine the resistance of bitumen against stripping. 100±0.5 g of crushed aggregate between 9.5-6.3 mm diameter is kept at 140-150°C for 1 hour. Then, approximately 5.0±0.1 g of bitumen is added to the aggregates and mixed until all aggregates are covered with bitumen. The prepared aggregate and bitumen mixture is transferred to petri dishes, and at least 3 cm height water is added and kept in an oven at 60°C for 24 hours. As a result, the separation of bitumen from the aggregate surface is determined visually in percent with the help of a light source.

RV test is carried out following the ASTM D4402 [43] standard. With this test, information about the workability of bitumen can be obtained. According to the Superpave specification, the viscosity value of the bitumen sample obtained from the RV test should not exceed 3000 cP. It is also possible to determine the mixing and compaction temperatures at which bitumen will be used with the RV test. Accordingly, the viscosities of the samples were measured in the Brookfield DV2T rotational viscometer using spindle #29 at 135°C, 165°C, and 180°C temperatures. Then, the results were marked on a graph and combined with a trend line. On this line, the temperatures corresponding to the viscosity values of 170±20 cP and 280±30 represent the mixing and compaction temperatures of the bitumen sample, respectively [51].

It is possible to examine the rheological properties of bitumen with various tests carried out using dynamic shear rheometer (DSR). Tests based on determining the complex shear modulus (|G*|) and phase angle (δ) of bitumen, carried out according to ASTM D7175, are one of these tests. Thanks to this test, information can be obtained about the resistance against rutting at high temperatures and fatigue cracking after repeated loading at intermediate temperatures of the asphalt pavement, which tested bitumen will be used. Unaged, RTFO or PAV aged bitumen samples are placed between two parallel plates of the DSR device that a controlled-strain testing mode was used and exposed to oscillating motion with a frequency of 1.59 Hz by the top plate. The diameter of the plates are 25 mm for unaged and RTFO-aged samples and 8 mm for PAV-aged samples. In addition, the gap between the plates is 1 mm for unaged and RTFO-aged samples, while this value is 2 mm for PAV-aged samples. After tests carried out with DSR, which are carried out under the specified conditions, the complex shear modulus (|G*|) and phase angle (δ) of the bitumen are determined. Its viscous and elastic behavior is characterized. |G*| is the indicator of the total resistance of the bitumen to deformation, while δ is defined as the phase difference between stress and strain. The |G*|/sinδ value obtained using the |G*| and δ values are the rutting resistance parameter of the bitumen. This value should be at least 1.00 kPa for unaged bitumen and at least 2.20 kPa for RTFOT aged bitumen. In addition, the |G*|·sinδ value is the fatigue resistance parameter of bitumen, and this value should not be more than 5000 kPa for PAV aged samples.

3. RESULTS AND DISCUSSION

3.1. Physical Properties of Modified Bitumen

The results obtained from the penetration and softening point tests are given in Figure 1. As seen in Figure 1(a), when WCO was added to SBSMB at the rates of 1%, 3%, 5%, 7%, and 9%, an increase of 48.5%, 125.7%, 240%, 322.9%, and 414.3% was observed in the

penetration value, respectively. Additionally, it is seen that when 1%, 3%, 5%, 7%, and 9% WCO is added to SBSMB, the softening point value decreases by 5.11%, 6.71%, 10.76%, 14.19%, and 17.25%, respectively. In parallel, the results of the two tests indicate that when WCO is added to SBSMB, a softening occurs with an increasing WCO ratio; in other words, the consistency of SBSMB decreases. In addition, it was stated in similar studies in the literature [24, 26, 28] that oils or waste oils increase the penetration value of SBSMB while decreasing the softening point.

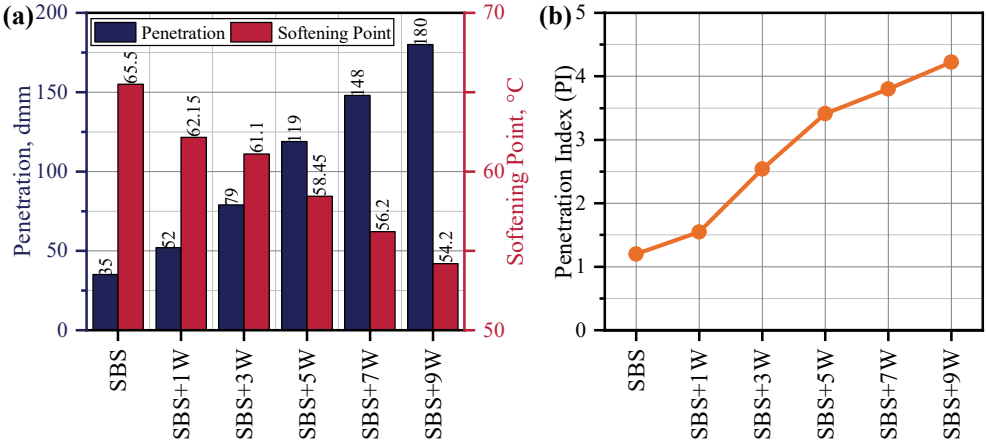

Figure 1 - Physical test results of the bitumen samples: (a) penetration and (b) penetration index (PI).

PI values were calculated with the help of Equation (1), and the results are given in Figure 1(b). When 1%, 3%, 5%, 7%, and 9% WCO was added to SBSMB, an increase of 29.2%, 111.7%, 184.2%, 216.7%, and 252.5% was observed in the PI value, respectively. These results show that the addition of WCO to SBSMB reduces the thermal sensitivity of SBSMB.

As a result of the ductility tests, no breaking was observed in any of the samples within a distance of 100 cm, which is the maximum tensile length of the test device. In other words, this shows that the ductility does not change or is not adversely affected by the addition of WCO to the SBSMB within the measurement limits of the test device. Cong et al. [28] reported that the ductility value increased with the addition of corn oil based WCO to base or SBSMB, and the ductility of bitumen containing WCO was greater than 100 cm. In another study, it was stated that the ductility of bitumen containing waste bio-oil and SBS was higher than that of SBS modified bitumen [26].

3.2. Short Term Aging

Mass losses of the samples were determined after RTFO tests carried out to examine the level of exposure of bitumen samples to short-term aging after mixing and compaction processes in asphalt pavement construction. The percent mass losses obtained are shown in Figure 2. When Figure 2 is examined, it is seen that all modified bitumen samples exhibit a mass loss

of less than 1%, which is the upper limit of the ASTM D6373 [53] standard. This indicates that all samples can perform in the pavement after short-term aging without critical disadvantage. In addition, with the addition of 1%, 3%, 5%, 7%, and 9% WCO to SBSMB, the mass loss values decreased by 26.08%, 39.13%, 39.13%, 43.47%, and 52.17%, respectively. These results show that the addition of WCO to SBSMB can increase the resistance of SBSMB to short-term aging. Similar to these results, in a previous study by Kumandaş et al. [54], it was determined that the aging resistance of modified bitumen increased with WCO addition.

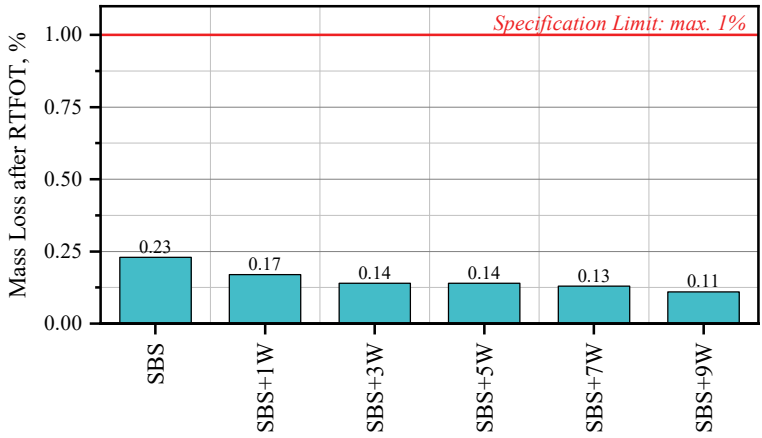

Figure 2 - Mass losses after RTFO test.

The results obtained by applying penetration and softening point tests to short-term aged bitumen samples are shown in Figure 3(a). When this figure was examined, it was observed that the obtained values increased for softening point values and decreased for penetration values after short-term aging compared to unaged bitumen samples. In order to obtain more detailed information about this hardening phenomenon caused by aging, the softening point differences (ΔS) and retained penetration percentages are determined and given in Figure 3(b). Although an increase in aging resistance was observed with the increasing amount of WCO according to the mass loss percentages, a similar relationship could not be observed for softening point difference values and penetration decrease percentages. Especially, in terms of penetration decrease percentages, SBSMB was least affected by hardening in the RTFOT effect, with 8% penetration decrease. On the other hand, it was determined that there was a decrease in the penetration values of bitumens containing WCO, varying between 24.4% and 38.7%. It is thought that this result cannot be attributed to bitumens containing WCO being more affected by aging compared to SBSMB. Regardless of the additive, a softer bitumen can be expected to harden more after aging than a bitumen with less penetration. In other words, SBSMB has already largely completed its hardening by modifying the base bitumen with SBS. Since SBSMBs containing WCO are much softer compared to SBSMB, they were more affected by the decrease in penetration after RTFOT. However, it can be said that this is due to the softness of the bitumen rather than the effect of WCO on aging. For this reason, it is thought that the percentage of penetration decrease in SBSMBs with and without WCO may not be a suitable indicator for resistance to aging.

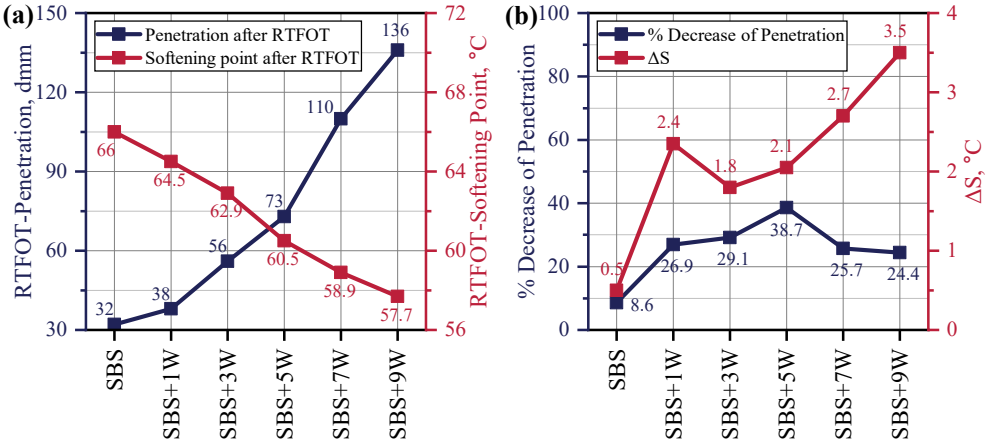

Figure 3 - Test results after RTFO: (a) penetration and softening point, and (b) decrease of penetration and difference in softening point.

3.3. Interaction Between Bitumen and Aggregate

The results from the Nicholson stripping tests are given in Figure 4 and Figure 5. When 1%, 3%, 5%, 7%, and 9% WCO was added to SBSMB, the Nicholson stripping ratios were 87.5%, 90%, 90%, 92%, and 94%, respectively. As can be understood from these results, the

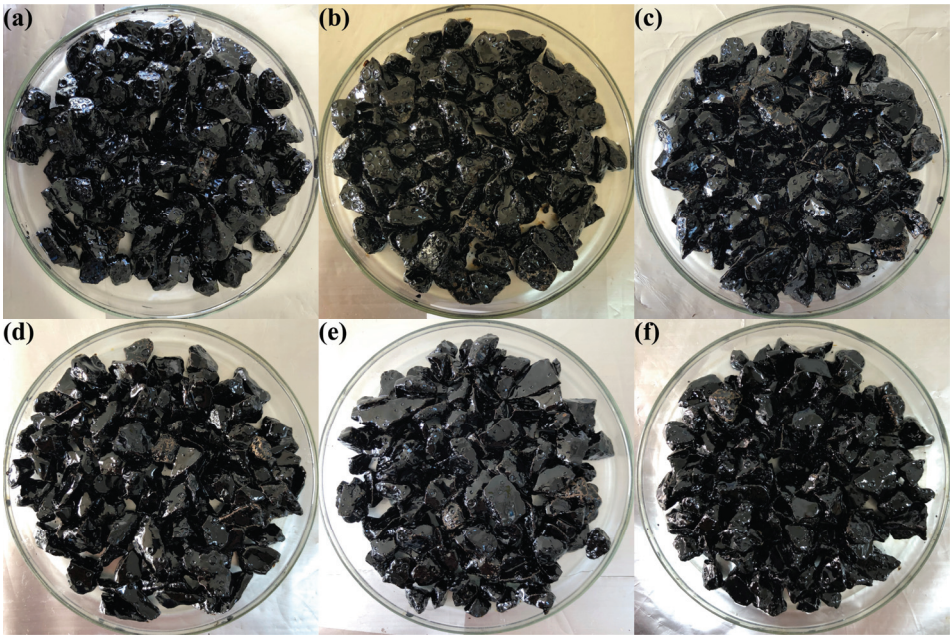

Figure 4 - Images of the samples after the Nicholson stripping test: (a) SBS, (b) SBS+1W, (c) SBS+3W, (d) SBS+5W, (e) SBS+7W, and (f) SBS+9W

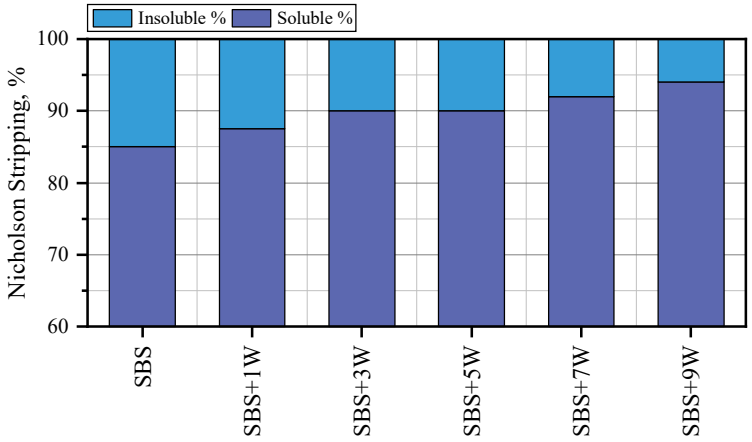

Figure 5 - Nicholson stripping test results.

adhesion of SBSMB with aggregate increased with the increasing amount of WCO. SBSMB already has high cohesion and interacts strongly with the aggregate. On the other hand, the addition of WCO softens the SBSMB, helping it to spread more easily on the aggregate surface. Thus, WCO enables the adhesion-enhancing effect of SBS to show in a larger surface area of the aggregate.

3.4. Impact of the WCO on the Workability of SBSMB

The results of RV tests conducted at 135°C are shown in Figure 6(a). When Figure 6(a) is examined, it is seen that all samples have a viscosity lower than the upper limit of the specification [53]. According to these results, it is predicted that all samples will not pose a problem in terms of mixability and compactibility.

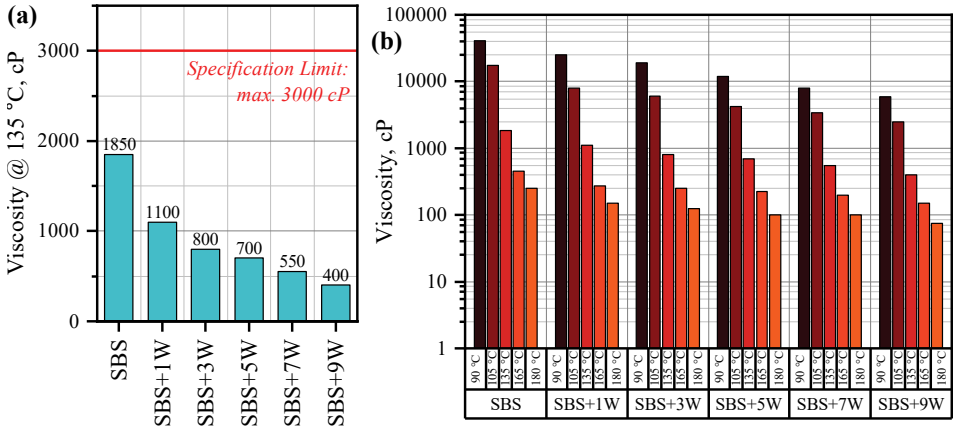

Figure 6 - Results of RV tests: (a) comparison with the specification limit at 135°C, and (b) viscosity values at different temperatures between 90 °C and 180 °C.

To better understand the viscosity-temperature behavior of the samples, the results of the RV tests carried out in a wide temperature range (90°C, 105°C, 135°C, 165°C, and 180°C) are shown in Figure 6(b). As shown in this graph drawn on the logarithmic axis, SBSMB has the highest viscosity values, and SBS+9W has the lowest viscosity values at all temperatures. Similar to these results, Sun et al. [30] added WCO based bio-oil to SBS modified bitumen in their study and stated that the viscosity of SBS modified bitumen decreased in parallel with increasing bio-oil addition. In another study by Cong et al. [28], it was emphasized that the viscosity of the control asphalt gradually decreased with increasing WCO based bio-oil addition. In addition to the findings in the literature, it was determined in this study that the addition of WCO increased the workability of unaged-SBSMB.

The percentage changes in the viscosities of the samples were determined according to the results of the RV tests and shown in Figure 7. Especially when looking at the data in the temperature range of 135-165°C on this figure, it is seen that the percentage change in the viscosity of SBSMB is higher than the other samples. This result indicates that in parallel with the PI results, SBSMB is more affected by the heat change than the other samples, and this effect rate decreases with increasing WCO addition. In other words, SBSMB has the highest thermal sensitivity, and SBS+9W has the lowest thermal sensitivity among the tested samples.

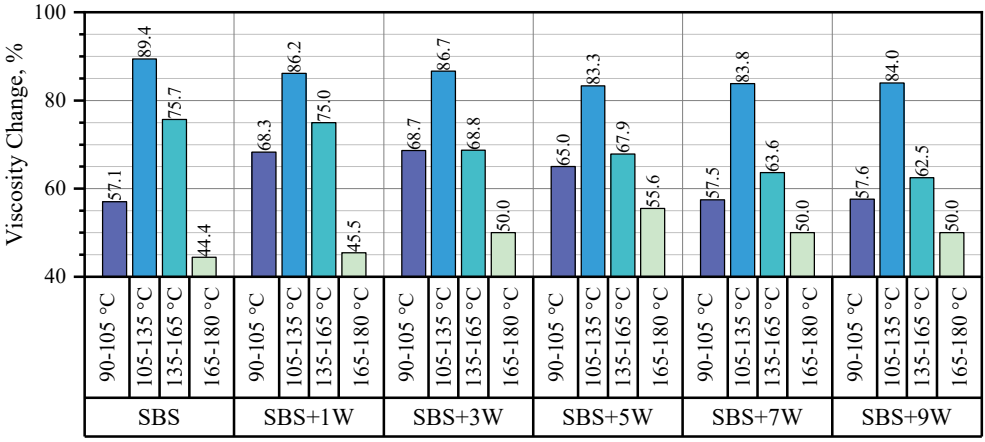

Figure 7 - Percentage change of viscosities.

In addition to the tests carried out on the viscosities of the samples, the results from the RV tests at 135°C, 165°C, and 180°C were placed on a logarithmic axis and combined with a trend line (Figure 8(a)). This trend line was used to determine mixing and compaction temperatures of the samples and the results are shown in Figure 8(b). In this figure, the average of the temperatures corresponding to 170±20 cP is given as the main mixing temperature. Similarly, the average of temperatures corresponding to 280±30 cP is stated as the mean compaction temperature. Additionally, the lower and upper limits of mixing and compaction temperatures are shown on the graph with error bars. When Figure 8(b) is examined, it is understood that the mean mixing and compaction temperatures of SBSMB are approximately 186 and 177.8°C, respectively. Although this result is generally

encountered in polymer-modified bitumen, it can create an economic disadvantage by increasing the energy consumed during construction and increase the damage to the environment by increasing carbon emissions. When WCO is added to SBSMB, it is seen that there is a significant decrease in mixing and compaction temperatures. Especially in the WCO+9W sample, the mixing and compaction temperatures decreased to 162.6°C and 149.4°C, respectively. This result indicates that the addition of WCO can both provide significant savings in terms of energy consumption and play a critical role in reducing the amount of carbon released to the environment.

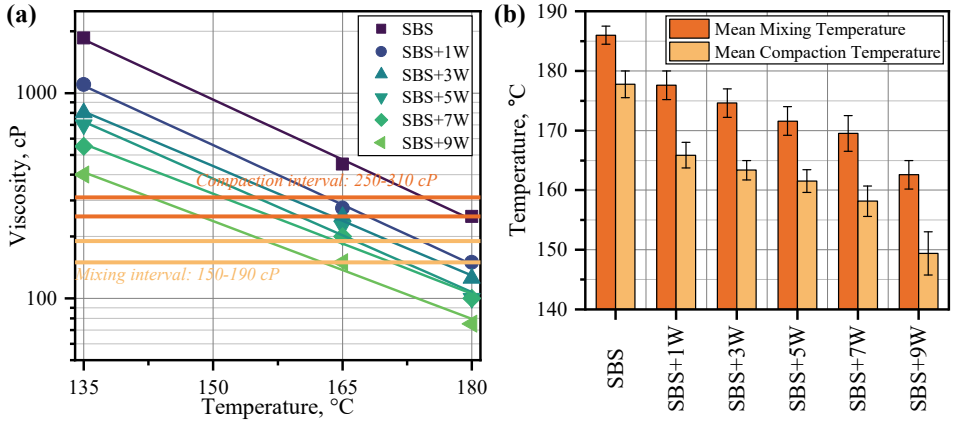

Figure 8 - Determination of mixing and compaction temperatures: (a) limit temperature intervals, and (b) mean mixing and compaction temperatures.

3.5. Rheological Behavior of SBS+WCO Modified Bitumen

|G*| and δ parameters obtained from tests conducted with DSR are shown in Figure 9(a) and Figure 9(b), respectively. As seen in Figure 9(a), there was a decrease in |G*| values with both increasing temperature and increasing WCO ratio. While the decrease occurring with the increase in temperature is due to the nature of the bitumen itself, the decrease occurring with the increasing additive ratio is an indicator of the softening effect of WCO. Additionally, when Figure 9(b) is examined, it is seen that the phase angles also decrease with WCO addition. However, there is no clear trend between the increase in the WCO ratio and the decrease in phase angle; the highest decrease occurred at 7% WCO and the lowest decrease occurred at 3% WCO. Therefore, it was not possible to make a definitive judgment regarding the effect of WCO addition on the elasticity of SBSMB based on phase angle values. |G*|/sinδ rutting parameters of all samples are given in Figure 10(a). Similar to |G*| values, the increase in temperature and WCO ratio decreases |G*|/sinδ values of the samples. It has been shown in many studies that waste oils adversely affect the rutting resistance of bitumen [17, 26, 30, 31, 35]. Similar results with the literature are obtained in this study. On the other hand, all samples at 64°C, all samples except SBS+9W at 70°C, and all other samples except SBS+7W and SBS+9W samples at 76°C met the 1.0 kPa rutting resistance specification limit value. Additionally, continuous grades (CGs) of all samples are given in Figure 10(b). CGs of all samples, determined by finding the temperature at which they meet the specification value. As seen in Figure 10(b), increasing the WCO ratio caused a decrease in the CG values of

SBSMB. These results show that the addition of WCO causes a decrease in the rutting performance of SBSMB. For this reason, rutting performance should be considered as critical parameter when selecting the WCO ratio to be added to SBSMB. If WCO is to be added to SBSMB on roads with high density or heavy traffic, it would be appropriate to choose low ratios such as 3% and 5% to avoid loss of performance.

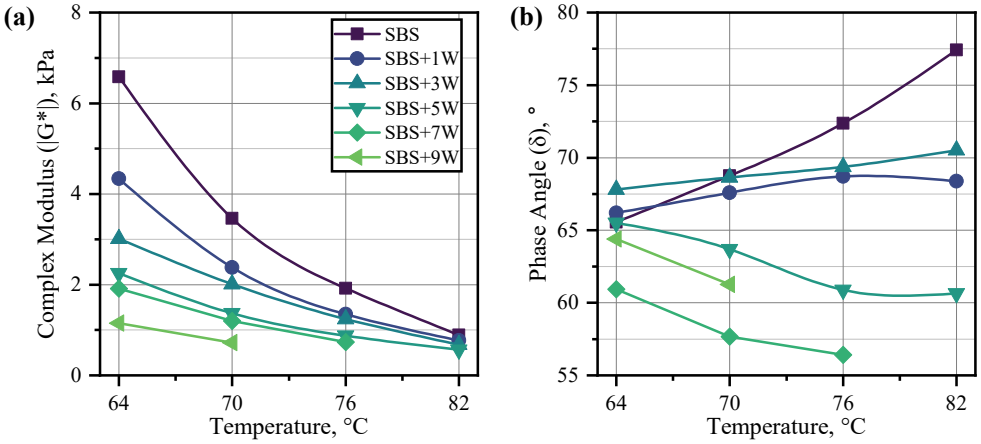

Figure 9 - Unaged samples: (a) |G| values, and (b) phase angles.*

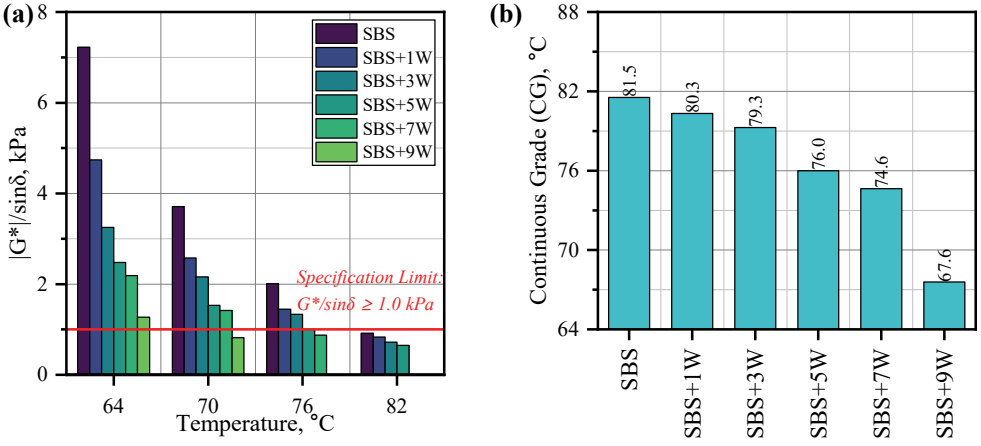

Figure 10 - Unaged samples: (a) Rutting performance, and (b) continuous grades.

The |G*| and δ values of the RTFO-aged samples are shown in Figure 11(a) and Figure 11(b). It is seen that |G*| values decrease with increasing temperature and additive ratio, similar to the results obtained from unaged samples. On the other hand, when Figure 11(b) is examined, it can be said that increasing temperature increases the phase angle values. This is an expected result due to the nature of bitumen. However, it was not possible to talk about a clear trend regarding the effect of WCO addition on the phase angle.

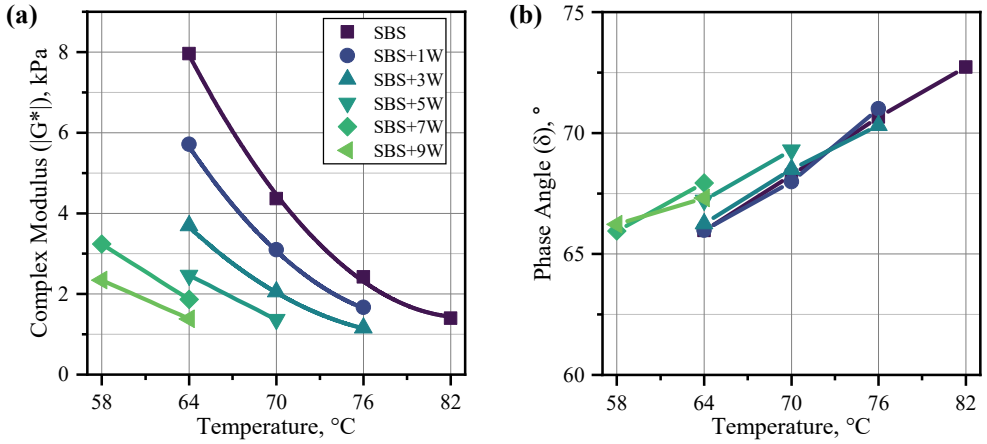

Figure 11 - RTFOT aged samples: (a) |G| values, and (b) phase angles.*

ASTM D6373 [53] standard recommends using RTFO-aged samples to evaluate rutting performance. |G*|/sinδ and CG values of the RTFO-aged samples are given in Figure 12(a) and Figure 12(b), respectively. When Figure 12(a) is examined, it is seen that the specification limit of 2.2 kPa is met by SBS, SBS+1W, SBS+3W, and SBS+5W samples at 64°C, SBS, SBS+1W SBS+3W samples at 70°C and only SBS samples at 76°C. On the other hand, when Figure 12(b) is examined, it is observed that there is a decrease in CG values with the addition of WCO, similar to the unaged samples. However, the results obtained from RTFO-aged samples are lower temperatures compared to the results obtained from unaged samples. This shows that RTFO-aged samples reached the specification limit earlier. Therefore, if WCO is to be added to SBSMB in the application, RTFO values of RTFO-aged samples must be considered.

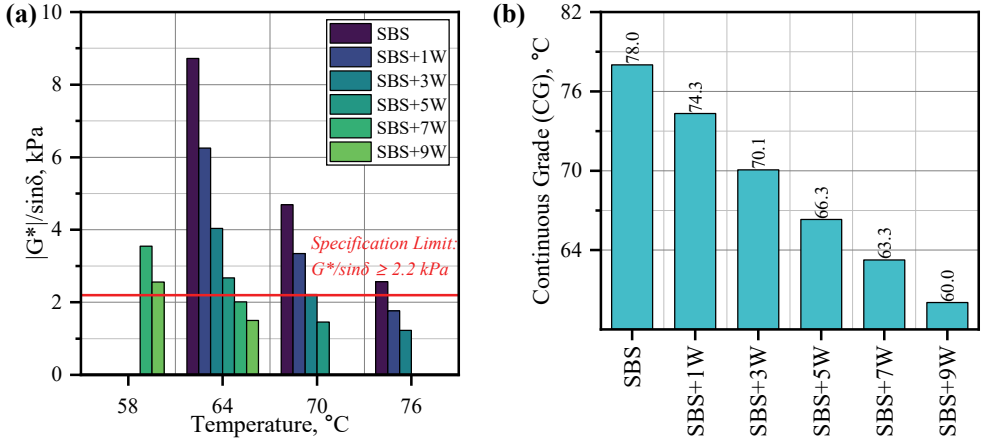

Figure 12 - RTFOT aged samples: (a) Rutting performance, and (b) continuous grades.

|G*|·sinδ parameters of the PAV-aged samples at intermediate temperatures are given in Figure 13. As can be seen from the Figure 13, samples did not exceed the specification limit of 5000 kPa at all temperatures. It is seen that the |G*|·sinδ value decreases with the increase in the amount of WCO added. These results indicates that WCO increases the fatigue resistance of SBSMB. This positive effect of WCO on fatigue resistance is consistent with the results of previous studies. In a study by Mollamohammadi and Hesami [25], it was determined that composite WCO consisting of soybean, rapeseed, palm, and sunflower oils significantly improved fatigue performance. In addition to the findings in the literature, in this study, it was found that the addition of WCO increased the fatigue resistance of unaged-SBSMB.

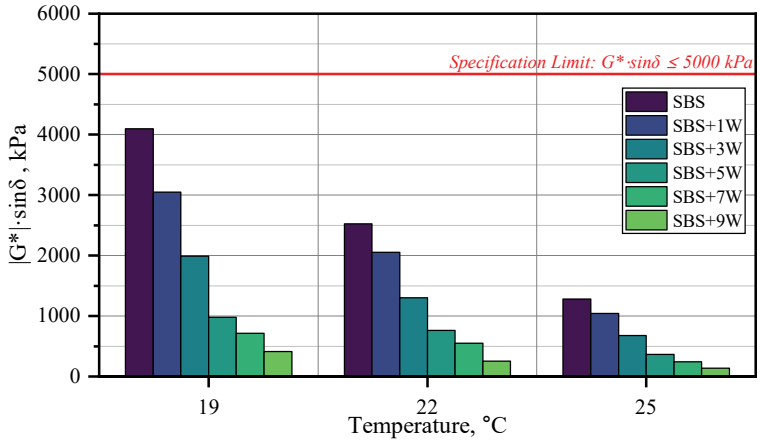

Figure 13 - Fatigue parameter values of PAV-aged samples.

As mentioned above, the findings obtained from the tests carried out with DSR show that WCO increases the fatigue resistance of SBSMB while reducing the rutting resistance. Examining the effect of WCO on rutting and fatigue resistance of SBSMB with MSCR and LAS tests, respectively, may provide more reliable results. However, since this study mainly focuses on examining the workability of SBSMB, further studies may contribute to the literature by comprehensively examining the effect of WCO on the rutting and fatigue resistance of SBSMB with MSCR and LAS tests, respectively.

4. CONCLUSIONS

In this study, unlike the existing studies in the literature involving SBS and WCO, WCO was used as flow improver in unaged SBSMB. In other words, this study was carried out to increase the workability of unaged-SBSMB with the addition of WCO rather than the use of WCO as a rejuvenator or a fatigue resistance enhancer in SBSMB. In this context, 1%, 3%, 5%, 7%, and 9% WCO was added to 5% SBS modified bitumen (SBSMB) and the physical and rheological properties of the obtained composite modified bitumen were investigated by experimental methods. The results obtained from the tests carried out in this direction are summarized below:

- When the physical properties of composite modified bitumen are examined, it can be said that the consistency and thermal sensitivity of SBSMB decrease with the addition of WCO.
- When the stripping resistance of the composite modified bitumen and aggregate mixture was examined, the stripping resistance of SBSMB improved with the addition of WCO.
- The results from the RV tests showed that the workability of SBSMB was significantly improved with the addition of WCO. With the addition of 9% WCO, the mixing and compaction temperatures of SBSMB decreased by 13% and 16%, respectively.
- When the rheological behavior of composite modified bitumen was examined, it was observed that while the rutting resistance of SBSMB decreased with the addition of WCO, the fatigue resistance increased. In addition to these results, the resistance of SBSMB to short-term aging improved with the addition of WCO.

Adding WCO to unaged-SBSMB can contribute to environmental health by increasing workability, reducing carbon emissions during asphalt pavement construction, and promoting waste materials in different areas. In addition, it can also be economically beneficial by lowering energy consumption during construction. Finally, WCO can soften the SBSMB and enable the bitumen to better envelop the aggregate. Thus, the increase in adhesion between the bitumen-aggregate can positively affect the stripping resistance of the pavement. In future studies, it is thought that it will be helpful to determine the performance of SBS+WCO composite modified bitumen at low temperatures and the properties of asphalt mixture samples to be prepared with this bitumen.

References

[1] Rongali, U.D., Swamy, A.K., Jain, P.K., Effect of SBS and HDPH polymer on rheological properties of asphalt. Pet. Sci. Technol. 34, 21, 1790-1796, 2016.

[2] Babagoli, R., Mohammadi, R., Ameri, M., The rheological behavior of bitumen and moisture susceptibility modified with SBS and nanoclay. Pet. Sci. Technol. 35, 11, 1085-1090, 2017.

[3] Nejad, F.M., Shahabi, M., Rahi, M., Hajikarimi, P., Kazemifard, S., An investigation on the effect of SBS+Vacuum bottoms residue modification on rheological characteristics of asphalt binder. Pet. Sci. Technol. 35, 22, 2115-2120, 2017.

[4] Xu, S., Huang, W., Cai, F., Huang, H., Hu, C., Evaluation of properties of Trinidad Lake Asphalt and SBS-modified petroleum asphalt. Pet. Sci. Technol. 37, 2, 234-241, 2019.

[5] Rezaei, S., Ziari, H., Nowbakht, S., Low temperature functional analysis of bitumen modified with composite of nano-SiO2 and styrene butadiene styrene polymer. Pet. Sci. Technol. 34, 5, 415-421, 2016.

[6] Gao, Z., Fu, H., Chen, Q., Cao, Y., Rheological properties and viscosity reduction mechanism of SBS warm-mix modified asphalt. Pet. Sci. Technol. 38, 6, 556-564, 2020.

[7] Yılmaz, M., Kök, B.V., Stiren-Butadien-Stiren Modifiyeli Bitümlü Bağlayıcıların Superpave Sistemine Göre Yüksek Sıcaklık Performans Seviyesinin ve İşlenebilirliğinin Belirlenmesi. J. Fac. Eng. Archit. Gazi Univ. 23, 4, 811-819, 2008.

[8] Shang, L.N., Wang, S.F., Zhang, Y., Zhang, Y.X., Pyrolyzed wax from recycled cross-linked polyethylene as warm mix asphalt (WMA) additive for SBS modified asphalt. Constr. Build. Mater. 25, 2, 886-891, 2011.

[9] Kataware, A.V., Singh, D., Evaluating effectiveness of WMA additives for SBS modified binder based on viscosity, Superpave PG, rutting and fatigue performance. Constr. Build. Mater. 146, 436-444, 2017.

[10] Azahar, W.N.A.W., Jaya, R.P., Hainin, M.R., Bujang, M., Ngadi, N., Chemical modification of waste cooking oil to improve the physical and rheological properties of asphalt binder. Constr. Build. Mater. 126, 218-226, 2016.

[11] Yan, K., Liu, W., You, L., Ou, J., Zhang, M., Evaluation of waste cooling oil and European Rock Asphalt modified asphalt with laboratory tests and economic cost comparison. J. Clean. Prod. 310, 127364, 2021.

[12] Al-Omari, A.A., Khedaywi, T.S., Khasawneh, M.A., Laboratory characterization of asphalt binders modified with waste vegetable oil using SuperPave specifications. Int. J. Pavement Res. Technol. 11, 1, 68-76, 2018.

[13] Elahi, Z., Mohd Jakarni, F., Muniandy, R., Hassim, S., Ab Razak, M.S., Ansari, A.H., Ben Zair, M.M., Waste Cooking Oil as a Sustainable Bio Modifier for Asphalt Modification: A Review. Sustainability. 13, 20, 11506, 2021.

[14] Ahmed, R.B., Hossain, K., Waste cooking oil as an asphalt rejuvenator: A state-of-the-art review. Constr. Build. Mater. 230, 116985, 2020.

[15] Rahman, M.T., Hainin, M.R., Abu Bakar, W.A.W., Use of waste cooking oil, tire rubber powder and palm oil fuel ash in partial replacement of bitumen. Constr. Build. Mater. 150, 95-104, 2017.

[16] Babagoli, R., Ameli, A., Influence of Soybean Oil on Binder and Warm Mixture Asphalt Properties. Adv. Mater. Sci. Eng. 2021, 6860878, 2021.

[17] Sun, Z., Yi, J., Huang, Y., Feng, D., Guo, C., Properties of asphalt binder modified by bio-oil derived from waste cooking oil. Constr. Build. Mater. 102, 496-504, 2016.

[18] Eriskin, E., Karahancer, S., Terzi, S., Saltan, M., Waste frying oil modified bitumen usage for sustainable hot mix asphalt pavement. Arch. Civ. Mech. Eng. 17, 4, 863-870, 2017.

[19] Dong, R., Zhao, M., Tang, N., Characterization of crumb tire rubber lightly pyrolyzed in waste cooking oil and the properties of its modified bitumen. Constr. Build. Mater. 195, 10-18, 2019.

[20] Zhao, X., Lu, Z., Su, H., Le, Q., Zhang, B., Wang, W., Effect of Sasobit/Waste Cooking Oil Composite on the Physical, Rheological, and Aging Properties of Styrene–Butadiene Rubber (SBR)-Modified Bitumen Binders. Mater. 16, 23, 7368, 2023.

[21] Li, H., Dong, B., Wang, W., Zhao, G., Guo, P., Ma, Q., Effect of Waste Engine Oil and Waste Cooking Oil on Performance Improvement of Aged Asphalt. Appl. Sci. 9, 9, 1767, 2019.

[22] Li, H., Zhang, F., Feng, Z., Li, W., Zou, X., Study on waste engine oil and waste cooking oil on performance improvement of aged asphalt and application in reclaimed asphalt mixture. Constr. Build. Mater. 276, 122138, 2021.

[23] Chen, M.Z., Leng, B.B., Wu, S.P., Sang, Y., Physical, chemical and rheological properties of waste edible vegetable oil rejuvenated asphalt binders. Constr. Build. Mater. 66, 286-298, 2014.

[24] Zhang, D., Zhang, H., Zhu, C., Effect of different rejuvenators on the properties of aged SBS modified asphalt. Pet. Sci. Technol. 35, 1, 72-78, 2017.

[25] Mollamohammadi, A., Hesami, S., Evaluation of the Effect of WCO/SBS-Modified RAB and RAP and Stiffness Recovery Procedure on Fatigue Performance of HMA. J. Mater. Civ. Eng. 35, 2, 04022399, 2023.

[26] Nie, X., Li, Z., Yao, H., Hou, T., Zhou, X., Li, C., Waste bio-oil as a compatibilizer for high content SBS modified asphalt. Pet. Sci. Technol. 38, 4, 316-322, 2020.

[27] Plewa, A., Asphalt Mixtures with Binders Fluidized by Addition of Vegetable Origin Oil for Applications as Flexible Anti-Crack Layers. Roads Bridges. 18, 3, 181-192, 2019.

[28] Cong, P., Chen, B., Zhao, H., Coupling effects of wasted cooking oil and antioxidant on aging of asphalt binders. Int. J. Pavement Res. Technol. 13, 1, 64-74, 2020.

[29] Wang, C., Xue, L., Xie, W., You, Z., Yang, X., Laboratory investigation on chemical and rheological properties of bio-asphalt binders incorporating waste cooking oil. Constr. Build. Mater. 167, 348-358, 2018.

[30] Sun, Z., Yi, J., Chen, Z., Xie, S., Xu, M., Feng, D., Chemical and rheological properties of polymer modified bitumen incorporating bio-oil derived from waste cooking oil. Mater. Struct. 52, 5, 106, 2019.

[31] Liu, S., Meng, H., Xu, Y., Zhou, S., Evaluation of rheological characteristics of asphalt modified with waste engine oil (WEO). Pet. Sci. Technol. 36, 6, 475-480, 2018.

[32] Liu, S., Peng, A., Wu, J., Zhou, S.B., Waste engine oil influences on chemical and rheological properties of different asphalt binders. Constr. Build. Mater. 191, 1210-1220, 2018.

[33] Liu, S., Peng, A., Zhou, S., Wu, J., Xuan, W., Liu, W., Evaluation of the ageing behaviour of waste engine oil-modified asphalt binders. Constr. Build. Mater. 223, 394-408, 2019.

[34] Luo, W.H., Zhang, Y.H., Cong, P.L., Investigation on physical and high temperature rheology properties of asphalt binder adding waste oil and polymers. Constr. Build. Mater. 144, 13-24, 2017.

[35] Liu, S., Zhou, S., Peng, A., Li, W., Investigation of physiochemical and rheological properties of waste cooking oil/SBS/EVA composite modified petroleum asphalt. J. Appl. Polym. Sci. 137, 26, 48828, 2020.

[36] KGM. Highway Technical Specifications. General Directorate of Highways, Ankara, Türkiye, 2023.

[37] TS EN 1426. Bitumen and bituminous binders - Determination of needle penetration. Turkish Standards Institution (TSI), Ankara, Türkiye, 2015.

[38] TS EN 1427. Bitumen and bituminous binders - Determination of the softening point - Ring and Ball method. Turkish Standards Institution (TSI), Ankara, Türkiye, 2015.

[39] TS EN 13589. Bitumen and bituminous binders - Determination of the tensile properties of modified bitumen by the force ductility method. Turkish Standards Institution (TSI), Ankara, Türkiye, 2018.

[40] TS EN 15326+A1. Bitumen and bituminous binders - Measurement of density and specific gravity - Capillary-stoppered pyknometer method. Turkish Standards Institution (TSI), Ankara, Türkiye, 2010.

[41] TS EN ISO 2592. Petroleum and related products - Determination of flash and fire points - Cleveland open cup method. Turkish Standards Institution (TSI), Ankara, Türkiye, 2017.

[42] TS EN 12607-1. Bitumen and bituminous binders - Determination of the resistance to hardening under influence of heat and air - Part 1: RTFOT method. Turkish Standards Institution (TSI), Ankara, Türkiye, 2015.

[43] ASTM D4402. Standard Test Method for Viscosity Determination of Asphalt at Elevated Temperatures Using a Rotational Viscometer. ASTM International, West Conshohocken, PA, 2015.

[44] TS EN 1097-6. Tests for mechanical and physical properties of aggregates - Part 6: Determination of particle density and water absorption. Turkish Standards Institution (TSI), Ankara, Türkiye, 2022.

[45] TS EN 1097-8. Tests for mechanical and physical properties of aggregates - Part 8: Determination of the polished stone value. Turkish Standards Institution (TSI), Ankara, Türkiye, 2020.

[46] ASTM D5. Standard Test Method for Penetration of Bituminous Materials. ASTM International, West Conshohocken, PA, 2020.

[47] ASTM D36-14. Standard Test Method for Softening Point of Bitumen (Ring-and-Ball Apparatus). ASTM International, West Conshohocken, PA, 2020.

[48] ASTM D113. Standard Test Method for Ductility of Asphalt Materials. ASTM International, West Conshohocken, PA, 2017.

[49] ASTM D2872. Standard Test Method for Effect of Heat and Air on a Moving Film of Asphalt (Rolling Thin-Film Oven Test). ASTM International, West Conshohocken, PA, 2019.

[50] ASTM D6521. Standard Practice for Accelerated Aging of Asphalt Binder Using a Pressurized Aging Vessel (PAV). ASTM International, West Conshohocken, PA, 2019.

[51] Karahancer, S., Effect of aluminum oxide nano particle on modified bitumen and hot mix asphalt. Petrol. Sci. Technol. 38, 13, 773-784, 2020.

[52] ASTM D7175. Standard Test Method for Determining the Rheological Properties of Asphalt Binder Using a Dynamic Shear Rheometer. ASTM International, West Conshohocken, PA, 2015.

[53] ASTM D6373. Standard Specification for Performance-Graded Asphalt Binder. ASTM International, West Conshohocken, PA, 2021.

[54] Kumandas, A., Cavdar, E., Oruc, S., Pancar, E.B., Kok, B.V., Effect of WCO addition on high and low-temperature performance of RET modified bitumen. Constr. Build. Mater. 323, 126561, 2022.

Turkish Journal of Civil Engineering, 2024 19-45, Paper 786, ***Research Article***

Debris Flow Impact on Rigid Walls: Protection by Tree Trunks

Pakhshan AHMADIAN[1*]
Umut TÜRKER[2]

ABSTRACT

To mitigate debris flow disasters, most of the previous research has focused, mostly through experimental methods, on placing different rigid barriers as structural prevention against debris flow to dissipate its energy. However, there has been less research on simulating the debris flow resistance on the tree trunk patches. In the present work, analytical and numerical simulation of the peak impact pressure of debris flow on a vertical rigid wall has been analysed under the protection of a patch of tree trunks. Along the debris flow path, tree trunks with identical diameters have been arranged in linear and rectilinear configurations. The mathematical analysis employs the Reynolds Transport Theorem, while the numerical simulations use the Reynolds-Averaged-Navier-Stokes equations. The numerical simulation results have depicted that the rectilinear configuration of tree trunks in each spot area is more effective than other configurations and increasing density of tree trunks within a given spot area is 50% more protective than the increasing the number of rows of the tree trunks. Additionally, this study estimates a new dynamic coefficient (α) as a function of the Froude number and devises a new expression for the drag force coefficient for different tree trunk configurations.

Keywords: Debris flow, rigid barriers, tree trunks, Reynolds transport theorem, Reynolds-averaged-Navier-Stokes.

1. INTRODUCTION

Based on the National Research Council (NRC) (Areas (1982)), the mud floods, mudflows, and debris flows have been classified as hyper-concentrated sediment flows. Based on the dominant shear stress from these three components, Julien and Leon (2000) offered a classification of hyper-concentrated sediment flows in debris flow in which dispersive stress

Note:
- This paper was received on July 11, 2023 and accepted for publication by the Editorial Board on June 11, 2024.
- Discussions on this paper will be accepted by January 31, 2025.
- https://doi.org/10.18400/tjce.1325755

1 Eastern Mediterranean University, Department of Civil Engineering, Famagusta, Turkish Republic of Northern Cyprus / pakhshan.ahmadian@cc.emu.edu.tr - https://orcid.org/0000-0002-3428-035X

2 Eastern Mediterranean University, Department of Civil Engineering, Famagusta, Turkish Republic of Northern Cyprus / umut.turker@emu.edu.tr - https://orcid.org/0000-0002-31647419

* Corresponding author

is dominant. Debris flow is the solid-liquid two-phase flow that consists of slurry or water containing silt, clay and sand (Thouret et al. (2020)). Since the kinetic energy of debris flow is very high, its interaction with engineering structures along their paths can be devastating (Armanini (1997)). Extreme impact force causes serious damage that can even end in societal disasters. Therefore, the determination of the debris flow impact force on any obstacle along their path should be taken as a priority (Yazid et al. (2017) and Mahnamfar et al. (2020)). There are several ways to carry out and calculate the debris flow impact forces. These can be categorized as analytic formulas, experimental studies at fields or flumes, or numerical analyses based on previous studies. Previously, several studies of debris flow impact forces have been conducted based on field measurements (e.g., Leonardi and Pirulli (2020) and Yan et al. (2023)) and scaled experiments (e.g., Scheidl et al. (2012); Cui et al. (2015); Armanini et al. (2019) and Song et al. (2021)). Debris flow impact forces have been defined as the combination of slurry and grain impact loading (Lei et al. (2018)). Moreover, slurry impact pressure studies can be classified into two groups: hydrostatic models and hydrodynamic models (Lichtenhahn (1973); Zanchetta et al. (2004)).

To mitigate the disasters, most of the previous researchers have focused on placing different dams as rigid barriers which were taken as structural prevention against debris flow disasters to trap the soiled materials. Also, the construction of a concrete baffle array is an alternative way to minimize the destructive effect of debris flow. In this kind of structure, the height, type and distance between each baffle play an essential role in mitigation purposes. In general, scientists prefer to perform numerical simulation or fieldwork to determine the performance of baffle structures (Ng et al. (2015); Bi et al. (2018); Wang et al. (2020); Yang et al. (2021); Deng et al. (2022); Kim and Yune (2022) and Kim et al. (2023)). Numerous studies have studied baffles constructed at slopes where granular flows were accelerated (Choi et al. (2015)) and at deposition zone where granular flows were decelerated (Wang et al. (2020)).

Like baffle array structure, a patch of trees can also contribute to reduce debris flow mobility and reducing the triggering capacity of the debris flow. The presence of the tree trunks increases the debris flow resistance, prevents debris flow from moving, supports the deposition of debris, and most importantly, reduces the maximum impact forces on structures (Fidej et al. (2015) and Bettella et al. (2018)). In addition, interest has recently been increasing in the study of tree trunks or vegetation in debris flow disasters to dissipate debris flow energy on their paths. The effect of trees on debris-flow deposits has been studied extensively in the past few years. Researchers have been studying how tree trunks (in cases of rigid vegetation) affect the flow patterns in rivers, streams, coastal dunes and floodplains (Mashud et al. (2011); Vargas-Luna et al. (2015); Türker et al. (2019) and Kumar et al. (2021)), but few studies investigated the effect of a patch of trees as a preventive measurement against debris flow disaster. The rigid vegetation or tree trunks exert drag forces against debris flow that can greatly reduce debris flow velocities near the bed (Liu et al. (2021)) and also can reduce suspended sediment transport and sediment erosion (Vargas-Luna et al. (2015) and Kang et al. (2022)). The majority of experimental and theoretical studies of cylinder arrays (representing vegetation canopies or tree trunk solid fraction) have been addressed for water flow. These research have consistently shown the effect of canopy density on the drag coefficient and water flow velocity (Tanino et al. (2008); Etminan et al. (2017); D'Ippolito et al. (2019); Chang et al. (2020); Mancheño et al. (2021) and Sohrabi et al. (2023)). Tree trunks increase flow resistance by exerting drag forces, as a result, the mean

debris flow velocity and bed shear stress were reduced so that the water levels become high. Additionally, the tree trunk forces the flow to move around, which changes the flow field around tree trunks (Nepf (2012) and Liu et al. (2016)). There is still an incomplete understanding of the morphologies of debris flow behavior, and fewer studies have addressed patches of tree structures and their interactions within debris flow material along with their travel distances.

The experimental analyses by considering the assumptions about the material concentration, particle size distribution and rheological parameters alone can be inaccurate in measuring the impact force of debris flows. A variety of factors might cause inaccuracies, including environmental conditions, human error during experiments, variations in the frequency of debris flows, and discrepancies in devices and testing methods. Therefore, making accurate numerical analysis and employing an analytic method can be effective ways to obtain accurate debris flow impact force. In the present work, an analytical investigation and a numerical evaluation were conducted to compare the behaviour of debris flow, its impact force and distribution when it encounters a rigid wall by comparing results from several previous large-scale and small-scale laboratory experiments. the amount of conservation of mass, momentum and energy that passes through the selected control volume was evaluated by the Reynolds Transport Theorem (RTT). The simulation results were analysed by FLOW-3D, a three-dimensional finite element model, that provides valuable insight into several physical flow processes. The Renormalized Group (RNG) based on k-epsilon model was used as a turbulence model. This model is the most precise, highly suitable and robust model for accurately simulating mass flow dynamics. To offer better coverage, it expands the capabilities of the standard k-epsilon model. Basically, the Navier-Stokes equations which describe the motion of fluids in three-dimensional space were solved and this gives the ability to measure the peak impact pressures on the rigid wall. The aim of this study is to determine the maximum impact pressure of debris flow over a rigid vertical wall, right after passing through different configurations of patches of tree trunks. For the development of effective measures, two different configurations were simulated. In one of the simulations the number of rows of tree trunks increased towards upstream, whereas, in the second configuration, the density of tree trunks increased within a predefined area.

2. METHODOLOGY

Debris flow is a function of Froude number (Fr), which is the ratio between the inertial and gravitational forces and was given as follows:

$$F_r^2 = \frac{u^2}{g\,H\cos\theta} = \frac{\rho u^2}{\rho g H\cos\theta} = \frac{\text{Inertial force}}{\text{Gravitational force}} \quad (1)$$

where u is debris flow velocity (m/s), g is the gravitational acceleration (m/s^2), H (h=H cosθ as depicted in Fig. 1) is the vertical flow depth (m), θ is the flume bed inclination.

Depending on the Fr the magnitude and the behaviour of debris flow changes. In this research, the numerical analysis is based on the experimental study performed by Cui et al. (2015) where the debris flow was examined under supercritical flow conditions; the Fr is always greater than 1.

The debris flow generally generates high kinetic energy named as the hydrodynamic impact force. This was initially studied by Hungr et al. (1984) and later by Armanini (1997), showing that the hydrodynamic impact force is proportional to both debris flow velocity and debris flow density, ρ. Hence the debris flow maximum impact pressure (P_{dmax}) equation was given as follows:

$$P_{dmax} = \alpha\rho\, u^2 \tag{2}$$

In which ρ is (kg/m3), and α is the empirical proportionality coefficient for hydrodynamic models that can be experimentally identified according to the type of debris flow. For instance, α =2.0 was suggested by Watanabe (1981) for laminar and fine aggregate debris flows, whereas values between 2.0 and 4.0 were measured by Egli (2005) for debris flows which mainly involve coarse aggregate. Values between 3 and 5 were reported after 70 field investigations of debris flow tests in China (Zhang (1993)).

Hübl et al. (2009) used dimensional analysis and proposed a method for estimating debris flow P_{dmax} against protecting structure expressed as:

$$\frac{P_{dmax}}{\rho u^2} = a\, F_r^b \tag{3}$$

Where the parameters of (a) and (b) are empirical factors and their values are between 4.9 to 5.62 and -1.66 to -1.29, respectively (Hübl et al. (2009)).

2.1. Momentum Conservation Law

2.1.1. Reynolds Transport Theorem

Based on the definitions given by Takahashi (1979); Chu et al. (1995) and Mangeney et al. (2010), a change in the momentum of the debris flow originates the impact impulse pressure on a rigid wall. The total forces per unit width that act on the control volume on the sloping bed in the x direction is:

$$F_{Tx} = \int_{L_x}^{L+L_x} \left[\bar{\rho} g\, \bar{h}\, sin\,\theta \; - k\bar{\rho} g\, \bar{h} \frac{d(h)}{dx} - \bar{\rho} g\; \bar{h} \tan\varphi\right] dx \tag{4}$$

Where φ represents the friction angle of the material, $\bar{\rho}$ represents depth-averaged debris flow density , $\bar{h}$ represents the average depth along the x-direction that is $\bar{h} = z_{top} - z_{bed}$, L represents the control volume length and L_x is the length of the flume upstream of the control volume. The angle of inclination of the bed slope was represented by θ. The first term is gravitational force which represents body force due to gravity that acts on the control volume, the second and third terms represent external force components, normal and tangential on the control volume (Fig. 1).

Solving Reynolds Transport Theorem to obtain the momentum flux model that is appropriate to define incoming momentum flux which flushes to downslope one obtains:

$$\bar{\rho}u_{in}^2\, h_{in} + \bar{\rho}g\, \bar{h}L\, sin\,\theta\ - k\bar{\rho}g\, \bar{h}L\frac{d(h)}{dx} - \bar{\rho}g\, \bar{h}L\tan\varphi = \bar{\rho}u_{out}^2\, h_{out} \quad (5)$$

where $\bar{\rho}u_{in}^2\, h_{in}$, ($\dot{M}_{in}$), and $\bar{\rho}u_{out}^2\, h_{out}$, ($\dot{M}_{out}$) are debris incoming and outgoing momentum flux per unit width, respectively, $h_{in} = H_{in}cos\theta$, $h_{out} = H_{out}cos\theta$, $\bar{\rho}g\,\bar{h}L\,sin\,\theta$ is the gravitational force (F_g) component per unit width, $k\bar{\rho}g\,hL\frac{d(h)}{dx}$ is the longitudinal pressure force (F_p) per unit width due to longitudinal variations in depth h, and $\bar{\rho}g\,\bar{h}\,L\tan\varphi$ is the basal friction force (F_{bs}) per unit width as illustrated in Fig. 1.

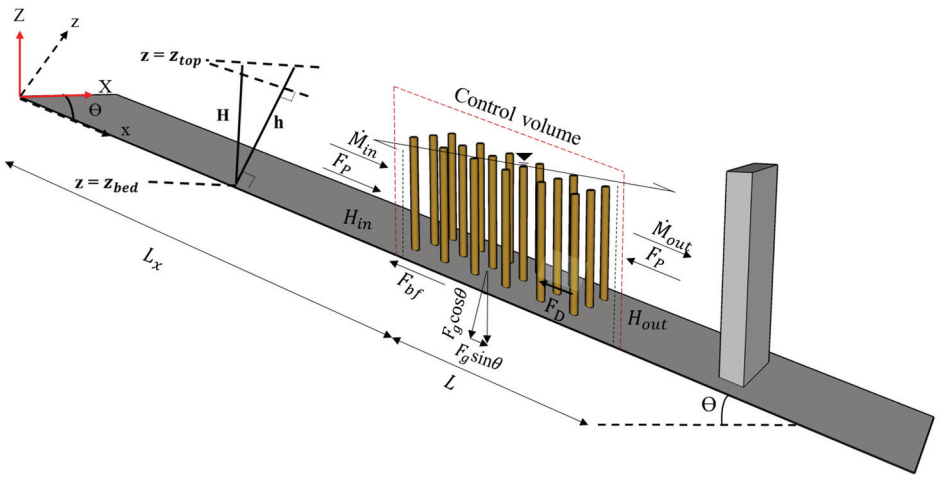

Fig 1 - Sketch of the flume geometry and the total forces that act on the control volume attributed to the tree trunk patches arrangement at an inclined bed with the angle of (θ).

3. MODEL PROGRESS

3.1. Drag Force

Nowadays, referring to the more specific reference of the field of rigid vegetation, rigid tree trunks have often been demonstrated by circular cylinders made of various materials either in experimental or simulation models. Due to the influence of the tree trunks against debris flow, the drag forces were exerted and can be expressed as $\sum_{i=1}^{N} F_D$ where N is the number of the tree trunks per unit plan area.

Formally, the depth integration of drag force for a single vertical cylinder with diameter d, from z_{bed} to z_{top} can be expressed as follows:

$$F_D = \int_{zbed}^{ztop} \frac{1}{2} C_D\, \bar{\rho}u^2 d\, \cos\theta\, dz \quad (6)$$

In which C_D is the drag coefficient and d being the tree trunk diameter.

By inserting Eq.6 into Eq.5, the momentum conservation equation applied along flow direction given in Fig.1 can be rewritten as:

$$\bar{\rho}u_{in}^2 h_{in} + \bar{\rho}g\,\bar{h}\,L\sin\theta - k\bar{\rho}g\,\bar{h}L\frac{d(h)}{dx} - \bar{\rho}g\,\bar{h}L\tan\varphi - \frac{1}{2}NC_D\,\bar{\rho}\bar{h}u^2 = \bar{\rho}u_{out}^2 h_{out} \quad (7)$$

3.2. Tree Trunk Patches Methods

Several studies have been conducted on the interaction between flow and rigid vegetation in the past (e.g., Liu et al. (2016) and D'Ippolito et al. (2021)), but a few studies have been done on the effect of drag exerted from various vegetation densities on debris flow (e.g., Liu et al. (2021)). Here, the tree trunk simulation analyses are based on two different scenarios. In one of the simulations, the density of tree trunks (λ) increased within a predefined area (Fig. 2), and in the second configuration, the vegetated length parameters (∅) (the number of rows of tree trunks) increased towards upstream (Fig. 3).

A geometric similarity ratio value of 1:50 was used for the tree trunk diameter in the simulation. The cylinder with a 1 cm diameter and 14 cm in length was used in the simulated flow (Cost (1979)). Tree trunk density without canopy was presented by gradually increasing the number of individual rigid tree trunk elements in the measuring plane area, in two different linear and rectilinear arrays (A1, A2, A3, A4, A5 and A6), Fig. 2. In this group model two significant parameters, λ and solid volume fraction (ψ), have been examined. Referring to emergent rigid vegetation for cylindrical elements with a constant diameter (d) of past experimental studies (Valyrakis et al. (2021); Wilson et al. (2003) and Nepf (1999)), and based on the frontal area of the individual rigid elements per unit volume, the λ can be defined as the ratio of the projected rigid tree trunks plan area to the total volume:

$$\lambda = \frac{dh}{s_i^2 h} = \frac{d}{s_i^2} \quad (8)$$

where s_i represents the distance between adjacent individual tree trunk elements. The ψ is the ratio of the areal coverage of the tree trunk elements to the portion of measuring area covered by tree trunk elements previously defined by Türker et al. (2006), and expressed as:

$$\psi = N\,\frac{\pi d^2}{4\Delta X\,\Delta Z} \quad (9)$$

where ΔX is the horizontal distance, ΔZ is the vertical distance in measuring the plane area and N is the number of tree trunks in the area of concern. Two scenarios were proposed for determining the P_{dmax} applied by debris flow on vertical walls. The first scenario covers six different configurations in which linear and rectilinear patches of tree trunks were examined. The tree trunk densities and ψ ranging from λ = 1.3 m^{-1}, for the linear arrangement model A1, to λ = 44.4 m^{-1}, and for the rectilinear arrangement defined as configuration A6, (Table 1).

Table 1 - Plan view of cylinder tree trunks arrangement in simulation model

Model group A						
	Tree trunk arrangement	Horizontal distance on measuring plane ΔX (cm)	Vertical distance on measuring plane ΔZ (cm)	Tree trunk distance s_i (cm)	Solid volume fraction (ψ) %	Tree trunk density λ (m^{-1})
A1	Linear	10	8	10	1	1.3
A2	Rectilinear	10	8	6	1.96	2.8
A3	Linear	10	8	5	3.9	4
A4	Rectilinear	10	8	3	7.8	11.1
A5	Linear	10	8	2.5	15.7	16
A6	Rectilinear	10	8	1.5	31.4	44.4
Model group B						
		Tree trunks spacing perpendicular to debris flow direction ΔX (cm)	Tree trunks spacing parallel to debris flow direction ΔZ (cm)	Tree trunks diameter d (cm)	Number of rows N_r	Vegetated length parameter $\emptyset$
B1	Linear	4	5	1	1	0.04
B2	Linear	4	5	1	3	0.12
B3	Linear	4	5	1	5	0.2
B4	Linear	4	5	1	8	0.31
B5	Linear	4	5	1	12	0.47
B6	Linear	4	5	1	17	0.67

The second scenario has been examined with six different configurations in which the number of rows used for the tree trunks increased towards the upstream side of the flume. The first configuration is run with one row of tree trunks (B1) and then the number of rows increased to 3, 5, 8, 12 and 17 in the following configurations (Fig. 3.); spacing between each tree trunk was adjusted to ΔX =4 cm in the orthogonal direction to the flume direction and ΔZ =5 cm along the flume directions.

The dimensionless $\emptyset$ (Türker et al. (2019)) was obtained by the ratio of the volume of a single vegetation element in a unit area to the total volume of the unit area. The dimensionless $\emptyset$ varied between 0.04 and 0.67 as shown in Table 1. The $\emptyset$, based on its definition, was calculated as given in Eq 10.

$$\emptyset = N_r \frac{\frac{\pi}{4} d^2 h}{\Delta x \, \Delta z \, h} = N_r \frac{\pi d^2}{4 \, \Delta x \, \Delta z} \tag{10}$$

Where N_r is the row number of tree trunks and h represents the height of the tree trunk.

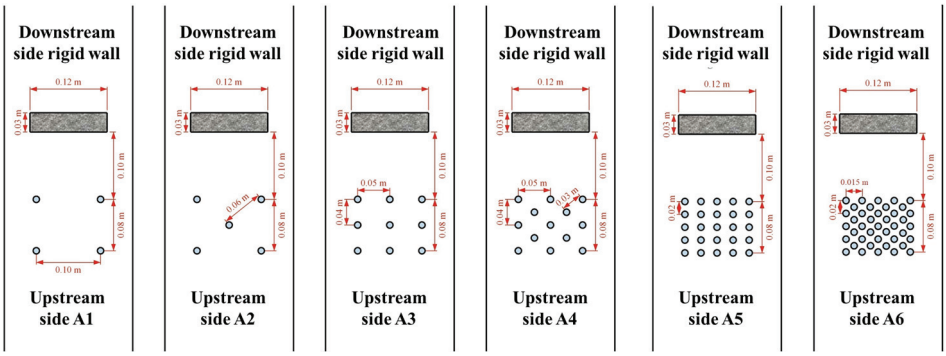

Fig 2 - The top view of the six different linear and rectilinear patches of tree trunk arrangements for model group A (A1, A2, A3, A4, A5 and A6).

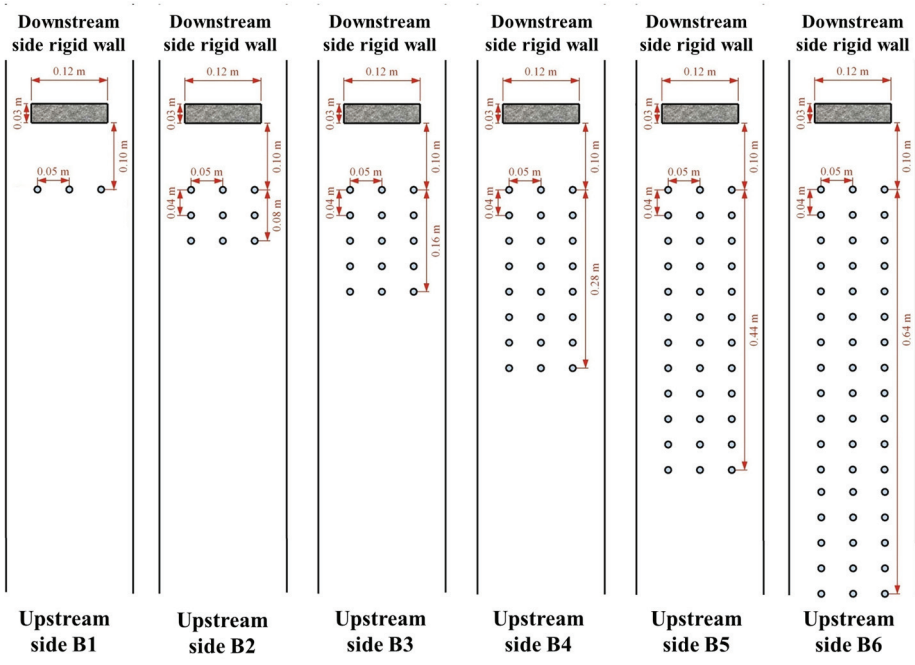

Fig 3 - The top view of the six different linear patches of tree trunk arrangements for model group B (B1, B2, B3, B4, B5 and B6).

4. MODEL SETUPS

The simulation results were performed by FLOW-3D, a three-dimensional finite element model. Continuity and momentum equations together with the finite volume method were used to solve the RANS equations.

4.1. Particle Size Distribution

According to data extracted from Cui et al. (2015), the materials that were used as input data for the model contained 2.9% clay, 5.1% silt, 37% sand, and 55% gravel. The ρ is 2074 (kg/m³) with a water concentration of 0.35 and a total volumetric concentration of 0.63. Consequently, the volumetric concentrations for clay, silt, sand, and gravel are 39.1 (kg/m³), 68.7 (kg/m³), 498.8 (kg/m³), and 741.4 (kg/m³), respectively. The cumulative percent passing of grain size, represented in Fig. 4, was employed as input data for defining debris flow particle size. As shown in the graph, the maximum particle size is 20 mm. To achieve the same material contents of the different grain size diameters that align with experimental data, four different gravel contents of 6%, 5%, 29%, and 15%, with diameters of 16 mm, 12 mm, 8 mm, and 3 mm were applied in the model respectively. Additionally, four different sand contents of 11%, 9%, 14%, and 3%, with diameters of 1.75 mm, 0.9 mm, 0.375 mm, and 0.11 mm were assigned respectively. Furthermore, for the silt and clay contents, percentages of 5.1% and 2.9% with diameters of 0.04 mm and 0.002 mm were respectively applied in the model.

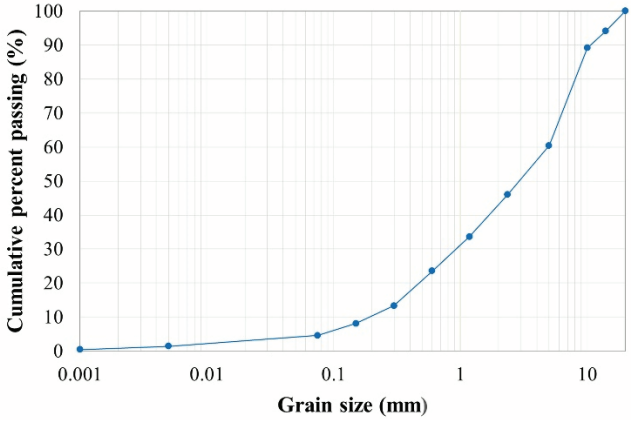

Fig 4 - Debris flow cumulative grain size distribution.

4.2. The Geometry and Boundary Condition of Numerical Analysis

In analysing debris flow impact force, crucial factors were selected with reference to previous studies. The simulated flume is 300 cm long and 20 cm wide with an inclination angle of 15° which was shown in Fig. 5. The 3 cm thick wall was placed at the end of the flume. The height of the wall is 25 cm, and its width is 12 cm. The debris material was flushed down by a gate with a 20x20 cm^2 area, placed at 50 cm from the top of the flume as a flow inlet. To measure the debris flow impact pressure, 18 measurement points (historical probes) were applied and positioned on the wall at different vertical heights: 1.5 cm, 4.5 cm, 7.5 cm, 10.5 cm, 13.5 cm, and 16.5 cm from the bottom of the rigid wall.

A wall boundary type was assigned to X_{min}, Y_{min}, Y_{max} and Z_{min} since there is no outflow in that region. On the other hand, outlet flow was applied at X_{max}, and a symmetry boundary type was assigned at Z_{max} as illustrated in Fig. 5.

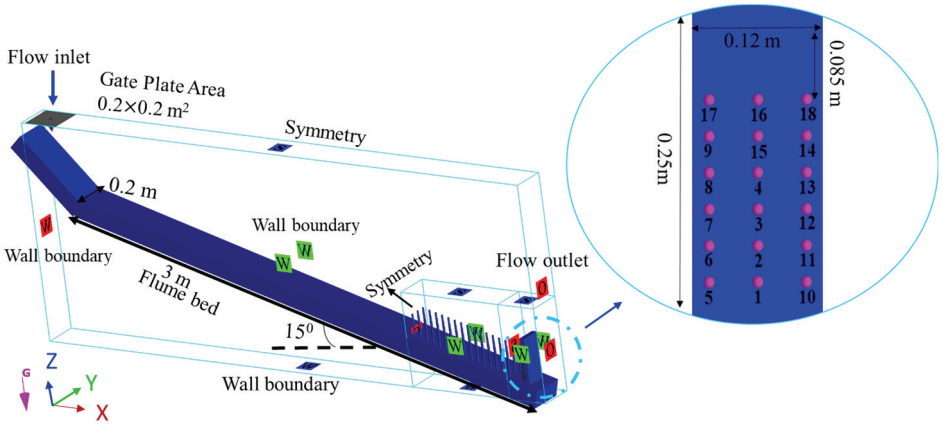

Fig 5 - Debris flow simulation model Geometry with various boundary condition types and 18 measurement points (historical probes) on the rigid wall.

As part of setting up the model, all material contents were applied in the fluid initialization, and material diameters were specified in the physics of the model as the sediments scour window. In the mass momentum source window, the debris flow geometry and properties were performed, including details such as the shape (a square with dimensions of 20 x 20 cm²), flow direction (oriented along the z-axis), and rotation (a 180-degree rotation in the y-direction). This configuration is depicted in Fig. 5, which represents the flow geometry at the inlet flow. To achieve the same debris flow discharge as the experimental results, the flow rate was programmed as 0.11 (m^3/s) between the time (0 - 2), 0.05 (m^3/s) between the time (2 – 2.5), 0.01 (m^3/s) between the time (2.5 – 3.1), 0.005 (m^3/s) between the time (3.1 – 4), 0.001 (m^3/s) between the time (4 - 5), 0.0001 (m^3/s) between the time (5 - 8) and zero for time 8 (sec). The debris flow characteristics and input data used in the simulation model are listed in Table 2.

The cartesian meshes were generated using the nested multi-block grid mesh in FLOW-3D to minimise the model memory usage and runtime. Several meshes were tested in the simulation model to ensure that the numerical solution remains consistent and does not significantly change with different grid settings. Due to dealing with elements of different sizes, both uniform and non-uniform Cartesian mesh sizes were defined in the geometry. A uniform Cartesian mesh cell size of 0.005 m was used as finite meshes for the entire area. To improve mesh size precision for the tree trunk area and rigid wall, two different non-uniform block meshes were employed as illustrated in the Fig. 6.

In block (a), the cell counts 100 and 200 were applied in both y and z directions for all group models A and B, respectively. However, due to different configurations in the x direction for group models A and B, the cell counts of 200 were allocated to the B6 model, the longest tree truck rows, in the x direction which indicated the average mesh sizes of 0.002 m. To provide uniform precision for all group models A and B, a ratio of 308 cell counts per meter was applied. Furthermore, in block (b), cell counts of 100 were assigned in the x, y, and z directions for all group models. The total number of real cells for all mesh blocks is 11474000. To increase the usefullness of results in FLOW-3D, the size ratio between the

adjacent cells should be close to unity as much as possible and must not exceed 1.25. Moreover, aspect ratios of the cells should also approximate unity as much as possible, and not exceed 3.0 because cell aspect ratios exceeding 3.0 can cause pressure iteration problems. Furthermore, all degrees of freedom for cells at all the sides (x, y and z) and bottom were fixed as shown as mesh planes in Fig. 6.

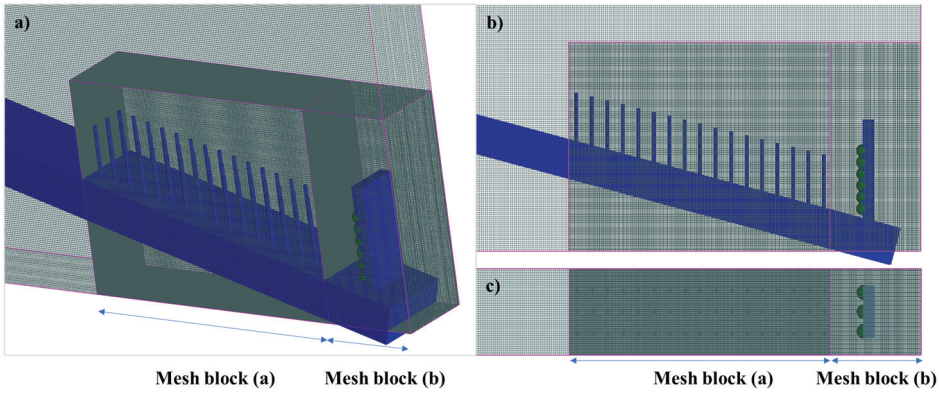

Fig 6 - Computational mesh grid in the control volume of the simulated model with two different adding mesh block (a) and (b): section a) 3D view, section b) side view and section c) top view.

Table 2 - Debris flow simulation input variable

Parameters	***Value***
Specific gravity (Gs)	2.65
Flume inclination angle (degrees)	15
Average grain diameter d_{50} (m)	0.0027
Dynamic Viscosity (Pa s)	0.096
Yield stress (Pa)	30.32
Fluid viscosity (kg/m/s)	*0.001*
Debris flow fluid density (kg/m^3)	*2074*
Friction angle (degrees)	32
Water concentration	0.35
Sediment volume concentration	0.63
Total debris flow volume (m^3)	0.23

5. VALIDATION OF THE TOTAL IMPACT FORCES

The debris flow simulation analysis validation conducted with and without sediment particle (clean water) distribution using the experimental results of Cui et al. (2015). Based on their

experiment, the length of the flume is 300 cm, the width is 20 cm, and the inclination angle is 15°. Five impact measurement points (historical probes) S1 to S5 were located at the end of the flume. These points were placed on the wall at 1.5 cm, 4.5 cm, 7.5 cm, 10.5 cm, and 13.5 cm vertical depths from the bottom of the wall. In their experiments, the flow impact pressure processes can be considered into three stages. First, there is a strong impact at the head of the debris flow, followed by a steady impact along the body, and finally, there is a sliding flow at the tail. Due to the lower impact pressure in the debris flow tail, only the initial two steps were considered by them as the impact pressures. Consequently, the impact pressure measured at 10.5 cm and 13.5 cm heights were excluded from their calculations.

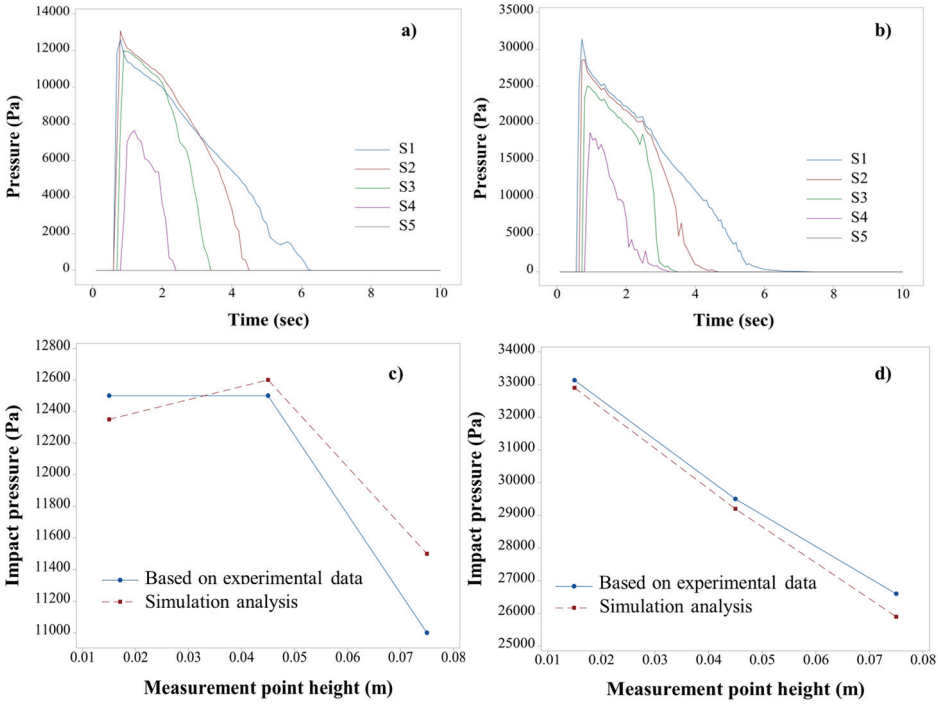

Fig 7 - Impact pressure determination for different measurement points (1.5 cm, 4.5 cm, and 7.5 cm above the flume bed) that placed at different height, (a) clean water, (b) debris flow and validation of experimental data based on simulation analysis for (c) Clean water and (d) Debris flow.

Based on the simulation and experimental results, both clean water and debris flow impact pressures do not reach point S5 in terms of height. The velocity of the clean water is estimated at 4.9 m/s, Fr is 5.2 and the P_{dmax} is 12.6 kPa (Fig. 7-a). Using the input parameters provided in Table 2 for water with sediment particles, the respected values were u of 4.1 m/s, Fr of 3.8, and P_{dmax} of 32.9 kPa (Fig.7-b). The impact pressure process at the first measurement point S1 was sustained for about 6 seconds and other points was sustained for 3-4 seconds. Fig. 7-c and -d show the comparison between experimental data and simulation results in three different measurement point heights; 1.5 cm, 4.5 cm, and 7.5 cm from the flume bed.

In clean water, the percentage error of the simulated analyses is less than 2% for the first and second heights, and below 5% for the third height compared to the experimental results. Similarly, in the debris flow the percentage error of the simulated analyses at each height is less than 2% of experimental results. As a result, the MSE is 0.09 for clean water and 0.13 for debris flow. Therefore, the findings are in good agreement with the experimental observations.

The analytical results obtained from Eq.4 were validated by using experimental data from Cui et al. (2015). In their experiment, they conducted a total of 27 tests, with a range of Fr variation between 2.5 and 5.9. Subsequently, these results were compared with 155 tests of previous data with Fr between 0.5 and 10.8 by Hübl and Holzinger (2003); Tiberghien et al. (2007) and Scheidl et al. (2012) and field experiment analyses by Costa (1984) and Zhang and Yuan (1985). In this study, subcritical flow data (Fr<1) have not been included in comparison. The result of the regression hydrodynamic model derived by Cui et al. (2015) was expressed in Eq.11 and was given in Fig. 8:

$$\frac{P_{dmax}}{\rho\, u^2} = 5.3\, Fr^{-1.5} \tag{11}$$

The impact pressure analysis data from Cui et al. (2015) were inserted into Eq. 4 and the results were plotted on the power line with a regression error square (R^2) of 0.95 to show that the results matched with the previous studies. Based on these ranges the dimensionless empirical coefficient, α is analytically calculated to be in the range of 0.4 and 1.86.

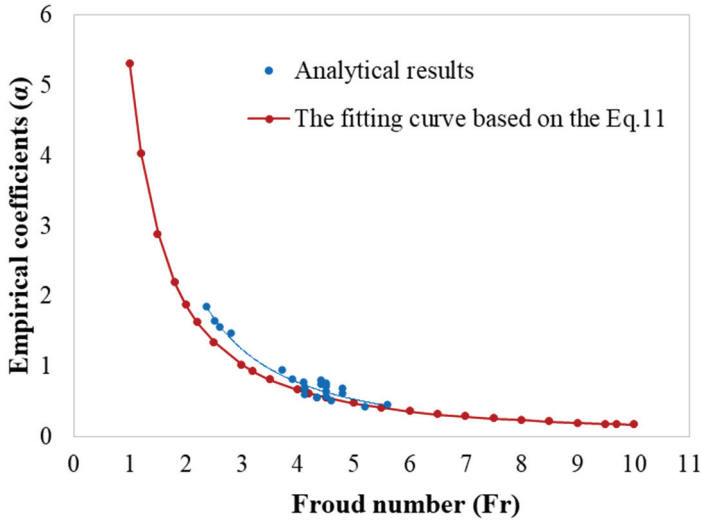

Fig 8 - Relationship between empirical coefficients and the Fr based on Analytical and experimental results

5.1. Impact Pressure Simulation

Twelve model tests were performed with different tree trunk arrays in both linear and rectilinear directions. All forces per unit meter were measured with specified density, tree trunk diameters, and distances. The results are shown in Table 3. The momentum flux leaving the control volume of the vegetated area generates pressure on the vertical wall. Eighteen measuring points (S1 to S18) have been used to assess impact pressure on the wall. Each point was arranged to have a 3 cm vertical and 4 cm horizontal distance from each other. Variation of impact pressures at S1, S2, S3, S4, S15 and S16, that were placed at different depths for both A4 and B5 models, as a function of time are depicted in Fig. 9 and Fig. 10. It can be noted that, with the increase of tree trunks against the debris flow path, the duration of the rigid wall impact pressure also increases. For instance, approximately 9 to 10 seconds were estimated to be sustained for A4 and 8 to 9 seconds for B5 as indicated in Fig. 9 and 10. The arrival time of peak impact pressures based on the effect of tree trunks was shown in Table 3, where peak impact pressure arrival times were changed from 0.76 to 1.2 seconds for group model A and from 0.76 to 0.9 seconds for group model B.

Table 3 - Numerical results for both group models A and B.

Group models A										
Solid volume fraction (ψ) %	Peak Impact arriving Time (sec)	Depth H_{out} (cm)	Velocity u (m/s)	Froude number	$\dot{M}_{in}$ (kN/m)	F_D (kN/m)	F_g (kN/m)	F_p kN/m)	F_{bs} (kN/m)	$\dot{M}_{out}$ (kN/m)
1	0.76	14	4.6	3.93	47.8	2.2	0.60	0.62	1.45	44.1
1.96	0.8	16.5	3.9	3.06	47.8	20.8	7.10	0.74	1.71	31.6
3.9	0.8	15.2	4.2	3.48	47.8	8.7	0.68	0.70	1.64	37.4
7.8	1	18.9	3.4	2.49	47.8	29.1	8.15	0.84	1.97	24
15.7	1	17.2	3.7	2.87	47.8	23.6	7.41	0.77	1.79	29
31.4	1.2	25.4	2.5	1.61	47.8	41.5	10.90	1.13	2.63	13.4
Group models B										
Vegetated length parameter, ø	Peak Impact Arriving Time (sec)	Depth H_{out} (cm)	Velocity u (m/s)	Froude number	$\dot{M}_{in}$ (kN/m)	F_D (kN/m)	F_g (kN/m)	F_p kN/m)	F_{bs} (kN/m)	$\dot{M}_{out}$ (kN/m)
0.04	0.76	14.7	4.4	3.6	47.8	6.5	0.70	0.73	1.69	39.6
0.12	0.8	15.2	4.2	3.5	47.8	8.7	0.68	0.70	1.64	37.4
0.2	0.9	16.1	4.0	3.2	47.8	12.9	0.72	0.75	1.74	33.1
0.31	0.9	17	3.8	2.9	47.8	16.2	0.76	0.79	1.84	29.7
0.47	0.9	17.1	3.8	2.9	47.8	16.4	0.77	0.79	1.85	29.5
0.67	0.9	17.1	3.8	2.9	47.8	16.4	0.77	0.79	1.85	29.5

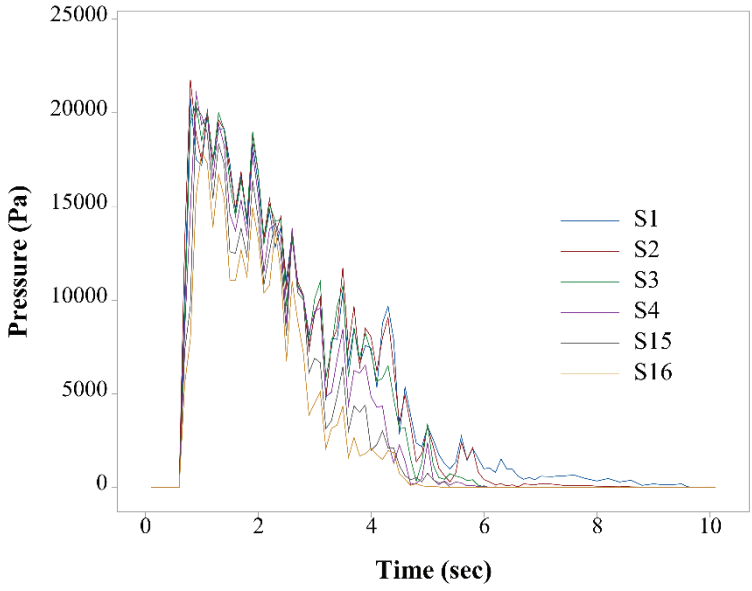

Fig 9 - Debris flow impact Pressures at measurement points (S1, S2, S3, S4, S15 and S16) were placed at different depths for model A4.

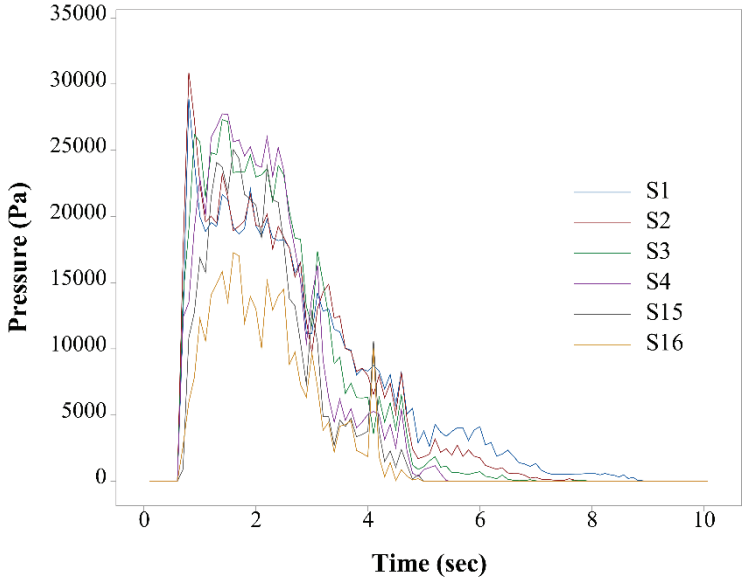

Fig 10 - Debris flow impact Pressures at measurement points (S1, S2, S3, S4, S15 and S16) were placed at different depths for model B5.

Fig. 11 and 12 show the front view impact pressure distribution along the rigid wall models A and B. It can be seen that for group model A (linear and rectilinear), P_{dmax} was concentrated between 4.5 to 10.5 cm above the floor. As ψ increased, independent of linear or rectilinear configurations of tree trunks, the effect of impact pressure decreased. When the maximum impact pressures at A1 are compared with the max impact pressures at A6, a reduction of 67.3%, 69.5% and, 70% in maximum pressures were observed at S4, S3, and S2, respectively. Another important observation is the increase in the depth of flow in parallel to the increase in ψ. Due to the velocity retarding effect (drag force effect) of the tree trunks, there is a reduction in u from 4.6 to 2.5 (m/sec) in the flow direction. Based on the principles of continuity, a decrease in velocity increases the flow area, which in turn increases the depth of the debris flow; depth increased from 14 cm to 25 cm. Consequently, the reduction in the velocity did not change the regime of the flow and the supercritical flow properties dominate the flow. However, as is seen in Fig. 11, a considerable increase in maximum impact pressures at the top of the wall was observed due to the rise in the debris flow depth. The retarding effect of tree trunks on the occurrence time of peak impact pressures was given in Fig. 11 indicates a 58% shift in the occurrence time of peak impact pressures.

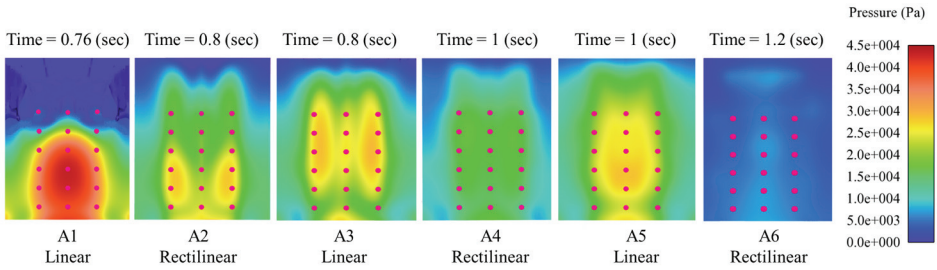

Fig 11 - The pressure distributions in the 18 measurement points on the rigid wall for group models A with various λ (1.3, 2.8, 4, 11.1, 16 and 44.4, m^{-1}) and ψ (1, 1.96, 3.9, 7.8, 15.7 and 31.4, %).

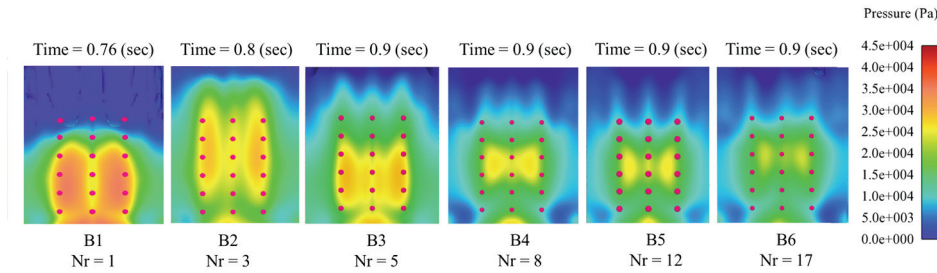

Fig 12 - The Pressure distributions in the 18 measurement points on the rigid wall for group models B with various Ø, (0.04, 0.12, 0.2, 0.31, 0.47 and 0.67).

The simulation for model B configurations clearly depicted the effect of drag on the debris flow. The in-line ordered trunks providing an easy path for debris flow to reach the wall caused maximum impact pressures. On the other hand, as the ∅ increased, the pressure dropped in the projection of tree trunks. Simulated peak pressures on the wall were 39 kPa in model B1 and 29 kPa in model B6. Approximately, a 34% reduction in peak impact pressure is not as good as the results achieved in Model A simulations. A significant reduction in debris flow velocity is not observed as in the case of model A simulations. As the ∅ increases from 0.04 to 0.67, a slight decrease, from 4.4 m/s to 3.8 m/s, in u was observed. Meanwhile, the flow depth increased from 15 cm to 17 cm. Consequently, the necessary time required to observe the occurrence of peak impact pressures on the wall did not vary much (Fig. 12).

5.2. Normalized Drag Coefficient

There are several studies that define the drag force and coefficient based on various assumptions. Some of them ignore the dominant effect of the Reynolds number (e.g. Riazi and Türker (2019)) while some assume that the drag force is linearly changing with flow velocity (e.g. Türker and Valyrakis (2021)). Implementing the drag force concept on linearly and randomly distributed trees based on using a quadratic drag law it was concluded that the variation in drag force increases as the λ increases. For the analyses of C_D along an individual tree trunk, the drag force equation (Eq. 5) can be given as:

$$C_D = \frac{2F_D}{\bar{\rho}u^2 dH} \tag{12}$$

in which H is debris flow depth. Based on the data given in (Table 3), under the assumption that debris flow velocity, debris flow density and tree trunk area are constant at the entrance of control volume, the magnitude of C_D will vary as the tree trunk ψ and ∅ change. Therefore, the C_D increases as the number of tree trunks increases. In other words, C_D in a normalized form should take into consideration the amount of tree trunks. Hence, based on this observation, for the assessment of the normalized drag coefficient (C_{DN}) associated with the debris flow resistance due to rigid tree trunks the following expression was proposed:

$$C_{DN} = C_D \times \eta \tag{13}$$

where η is the mean value of the correlation drag coefficient for each different λ.

There are several different methods to define the tree trunk C_D for the group tree trunk model in which C_D is not the same as a single tree trunk and has typically been modified to increase with λ (Nepf (1999); Tanino and Nepf (2008); Kothyari et al. (2009); Stoesser et al. (2009)).

The drag force was equally distributed within the control volume among the different tree trunks to examine drag coefficients.

The graph in Fig. 13 shows the variation of C_{DN} with various row numbers, Nr. The values of η and C_{DN} for the six different group model B are in the range of about 1.0-2.5 and 0.2-1.2 (Table 4). The graph exhibits that C_{DN} increases with an increase in row numbers and

eventually assumes a maximum value. This could be due to the possibility that the debris flow became fully developed after a certain length of vegetation array.

The nonlinear regression equation describing the change in C_{DN} with respect to the number of rows was given in Eq. 14 with a mean square error (MSE) of 0.03 and the standard error of the regression (S) of 0.18. Equation 14 was derived to describe the C_{DN} valid for the simulation performed in this study.

$$C_{DN} = 1.2 - 1.44\exp(-0.24N_r) \quad (14)$$

Table 4 - Results of C_D, η and C_{DN} with different ψ number of rows

	C_D	η	C_{DN}
(ψ) %		**Group model A**	
1	0.07	1.0	0.1
1.96	0.62	9.4	5.9
3.9	0.44	6.6	2.9
7.8	0.87	13.2	11.5
15.7	0.71	10.7	7.6
31.4	`1.24	18.8	23.3
N_r		**Group model B**	
1	0.20	1.00	0.2
3	0.26	1.32	0.3
5	0.39	1.96	0.8
8	0.49	2.46	1.2
12	0.49	2.49	1.2
17	0.49	2.49	1.2

The values of η for linear group model A are in the range of about 1 to 10.7 and for rectilinear group model A are in the range of 9.4 to 18.8 (Table 4). The graph in Fig. 14 shows the variation of C_{DN} with various ψ for linear and rectilinear tree trunk models. The C_{DN} increases with increasing the number of tree trunks within a predefined area in both linear and rectilinear models. As illustrated in Fig. 14, the increase in rectilinear models is more pronounced compared to the linear model.

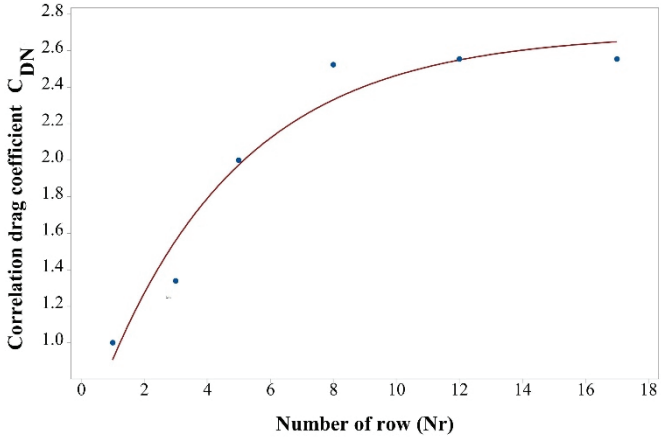

Fig 13 - Variation of C_{DN} with various row numbers (Nr) for group model B.

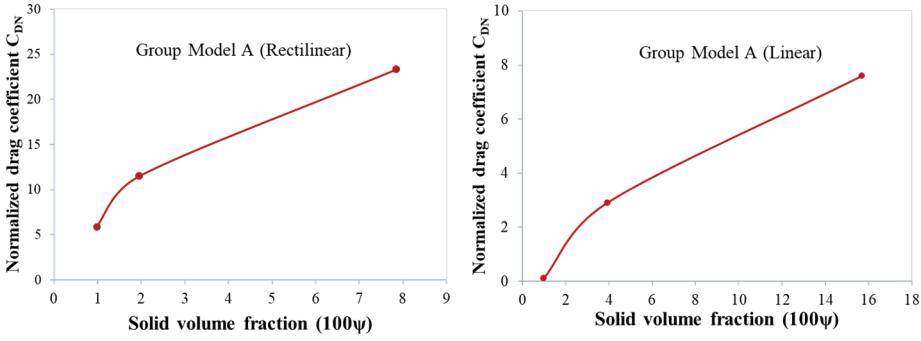

Fig 14 - Variation of C_{DN} with various ψ for group model A (Linear and Rectilinear).

To assess the influence of tree trunks on C_{DN} more completely, the normalized regression equation was defined as a function of the Fr and ψ for group model A and N_r for group model B as follows:

$$C_{DN} = 39.69 - 0.33\ln(100\psi)^{0.002} - 30.38\ln(Fr)^{0.85} \quad (15)$$

$$C_{DN} = 7.45 - 0.12\ln(N_r)^{0.72} - 5.63\ln(Fr)^{0.99} \quad (16)$$

These equations imply that drag coefficients have a weak dependence on tree trunks ψ fractions and row numbers as compared Fr. The agreement between the the proposed equations and estimated C_{DN} values is satisfactory as shown in Fig. 15.

Several factors affect the hydrodynamic empirical coefficient; the characteristics of a basin, the features and properties of debris flows, and intensity of rainfall. Previously obtained debris flow experimental results show that the hydrodynamic empirical coefficient can be

estimated within the range of (2.8–4.4) (Lichtenhahn (1973)), (2.5–7.5) (Scotton and Deganutti (1997)) and (0.45-2.2), (Armanini (1997)).

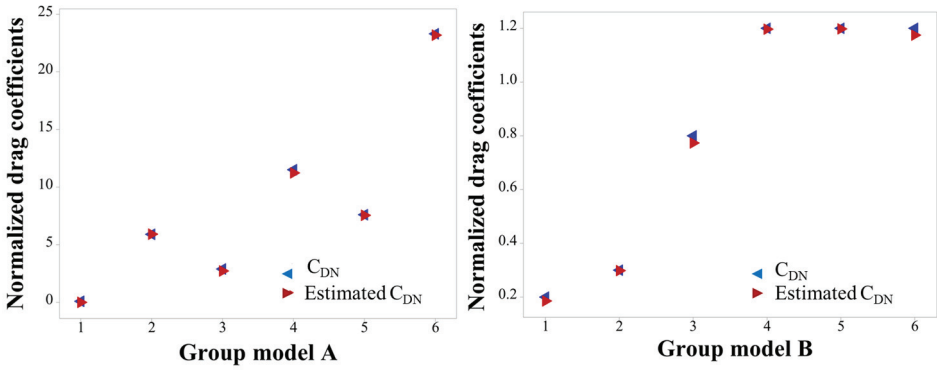

Fig 15 - Comparison between the C_{DN} and the estimated C_{DN} based on the results which obtained from Eq. 15 and Eq. 16 for both group models A and B.

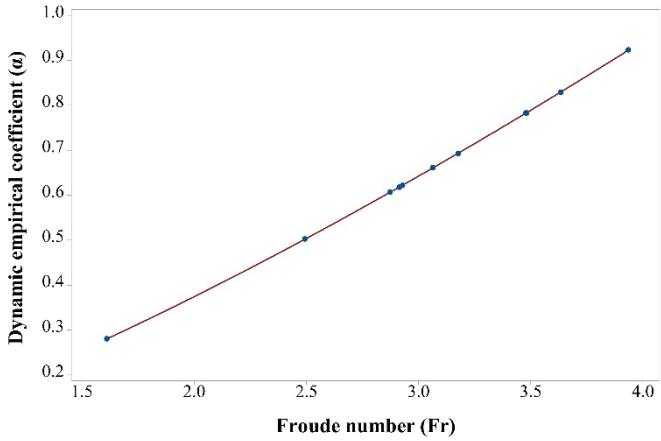

Fig 16 - Relationship between the Fr and dynamic empirical coefficient (α)

The magnitude of hydrodynamic empirical coefficient, α, has been assessed experimentally by using a flume to evaluate the impact force of debris flow as explained above. Fig. 16 depicts the variation of the dynamic empirical coefficient, α, as a function of Fr. In the present work, the presence of tree trunks increases the resistance forces, and the empirical coefficient was estimated to be in the range of (0.28–0.92) for the range of Fr varying between 1.6 and 3.9. Referring to Eq. 3, by having a new finding of P_{dmax}, the following hydrodynamic model with mean square error (MSE) 0.0004 and the standard error of the regression (S) 0.006 were introduced as:

$$\alpha = 0.15F_r^{1.33} \quad (17)$$

6. DISCUSSION

Based on the analytical and numerical calculations, the ratio between pressure forces and inertia forces which is the dynamic empirical coefficient, α, has been modified for the cases where the protection of patch of tree trunks was present (Eq. 17). In this study, the values of a and b were determined as 0.15 and 1.33, respectively. As a result, the relationship between Fr and dynamic empirical coefficient follows a power law. However, under normal conditions (without any mitigation techniques) which have been studied previously, the value of a ranges from 4.9 to 5.62 and the value of b ranges from -1.66 to -1.29, indicating that the Fr and α are inversely proportional (Hübl et al. (2009) and Cui et al. (2015)).

This result reveals the effect of the patch of tree trunks on reducing the magnitude of inertia forces. Such reduction reduces the Fr, therefore, to reduce α, since inertia force ρu^2 is decreasing, P_{dmax} should also be decreased. This can only be satisfied if the constant b is positive, 1.33. This result suggests that in the case of protective mitigation, the magnitude of b should be positive.

Implementation of the baffle array is a similar artificial technique to mitigate debris flow disasters. Studies conducted by Bi et al. (2018), Wang et al. (2020) and Yang et al. (2021) demonstrated that the baffle row numbers, column spacing, and row spacing all have significant influences on the baffle energy dissipation. According to their results, increasing the number of baffle rows and spacing increases baffles energy dissipation capacity which indicates the reduction in the debris flow velocity. Also, Ng et al. (2015) investigated the effects of baffle spacing and row numbers and their experimental results depicted reduced u by increasing the number of rows of baffles. By increasing from one row to three rows, u was reduced by 57 %. In this study, a reduction in the debris flow velocity is also observed. However, the reduction is not as high as in baffle cases but is up to 47% in the A type models and 21% for the B type models. Such a result indicates that natural mitigation methods might not be as successful as artificial ones but still can reduce risks generated by debris flow. In addition, Zhang et al. (2021) worked out the effect of baffle arrays at the acceleration stage of the granular flow and according to their results, u was reduced by 78.82%.

Many studies have recently investigated the C_D exerted by cylindrical arrays in the case of water flow. These findings examined flow patterns similar to the results investigated for debris flow in this study. Studies conducted by Tanino et al. (2008); Etminan et al. (2017); Chang et al. (2020); Mancheño et al. (2021) and Sohrabi et al. (2023) showed that by increasing ψ, the C_D increases and consequently the drag force increases. Also, D'Ippolito et al. (2019) investigated that by increasing λ, C_D increases by 50 %. Since the debris flow density is higher than the water flow, the results of this study indicated the C_D increases by 90% and 59% in both grope models A and B, respectively.

At the same time, some studies were made to examine the variation of exerted drag force with the effect of blockage and sheltering (Li and Shen (1973); Schoneboom et al. (2011); Etminan et al. (2017) and Liu et al. (2020)). From the perspective of the blockage and sheltering effect, the finding of this study have also been validated by those results. Etminan et al. (2017) and Liu et al. (2020) found that the blockage effect with high vegetation densities had a greater impact on reducing C_D than sheltering effects in rectilinear configurations. However, in the linear configuration with the constant blockage ratio, the sheltering effect

showed more strength, which was evidenced by parallel findings regarding the blockage and sheltering effects observed in this study.

In this study, the rectilinear configuration of tree trunks in each spot area was more effective than other configurations. When the maximum impact pressures at A1 were compared with the maximum impact pressures at A6, a reduction of 67.3%, 69.5% and, 70% in maximum pressures were observed at S4, S3, and S2, respectively and a 34 % reduction in peak impact pressure for model B.

For group model A (linear and rectilinear), the P_{dmax} concentration appears in a different region of the wall. The variation of impact pressure concentration is similar to the damaged regions of the wall. There is a relatively high impact pressure region over the wall from S1 to S4 in A1 (linear model). Increasing the tree trunk arrangements from A2 to A6 gradually reduces the effect of P_{dmax} and expands its effect to a large area, therefore, the damaged regions were altered.

Future research should focus on studying the debris flow velocity field, with a particular concentration on the debris flow surfaces and developing methods to determine the velocity field around patches of tree trunks.

7. CONCLUSION

The study focused on the effect of debris flow peak impact pressure on a vertical wall which has been analysed under the protection of a patch of tree trunks. Both numerical simulation and the analytical model have been applied and validated.

Based on research findings, the following conclusions were drawn:

1. The numerical simulation results depicted that increasing λ within a given spot area is 50% more protective than the increase in the number of rows of tree trunks.
2. An increase in λ is also effective in retarding the occurrence period of the peak flows in model A around 58%. For model B, since only the number of rows is increased, it has changed by 18.4% up to the B3 model (five tree trunk rows); its increase has not affected on occurrence period of the peak for the other models at all. Thus, based on the results of the eight, twelve and seventeen rows of tree trunks investigation, the design basis for the five rows of tree trunks was suggested for model B.
3. The P_{dmax} is concentrated between 4.5 and 10.5 cm above the floor.
4. Based on the analytical calculations the C_D has been developed as a function of Fr and the new dynamic empirical coefficient α has been modified based on the analytical results.
5. The C_D was defined as a function of Ø and ψ. Accordingly, the presence of patches of tree trunks plays a significant role in reducing debris flow impact pressure and thus minimizing the hazard risks. It is clear that accurate numerical analysis and analytic methods can be effective in obtaining accurate debris flow impact force simulations. This study can be improved and developed by using different sediment and water concentrations to test the P_{dmax} on the walls. In addition, this study can be improved by using an experimental system, such as the physical model of the

prototype, and converting the findings to values likely to be encountered in nature in future studies.

References

[1] Areas NRC (US). C on M for PM (1982) Selecting a methodology for delineating mudslide hazard areas for the National Flood Insurance Program. National Academies

[2] Armanini A (1997) On the dynamic impact of debris flows. In: Recent developments on debris flows. Springer, pp 208–226

[3] Armanini A, Rossi G, Larcher M (2019) Dynamic impact of a water and sediments surge against a rigid wall. J Hydraul Res

[4] Bagnold RA (1954) Experiments on a gravity-free dispersion of large solid spheres in a Newtonian fluid under shear. Proc R Soc London Ser A Math Phys Sci 225:49–63

[5] Bettella F, Michelini T, D'Agostino V, Bischetti GB (2018) The ability of tree stems to intercept debris flows in forested fan areas: A laboratory modelling study. J Agric Eng 49:42–51

[6] Bi Y, Du Y, He S, et al (2018) Numerical analysis of effect of baffle configuration on impact force exerted from rock avalanches. Landslides 15:1029–1043

[7] Chang W-Y, Constantinescu G, Tsai W-F (2020) Effect of array submergence on flow and coherent structures through and around a circular array of rigid vertical cylinders. Phys Fluids 32

[8] Choi CE, Ng CWW, Law RPH, et al (2015) Computational investigation of baffle configuration on impedance of channelized debris flow. Can Geotech J 52:182–197

[9] Chu T, Hill G, McClung DM, et al (1995) Experiments on granular flows to predict avalanche runup. Can Geotech J 32:285–295

[10] Cost ND (1979) Multiresource inventories: a technique for measuring volumes in standing trees. Southeastern Forest Experiment Station

[11] Costa JE (1984) Physical geomorphology of debris flows. In 'Developments and applications of geomorphology'.(Eds JE Costa, PJ Fleisher) pp. 268–317

[12] Cui P, Zeng C, Lei Y (2015) Experimental analysis on the impact force of viscous debris flow. Earth Surf Process Landforms 40:1644–1655

[13] D'Ippolito A, Calomino F, Alfonsi G, Lauria A (2021) Flow resistance in open channel due to vegetation at reach scale: A review. Water 13:116

[14] D'Ippolito A, Lauria A, Alfonsi G, Calomino F (2019) Investigation of flow resistance exerted by rigid emergent vegetation in open channel. Acta Geophys 67:971–986

[15] Mangeney, A., Roche, O., Hungr, O., Mangold, N., Faccanoni, G., & Lucas, A. (2010). Erosion and mobility in granular collapse over sloping beds. Journal of Geophysical Research: Earth Surface, 115(F3)

[16] Egli T (2005) Wegleitung Objektschutz gegen gravitative naturgefahren. VKF

[17] Etminan V, Lowe RJ, Ghisalberti M (2017) A new model for predicting the drag exerted by vegetation canopies. Water Resour Res 53:3179–3196

[18] Fidej G, Mikoš M, Rugani T, et al (2015) Assessment of the protective function of forests against debris flows in a gorge of the Slovenian Alps. iForest-Biogeosciences For 8:73

[19] Hübl J, Holzinger G (2003) Development of design basis for crest open structures for debris flow management in torrents: miniaturized tests for the efficiency estimation of debris flow breakers. WLS Rep 50

[20] Hübl J, Suda J, Proske D, et al (2009) Debris flow impact estimation. In: Proceedings of the 11th international symposium on water management and hydraulic engineering, Ohrid, Macedonia. pp 1–5

[21] Hungr O, Morgan GC, Kellerhals R (1984) Quantitative analysis of debris torrent hazards for design of remedial measures. Can Geotech J 21:663–677

[22] Iverson RM, George DL, Logan M (2016) Debris flow runup on vertical barriers and adverse slopes. J Geophys Res Earth Surf 121:2333–2357

[23] Iverson RM, Ouyang C (2015) Entrainment of bed material by Earth-surface mass flows: Review and reformulation of depth-integrated theory. Rev Geophys 53:27-58

[24] Julien PY, Leon C (2000) Mud floods, mudflows and debris flows. Classification, rheology and structural design. Jornadas Investig JIFI

[25] Kang T, Jang C-L, Kimura I, Lee N (2022) Numerical Simulation of Debris Flow and Driftwood with Entrainment of Sediment. Water 14:3673

[26] Kim B-J, Choi CE, Yune C-Y (2023) Multi-scale flume investigation of the influence of cylindrical baffles on the mobility of landslide debris. Eng Geol 314:107012

[27] Kim B-J, Yune C-Y (2022) Flume investigation of cylindrical baffles on landslide debris energy dissipation. Landslides 19:3043–3060

[28] Kim SJ, Stoesser T (2011) Closure modeling and direct simulation of vegetation drag in flow through emergent vegetation. Water Resour Res 47(10)

[29] Kothyari UC, Hayashi K, Hashimoto H (2009) Drag coefficient of unsubmerged rigid vegetation stems in open channel flows. J Hydraul Res 47:691–699

[30] Kumar r, Singh nk (2021) Three dimensional flow over elliptic cylinders arrays in octagonal arrangement. J Therm Eng 7:2031–2040

[31] Lei Y, Cui P, Zeng C, Guo Y (2018) An empirical mode decomposition-based signal process method for two-phase debris flow impact. Landslides 15:297–307

[32] Leonardi A, Pirulli M (2020) Analysis of the load exerted by debris flows on filter barriers: Comparison between numerical results and field measurements. Comput Geotech 118:103311

[33] Li R-M, Shen HW (1973) Effect of tall vegetations on flow and sediment. J Hydraul Div 99:793–814

[34] Lichtenhahn C (1973) Berechnung von sperren in beton und eisenbeton. Mitt Forstl Bundes Versuchsanst Wein

[35] Liu C, Nepf H (2016) Sediment deposition within and around a finite patch of model vegetation over a range of channel velocity. Water Resour Res 52:600–612

[36] Liu M-Y, Huai W-X, Yang Z-H, Zeng Y-H (2020) A genetic programming-based model for drag coefficient of emergent vegetation in open channel flows. Adv Water Resour 140:103582

[37] Liu W, Yang Z, He S (2021) Modeling the landslide-generated debris flow from formation to propagation and run-out by considering the effect of vegetation. Landslides 18:43–58

[38] Mahnamfar F, Abdollahzadehmoradi Y, Ağiralioğlu N (2020) Flood risk analysis of residential areas at downstream side of Elmali Dam. Acad Platf J Nat Hazards Disaster Manag 1:49–58

[39] Malvern LE (1969) Introduction to the Mechanics of a Continuous Medium

[40] Mancheño AG, Jansen W, Uijttewaal WSJ, et al (2021) Wave transmission and drag coefficients through dense cylinder arrays: Implications for designing structures for mangrove restoration. Ecol Eng 165:106231

[41] Mangeney, A., Roche, O., Hungr, O., Mangold, N., Faccanoni, G., & Lucas, A. (2010). Erosion and mobility in granular collapse over sloping beds. Journal of Geophysical Research: Earth Surface, 115(F3)

[42] Mashud M, Al-Bari A, Kader MG (2011) Experimental investigation of drag force reduction mechanism for flow around a circular cylinder. Int J Eng Appl Sci 3:69–75

[43] Nepf HM (2012) Hydrodynamics of vegetated channels. J Hydraul Res 50:262–279

[44] Nepf HM (1999) Drag, turbulence, and diffusion in flow through emergent vegetation. Water Resour Res 35:479–489

[45] Ng CWW, Choi CE, Song D, et al (2015) Physical modeling of baffles influence on landslide debris mobility. Landslides 12:1–18

[46] Riazi A, Türker U (2019) The drag coefficient and settling velocity of natural sediment particles. Comput Part Mech 6:427–437

[47] Scheidl C, Chiari M, Mullegger M, Proske D (2012) Estimation of debris-flow impact forces using a small scale modelling approach. In: 12th Congress Interpraevent

[48] Schoneboom T, Aberle J, Dittrich A (2011) Spatial variability, mean drag forces, and drag coefficients in an array of rigid cylinders. Exp methods Hydraul Res 255–265

[49] Scotton P, Deganutti AM (1997) Phreatic line and dynamic impact in laboratory debris flow experiments. In: Debris-flow hazards mitigation: mechanics, prediction, and assessment. ASCE, pp 777–786

[50] Sohrabi S, Afzalimehr H, Singh VP (2023) Estimation of drag coefficient of emergent and submerged vegetation patches with various densities and arrangements in open channel flow. ISH J Hydraul Eng 29:297–307

[51] Song D, Chen X, Zhou GGD, et al (2021) Impact dynamics of debris flow against rigid obstacle in laboratory experiments. Eng Geol 291:106211

[52] Stoesser T, Salvador GP, Rodi W, Diplas P (2009) Large eddy simulation of turbulent flow through submerged vegetation. Transp porous media 78:347–365

[53] Takahashi T (1979) Study of the deposition of debris flows (1)-deposition due to abrupt change of bed slope-. Ann Disaster Prev Res Inst Kyoto Univ 22:315–328

[54] Tanino Y, Nepf HM (2008) Laboratory investigation of mean drag in a random array of rigid, emergent cylinders. J Hydraul Eng 134:34–41

[55] Thouret J-C, Antoine S, Magill C, Ollier C (2020) Lahars and debris flows: Characteristics and impacts. Earth-Science Rev 201:103003

[56] Tiberghien D, Laigle D, Naaim M, et al (2007) Experimental investigations of interaction between mudflow and an obstacle. Debris-flow hazards Mitig Mech Predict assessment, Millpress, Rotterdam

[57] Valyrakis, M., Liu, D., Turker, U., & Yagci, O. (2021). The role of increasing riverbank vegetation density on flow dynamics across an asymmetrical channel. Environmental Fluid Mechanics, 21, 643-666

[58] Türker U, Valyrakis M (2021) Hydraulic jump on rough beds: conceptual modeling and experimental validation. Water Supply 21:1423–1437

[59] Türker U, Yagci O, Kabdasli MS (2019) Impact of nearshore vegetation on coastal dune erosion: assessment through laboratory experiments. Environ Earth Sci 78:1–14

[60] Türker U, Yagci O, Kabdaşlı MS (2006) Analysis of coastal damage of a beach profile under the protection of emergent vegetation. Ocean Eng 33:810–828

[61] Vargas-Luna A, Crosato A, Uijttewaal WSJ (2015) Effects of vegetation on flow and sediment transport: comparative analyses and validation of predicting models. Earth Surf Process Landforms 40:157–176

[62] Wang D, Li Q, Bi Y, He S (2020) Effects of new baffles system under the impact of rock avalanches. Eng Geol 264:105261

[63] Watanabe M (1981) Investigation and analysis of volcanic mud flows in mt sakurajima, japan

[64] Wilson C, Stoesser T, Bates PD, Pinzen AB (2003) Open channel flow through different forms of submerged flexible vegetation. J Hydraul Eng 129:847–853

[65] Yan Y, Tang H, Hu K, et al (2023) Deriving Debris-Flow Dynamics From Real-Time Impact-Force Measurements. J Geophys Res Earth Surf 128:e2022JF006715

[66] Yang E, Bui HH, Nguyen GD, et al (2021) Numerical investigation of the mechanism of granular flow impact on rigid control structures. Acta Geotech 16:2505–2527

[67] Yazid AS, Adnan TFFT, Abdullah AA, et al (2017) Flood risk mitigation: Pressing issues and challenges. Int Rev Manag Mark 7:157–163

[68] Zanchetta G, Sulpizio R, Pareschi MT, et al (2004) Characteristics of May 5–6, 1998 volcaniclastic debris flows in the Sarno area (Campania, southern Italy): relationships to structural damage and hazard zonation. J Volcanol Geotherm Res 133:377–393

[69] Zhang B, Huang Y, Liu J (2021) Micro-mechanism and efficiency of baffle structure in deceleration of granular flows. Acta Geotech 16:3667–3688

[70] Zhang S (1993) A comprehensive approach to the observation and prevention of debris flows in China. Nat Hazards 7:1–23

[71] Zhang S, Yuan J (1985) Impact force of debris flow and its detection. Mem Lanzhou Inst Glaciol Cryopedology, Chinese Acad Sci Beijing Sci Press 269–274

Turkish Journal of Civil Engineering, 2024, 47-64, Paper 787, ***Research Article***

Optimization of Hybrid Microwave Curing Approach Based On the Performance of Metakaolin-Based Geopolymer Mortars

Yiğit Alper ATALAY[1]
Tolga AYDIN[2]
Zeynep BAŞARAN BUNDUR[3*]
Pozhhan MOKHTARI[4]
Mehmet Ali GÜLGÜN[5]
Zoubeir LAFHAJ[6]

ABSTRACT

Geopolymer binders have been highlighted due to their low carbon emission during production and processing. While metakaolin and F-type fly ash are commonly used as raw materials for aluminosilicate-based geopolymers, the long heat-curing requirements for hardening and strength development still pose challenges. This paper investigates the possible use of a hybrid microwave curing technique to design a set-on-demand approach to reduce the duration of heat curing in metakaolin-based geopolymer. The experimental design was established for samples with three different molar ratios (MR; 1.3,1.5, and 1.7) containing metakaolin, fly ash, and silica fume. Samples were subjected to 3 different curing regimes: oven curing, microwave (MW) curing, and hybrid curing (a combination of optimized microwave and oven curing). The performance evaluation was based on compressive strength, dimensional stability, and alkali leaching (efflorescence). Implementing only MW curing resulted in a significant decrease in compressive strength

Note:
- This paper was received on October 12, 2023 and accepted for publication by the Editorial Board on June 14, 2024.
- Discussions on this paper will be accepted by January 31, 2025.
- https://doi.org/10.18400/tjce.1322047

1 Ozyegin University, Civil Engineering Department, Istanbul, Türkiye
alper.atalay@ozu.edu.tr - https://orcid.org/0000-0002-2296-1940

2 Ozyegin University, Civil Engineering Department, Istanbul, Türkiye
tolga.aydin@ozu.edu.tr - https://orcid.org/0009-0007-7699-7889

3 Ozyegin University, Civil Engineering Department, Istanbul, Türkiye
zeynep.basaran@ozyegin.edu.tr - https://orcid.org/0000-0003-1398-4021

4 University of Illinois, Material Science and Engineering, Urbana, USA
mokhtari@illinois.edu - https://orcid.org/0000-0002-0425-0483

5 Sabancı University, Faculty of Engineering and Natural Sciences, Istanbul, Türkiye
mehmet.gulgun@sabanciuniv.edu.tr - https://orcid.org/0000-0002-7096-6252

6 Civil Engineering Department, Centrale Lille, Lille, France
zoubeir.lafhaj@gmail.com - https://orcid.org/0000-0003-1985-9176

* Corresponding author

compared to their counterpart oven-cured samples. The reduction of compressive strength was more pronounced at lower molar ratios. The design of a hybrid curing approach where a portion of oven curing was replaced by MW resulted in a higher strength development than those only cured with MW. Similarly, the efficiency of hybrid curing was more pronounced in samples having MR of 1.5 and 1.7. Using MW curing in the geopolymer binders did not affect the alkali leaching; however, it increased the material's drying shrinkage. Results showed that replacing a portion of oven curing with microwave curing in a hybrid approach can increase the operation speed and the hardening rate without significantly decreasing compressive strength.

Keywords: Geopolymer, metakaolin, microwave curing, strength, shrinkage.

1. INTRODUCTION

Geopolymers are aluminosilicate-based sustainable building materials with a low carbon footprint during production and processing [1–3]. Some additional advantages of geopolymer binders over Ordinary Portland Cement (OPC) are higher compressive strengths, superior resistance to chemical attacks, freeze-thaw resistance, and higher temperature resistance [4–6]. Such properties have also led to geopolymers being considered as possible matrices for special applications such as hazardous/nuclear waste stabilization and solidification.

The raw materials for geopolymer binders can be provided entirely from aluminosilicate-rich by-products or naturally-resourced materials, such as calcined clays, with limited further processing [7–10]. Since the geopolymer composition generally involves by-product materials and natural resources, their production is efficient in raw material and energy consumption compared to OPC binders [2,11]. While geopolymer binders provide significant advantages in terms of sustainability, the cost of alkali activators such as sodium hydroxide (NaOH) and sodium silicate (Na_2SiO_2) limit their use to smaller volume operations [7].

It is known that a properly designed mix of high calcium-contained, alkali-activated binders can harden at room temperature, which makes them usable in the field. However, low-calcium geopolymer binders require additional time or heat, creating a disadvantage for *in-situ* applications. Without an external energy source such as heat, the polymerization reaction in low-calcium, i.e., metakaolin-based geopolymer, will be prolonged [12,13]. In general, heat and curing can be obtained in conventional ovens. Herein, the thermal energy is transferred from the surface to the core section of the material through convection, conduction, and heat radiation due to the different thermal gradients occurring in the material.

Despite certain advantages, the practical applications of geopolymers have been limited by the long maintenance time and slow strength development. Technologies that enable rapid strength development are of great interest in geopolymers. Recently, microwave curing (MW) was found to be an alternative heat curing method to improve the polymerization reaction rate [12,14–17]. In MW applications, microwaves can penetrate the matrix to generate heat throughout the volume of the material [14,18–20]. Microwave energy is delivered directly to the material through molecular interaction with the electromagnetic field. The electromagnetic energy is then converted to thermal energy. The curing process in a traditional oven causes water to evaporate from the surface of the treated materials quickly. Hence, uniform heating is difficult to achieve due to the high thermal gradient, resulting in

significant energy loss through heat conduction and convection in the heated materials [21]. MW provides an essential advantage in reducing the duration of heat curing, and it may even eliminate the need for heat curing if the binder system contains sufficient calcium oxide.

On the contrary, microwave heating induces the rise of temperature due to the absorption of heat by polar molecules to create position-independent localized heating spots, which is favorable for the formation of uniform volumetric heating. Besides, MW provides superior benefits to traditional heating, such as shortening the reaction time, improving reaction kinetics, lowering heat, enabling uniform heating, and higher energy efficiency [21–23]. While the material must be kept around 60 to 100 °C for an extended curing period in conventional oven curing, MW can provide a rapid temperature increase within seconds. However, improper microwave irradiation can cause surface cracking in geopolymers, reducing structural strength. Therefore, it is critical to understand the principles of microwave heating in developing geopolymer strength and how the process affects the key properties of geopolymers [24].

While MW can be applied to geopolymer ceramics, the application of such a method to building materials is still challenging because of the dimensions of the elements produced. Previously, Somaratna et al. [19] investigated the influence of MW on NaOH-activated, fly-ash-based mortars. It was found that MW applied for 120 min resulted in compressive strength comparable to those samples cured at 75 °C for 48 h. It was found that the compressive strength of the mortar samples was directly related to the total microwave energy absorbed during the first MW application when free water was present in the system [19]. However, applying MW for 120 min is still challenging for building materials. This study was followed using MW again for fly-ash-based geopolymers activated by Na_2SiO_2 and NaOH [12]. The study evaluated using MW and oven curing (OC) at higher temperatures in less than 60 minutes. The microwave-cured samples showed relatively higher compressive strength than those kept in the oven for 120 min [12]. The promising applicability of MW led the researchers to implement this technique in novel applications such as 3D printing. MW also effectively improved the buildability of slag-based alkali-activated material in 3D printing applications [25].

The MW method was validated in literature as an alternative curing method for alkali-activated material, mostly having slag as a primary precursor. This study investigated the effects of MW on strength and dimensional stability in metakaolin-based geopolymers. In addition, it was aimed at optimizing the duration of curing, enabling ease of application. The outcomes of this study can be applied to advance new processes, such as the 3D printing of geopolymers. The main goal of this study was to implement MW technology in metakaolin-based geopolymer mortars to reduce the duration of heat curing for geo-polymerization. The feasibility of MW was assessed in terms of compressive strength, dimensional stability, and alkali leaching. The significance of this research can be listed as (1) proposing a novel approach to trigger rapid hardening in metakaolin-based geopolymer with a short-term MW (less than 45 min); (2) establishing an optimized curing procedure; (3) reducing the total energy input in developing geopolymers and (4) investigating the effects of MW on alkali leaching and free shrinkage of the geopolymer binders.

2. MATERIALS AND EXPERIMENTAL METHODS

2.1. Materials

The primary raw materials used for the experiment were commercial metakaolin, silica fume, and F-type fly ash. Metakaolin was purchased from Kaolin Industrial Minerals Inc. Trade, Istanbul, Turkey. The fly ash was obtained from Cates Electric (Zonguldak, Turkey), and the commercial silica fume was purchased from Dost Kimya Inc. Trade, Istanbul, Turkey. Table 1 lists the chemical compositions of the raw materials used in the mixes. The data for metakaolin and fly ash was obtained by quantitative X-ray diffraction (XRD) analysis conducted with a BRUKER D8 Advance X-ray diffractometer (Karlsruhe, Germany). The XRD analysis of the minerals was conducted at angles from 10 to 90° 2θ at a step size of 0.02° in 2θ.

Table 1 - Composition of metakaolin, Type F fly ash, and silica fume

Element	Weight %		
	Metakaolin	**Fly Ash**	**Silica Fume**
SiO_2	56.1	55.8	98.1 (Amorph)
Al_2O_3	40.2	26.0	-
Fe_2O_3	0.8	6.44	-
CaO	0.2	1.68	-
MgO	0.2	2.33	-
SO_3	-	0.18	-
Na_2O	-	1.87	-
K_2O	0.5	3.86	-
Na Eq.	0.24	4.41	-
Free CaO	N/S	0.08	-
LOI	1.5	2.61	1.81

The manufacturer provided the chemical composition of silica fume. The average particle sizes of the raw materials were determined by a Mastersizer 2000 particle size analyzer with a Hydro MU 2000 (Malvern, Worcestershire, United Kingdom) wet dispersion unit. Figure 1 summarizes the particle size distributions for metakaolin and fly ash. The average particle size of silica fume was less than 25 μm. Amongst all materials used, silica fume had the smallest particle size, whereas metakaolin and fly ash had relatively similar gradation curves.

The alkaline activating solution was formulated using a commercially available sodium silicate solution composed of 26.5 wt% SiO_2, 10.6 wt% Na_2O, and 62.9 wt% H_2O having a molar ratio (MR, $nSiO_2/nNa_2O$) of 2.6. The sodium silicate solution was then mixed with 8 M sodium hydroxide (NaOH) solution to obtain the desired molar ratios (MR) of the

activating solution. Table 2 summarizes the relative proportions of the mixed ingredients. At last, mortar samples were prepared using standard sand according to the norm EN 196-1.

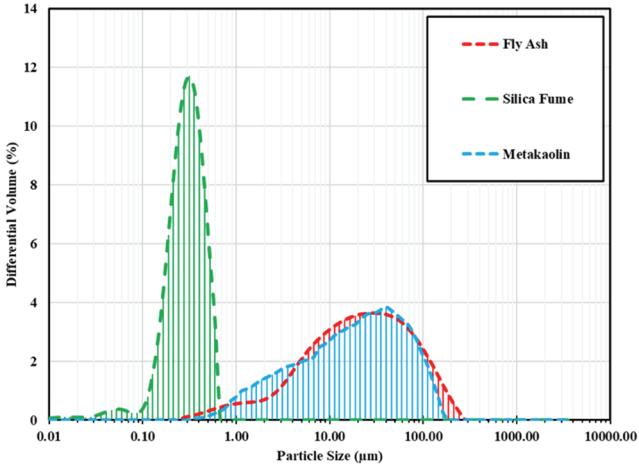

Figure 1 - Particle size distribution of Metakaolin and Fly Ash

Table 2 - Material proportions of blended geopolymers. FA: Fly Ash; MK: Metakaolin; SF: Silica Fume; MR: Molar Ratio; sol/b: Solution to binder ratio; w/b: Water to binder ratio

Sample Name	Binder (g)			Activating Solution (mL)		MR	sol/b	w/b	SiO_2/Al_2O_3	SiO_2/Na_2O
	FA	MK	SF	NaOH (8M)	Na_2SiO_3					
MK_5_1.3	180	390	30	105	255	1.3	0.62	0.4	3.31	7.01
MK_10_1.3	180	360	60	105	255	1.3	0.62	0.4	3.62	7.21
MK_15_1.3	180	330	90	105	255	1.3	0.62	0.4	3.98	7.42
MK_5_1.5	180	390	30	92	280	1.5	0.62	0.4	3.36	7.18
MK_10_1.5	180	360	60	92	280	1.5	0.62	0.4	3.68	7.39
MK_15_1.5	180	330	90	92	280	1.5	0.62	0.4	4.04	7.60
MK_5_1.7	180	390	30	70	300	1.7	0.62	0.4	3.40	7.69
MK_10_1.7	180	360	60	70	300	1.7	0.62	0.4	3.72	7.91
MK_15_1.7	180	330	90	70	300	1.7	0.62	0.4	4.09	8.13

2.2. Sample Preparation and Methodology

Nine mix compositions containing metakaolin, fly ash, and silica fume were prepared within the scope of this study. The weight % of the fly ash was kept at 30 wt% of the total binder content. A portion of the metakaolin in the binder was replaced by silica fume (5,10, and 15 wt. %). The formulated mixtures were designed to initiate hardening by providing the required heat of curing due to their low calcium oxide (CaO) contents (< 5% by weight) [26,27]. The activator solution to binder ratio (sol/b), including the water content in the activating solution, was kept at 0.60 ± 0.02, and the water to binder ratio (w/b) was held at 0.40. Mortar samples were prepared according to ASTM C305-14 [28]. Since the designed material system was aimed at 3D printing applications, the binder-to-sand ratio was kept at 1:1.5 [29].

The samples were cast in 40 x 40 x 160 mm molds. For all samples, three different curing regimes were applied: The duration and power of the microwave were determined by preliminary evaluations of its effects on hardening and workability. The microwave curing power and time were selected considering their impact on the geopolymers. Samples were kept in a humid environment under ambient conditions (70% RH at 23 ˚C).

2.3. Mechanical Performance Tests

The mechanical performance of the geopolymer mortars was determined by compressive strength tests. The mechanical performance was measured 3, 7, and 28 days after casting. The compressive strength was measured according to standard EN 196-1 [30]. The performance tests were done on triplicate samples.

2.4. Drying Shrinkage in Geopolymer Mortars

The dimensional stability and resistance against drying shrinkage in geopolymer mortars were assessed according to the ASTM C596-18 standard [31]. Geopolymer samples were cast in 50 x 50 x 285 mm molds. Six samples were cast from each mix. A set of samples were directly put in the oven for curing. Another set was subjected to hybrid curing. The samples were kept in a humid environment for three days after heat curing, as stated in section 2.2. After three days, the samples were removed from the curing chamber and submerged in the lime water for 24 hours, as stated in the standard. Then, the samples were removed from lime water, and the length and weight measurements were taken as t=0 [31]. The samples were kept in a 50% RH environment at 23 ˚C for 16 weeks. Periodic length measurements were taken at the 4^{th}, 7^{th}, 11^{th}, $18^{th,}$ 25^{th} days, and 8^{th} and 16^{th} weeks. Each measurement was taken from triplicates of samples.

2.5. Alkali Leaching in Geopolymer Mortars

The occurrence of alkali leaching (i.e., efflorescence) in geopolymer mortar was determined by 40x40x160 mm samples. A set of samples were directly put in an oven for curing. Another group was subjected to hybrid curing. The samples were kept in a humid environment for 28 days after heat curing. Then, the samples were placed in distilled water and kept in an open-air atmosphere at ambient conditions (60 ± 5 % RH at 23 ˚C) until the water evaporated completely. The initial evaluation was done by visual inspection. Once all the water was evaporated, the leached product produced on the top and bottom surfaces of the samples was scratched, and the material was collected from the sample. The weight of the total leached material was recorded for each sample. A qualitative XRD X-ray diffraction (XRD) analysis was done for the leached products with a BRUKER D8 Advance X-ray Diffractometer (Karlsruhe, Germany). The samples were placed and compacted into a sample holder, and analysis was conducted at angles from 10 to 90° 2θ at a step size of 0.02° 2θ.

3. RESULTS AND DISCUSSION

3.1. Compressive Strength

The initial evaluation of MW curing was done regarding compressive strength tests. Figure 2 compares the compressive strength of metakaolin-based geopolymers at different MRs and cured under various conditions. The MR and degree of heat input highly influenced the compressive strength of the metakaolin-based geopolymer systems.

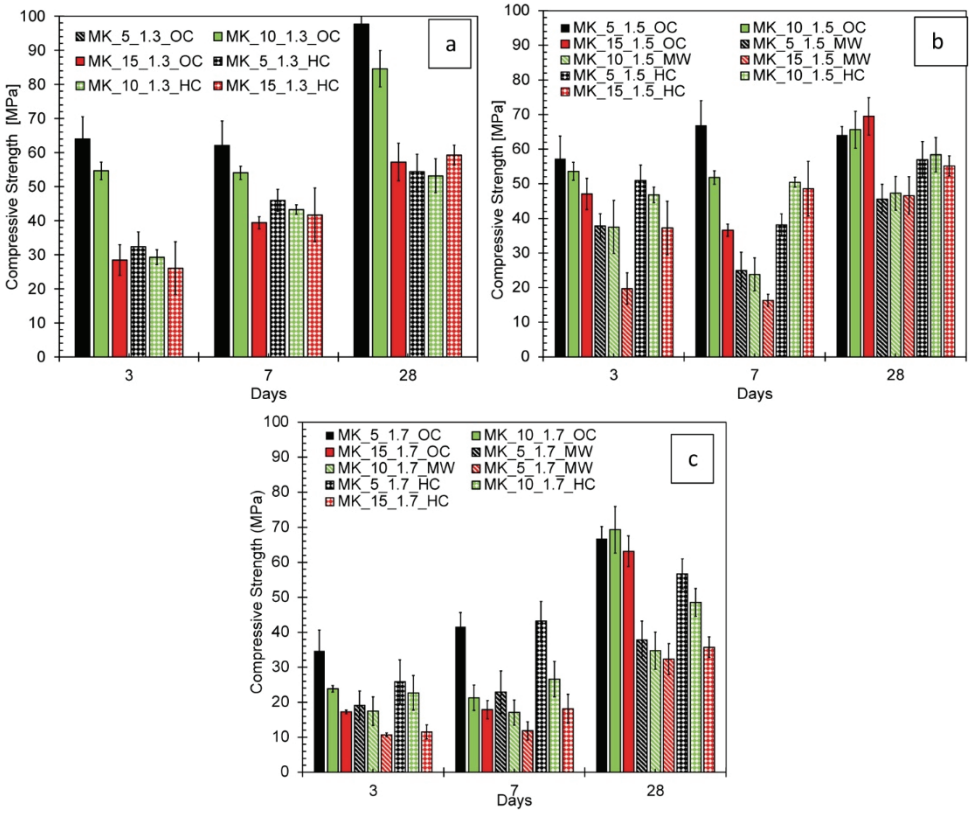

Figure 2 - Compressive strength of geopolymer mortars (a) MR: 1.3 (b) MR:1.5 (c) MR:1.7. OC: Oven Curing; MW: Microwave Curing; HC: Hybrid Curing. *The samples were not hardened with only microwave curing*

While MR is an important factor in compressive strength, the highest strength values were recorded with oven curing regardless of all MR ratios; this indicates that both MR and curing methodology are decisive factors. Even with oven curing, increasing silica fume dosage was more pronounced at 28 days and decreased the compressive strength at 3 and 7 days. This can be attributed to the pozzolanic nature of silica fume [32]. In addition, achieving a strength increase at 28 days in the MK_15 sample (15% silica fume) required an MR of 1.5 or higher.

This shows that the system should have higher moles of Na_2O to form N-A-S-H in a silica-rich environment.

Only MW curing reduced the compressive strength compared to the oven-cured counterpart samples. Theoretically, MW curing at 800W for 3 minutes should trigger a faster geopolymerization process by increasing the reaction rate [15, 25]. The samples with an MR of 1.5 and 1.7 were hardened after microwave application. This indicated that microwave curing was adequate for accelerating the strength gain of metakaolin-based geopolymer. However, this accelerating effect did not directly lead to increased 3-day compressive strength. Another important point is that MW curing was insufficient to develop strength in the MR_1.3_MW series. The sample with an MR of 1.3 was hardened but did not exhibit any strength. The compressive strength in MR_1.3_MW samples was recorded as "0". This might be due to the extended duration of high-energy microwave heating that can trigger evaporation in pore water, leading to a lower water content before the geopolymerization reaction. This effect results in a denser microstructure and an increasing rate of the hardening process without increasing the strength. A further evaluation must be done to understand the influence of microwave curing on the chemical composition of the geopolymer and establish a methodology to reduce the water loss in the samples.

Further optimization was done by establishing a combined hybrid curing (HC) approach. Herein, the samples were subjected to MW curing for 90 seconds and then kept at 60^{o}C for 30 minutes. This method partially restored the decrease in compressive strength due to only MW curing, particularly for an MR of 1.5. However, HC samples' compressive strength was still lower than their oven-cured counterparts, particularly for samples cured at 3 and 7 days. At 28 days, the decrease in compressive strength for HC compared to OC was 15% for MR 1.5, regardless of the percentage of silica fume replaced. This might have shown that the rapid heat application increased the hardening rate, but the total heat energy applied might not have been sufficient to trigger rapid geoopolymerization. Yet, based on the results obtained, it is concluded that the effective performance features are silica fume replacement, MR, and compressive strength. The silica fume replacement should be kept at 5% if we use an MR of 1.3, whereas increasing the silica fume dosage resulted in higher strength development in oven-cured samples. This trend was different when MW or HC was applied to the material; in this case, increasing MR and silica fume dosage decreased compressive strength. Therefore, further evaluation was done to correlate the curing regime, SiO_2/Al_2O_3, and SiO_2/Na_2O ratios on compressive strength

To correlate the chemical composition to the mechanical properties, further evaluation was done by assessing the influence of SiO_2/Al_2O_3 and SiO_2/Na_2O ratios on compressive strength. Figure 3 summarizes the effect of SiO_2/Al_2O_3 and SiO_2/Na_2O ratios on the compressive strength of geopolymer mortar cured at different temperatures. It was found that there was a direct relationship between the SiO_2/Na_2O ratio and the early age (3 and 7 days) compressive strength of the mortar. Both 3 and 7-day compressive strength of mortar decreased with increasing SiO_2/Na_2O ratio. The reduction in strength could be attributed to the excess silica content that could interfere with the geopolymerization process.

Even though the evaluations indicated that the decrease in compressive strength was more pronounced depending on the SiO_2/Na_2O ratio rather than the SiO_2/Al_2O_3 ratio, a high SiO_2/Al_2O_3 ratio might also adversely affect compressive strength. Wan et al. [33] evaluated the impact of extended SiO_2/Al_2O_3 concentrations on the mechanical properties of

metakaolin-based geopolymers. The results concluded that the optimum SiO_2/Al_2O_3 ratio should be held at 2, and increasing the SiO_2/Al_2O_3 ratio to 3 would significantly decrease the compressive strength. Higher concentrations of Si^{+4} and Al^{+3} could immediately form a gel around the metakaolin particles and prevent their subsequent destruction [34]. This study

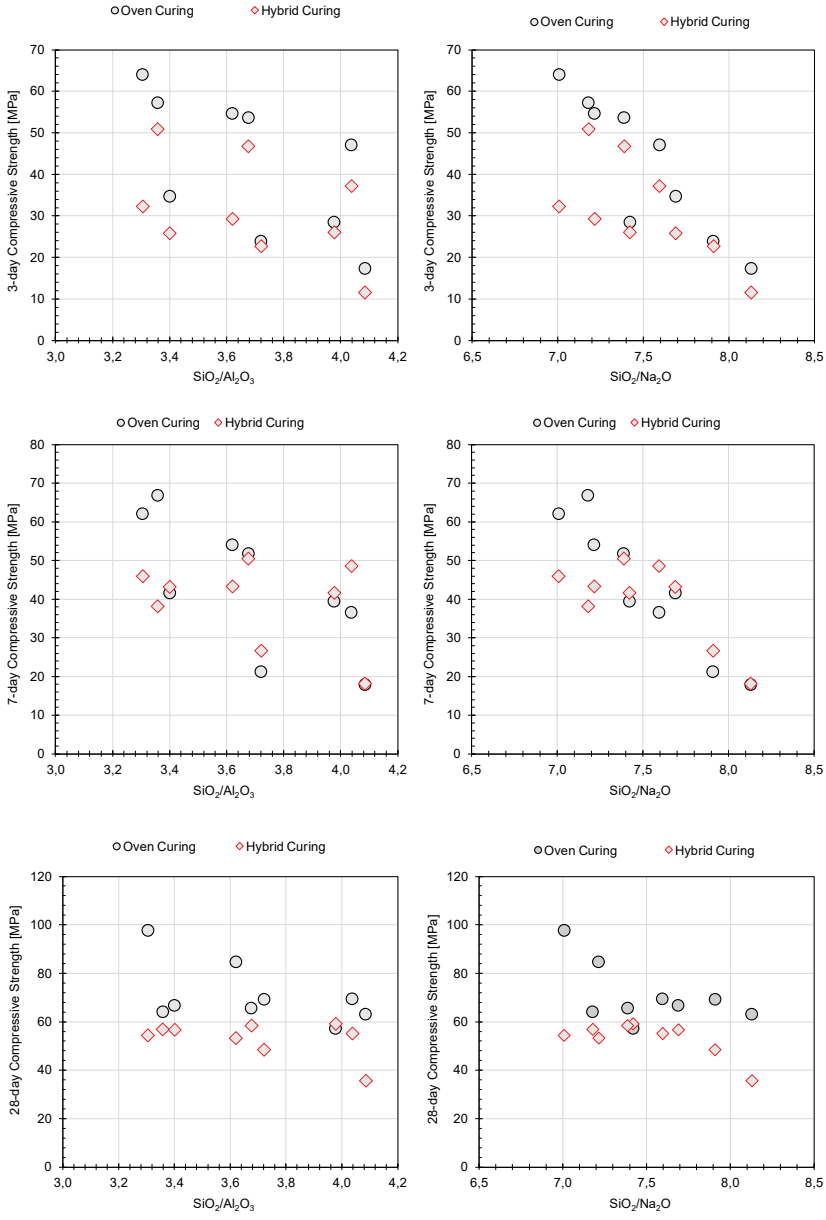

Figure 3 - Relationships between compressive strength and alkali content (a,b) 3 days (c,d) 7 days (e,f) 28 days

held the SiO_2/Al_2O_3 ratio between 3 and 4. Therefore, it was not possible to observe a significant change in the properties due to an increase in SiO_2/Al_2O_3 ratio. However, a lower SiO_2/Al_2O_3 ratio might have led to different outcomes regarding the absolute compressive strength and the effectiveness of the microwave application.

3.2. Dimensional Stability and Drying Shrinkage

Like the OPC binders, geopolymer systems also have a low tensile strength that can result in cracking due to excessive tensile stress developed due to early-age plastic shrinkage strains. Some geopolymer binders may have a higher drying shrinkage than OPC binders since the water does not form the aluminosilicate gel [35]. Higher drying shrinkage means a higher risk of cracking, leading to serviceability or durability problems. Although metakaolin-based geopolymers exhibit superior resistance to thermal shrinkage at temperatures above 700°C compared to OPC binders, they might be susceptible to severe shrinkage cracking at ambient temperatures [36].

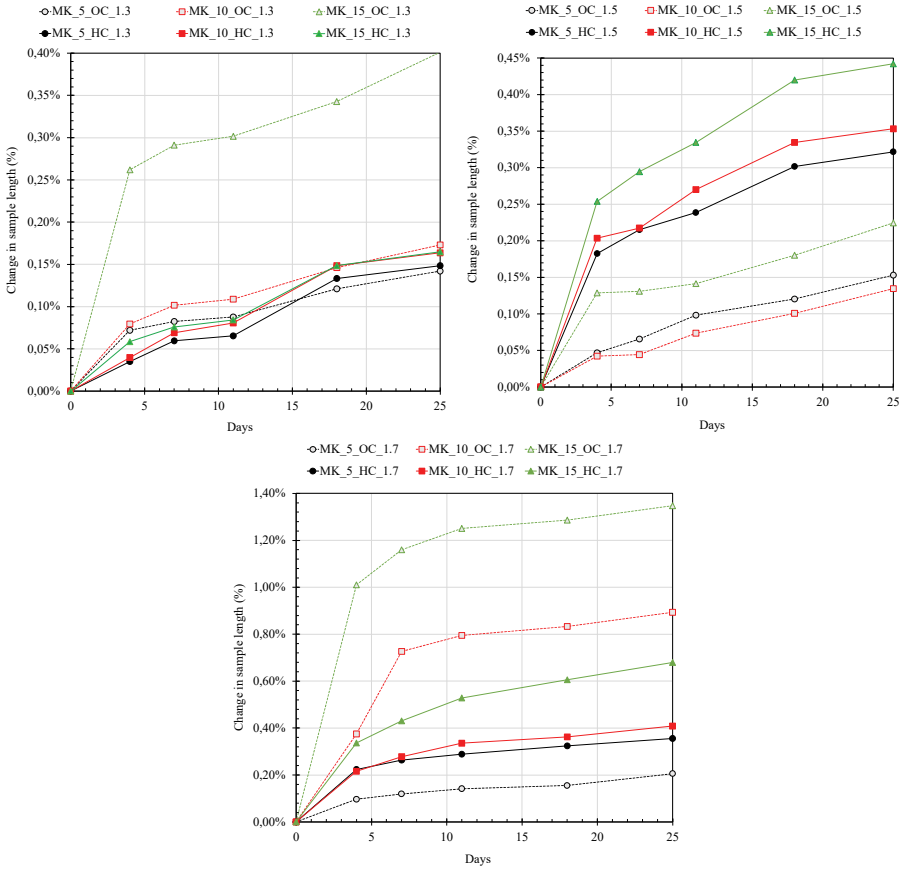

Figure 4 - Time-dependent length change in geopolymer mortars (a) MR: 1.3 (b) MR:1.5 (c) MR:1.7. MK: Metakaolin; OC: Oven Curing; HC: Hybrid Curing

Figure 4 summarizes the percent length changes in metakaolin-based geopolymer mortars cured in OC and HC. Based on the results, increasing the MR resulted in a higher degree of length change. In addition, the heat-cured samples (OC) showed relatively smaller length changes than their microwave-cured counterpart samples (HC). Previous studies indicated that the drying shrinkage of fly ash-based geopolymer concrete mixes cured under ambient conditions could be significantly higher than in OPC-based binders within the range of 1500 µcontrast. The drying shrinkage of heat-cured specimens was recorded in the range of 100 µscript epsilon [37,38]. Volumetric changes in metakaolin-based geopolymers were attributed to drying shrinkage rather than autogenous shrinkage [39]. Like the samples cured under ambient conditions, HC might result in a lower degree of geopolymerization, leaving the mortar mixed with a higher water content even after hardening. The remaining water content may result in a higher degree of evaporation and increase the drying of the material in a hardened state.

3.3. Alkali Leaching

Another performance parameter investigated in this study was alkali leaching (a.k.a efflorescence) in metakaolin-based geopolymers. While alkali leaching in OPC binders occurs with the reaction of soluble Ca^{+2} and CO_2 to form carbonate deposits, geopolymer binders could be much more complicated due to their relatively higher soluble alkali concentrations than OPC [9]. Therefore, alkali leaching could be a more severe issue in geopolymer binders. The known parameters affecting the extent of efflorescence in geopolymer binders can be listed as the reactivity of raw materials, type of alkali, and reaction conditions [40,41]. The alkali leaching in distilled water for the designed metakaolin geopolymers was quantitively assessed by calculating the total weight of collected leached precipitates. Table 3 summarizes the total amount of leached precipitates collected from mortar beams. The results showed that the amount of leaching was directly related to the MR of the alkali-activating solution. Increasing the silica fume content from 5 to 10% decreased the total amount of leached precipitates.

Table 3 - Total alkali leaching content in geopolymer mortars (kg) MK: Metakaolin; OC: Oven Curing; HC: Hybrid Curing

Sample Name	Oven Curing	Hybrid Curing
MK_5_1.3	2.55 ± 0.21	5.39 ± 0.18
MK_10_1.3	1.47 ± 0.19	1.13 ± 0.25
MK_15_1.3	1.39 ± 0.21	2.29 ± 0.21
MK_5_1.5	3.86 ± 0.28	3.82 ± 0.87
MK_10_1.5	1.76 ± 0.17	1.66 ± 0.16
MK_15_1.5	1.57 ± 0.14	2.66 ± 0.08
MK_5_1.7	8.21 ± 0.41	10.38 ± 0.19
MK_10_1.7	5.08 ± 0.59	6.70 ± 0.03
MK_15_1.5	11.78 ± 0.40	6.54 ± 0.22

In geopolymer binders such as those having metakaolin or fly ash as a precursor, the molar ratio SiO_2/Al_2O_3 is an essential indicator of the reactivity in the binder and microstructural features of the gel formed. Figure 5 presents the relationship between the SiO_2/Na_2O and SiO_2/Al_2O_3 ratios on the total alkali leaching. Our results showed that increasing the SiO_2/Na_2O ratio increased leaching. However, the relationship between alkali leaching and SiO_2/Al_2O_3 was more complex since there was no consistent trend between the total alkali leaching and SiO_2/Al_2O_3 ratio. A previous study found that the systems with a lower SiO_2/Al_2O_3 ratio, in other words, higher concentrations of Al_2O_3, will promote a higher degree of dissolution, which might decrease the ion binding capacity of the gel and lead to a higher degree of leaching [42, 43]. Our results indicated that the influence of the SiO_2/Al_2O_3 ratio was more pronounced in samples having a higher MR (i.e., MR=1.7). This effect on leaching can be correlated with the amount of drying shrinkage in samples. The samples with a higher alkali leaching also demonstrated a higher degree of plastic shrinkage. The loss of reaction phases in the material resulted in a change in volumetric dimension.

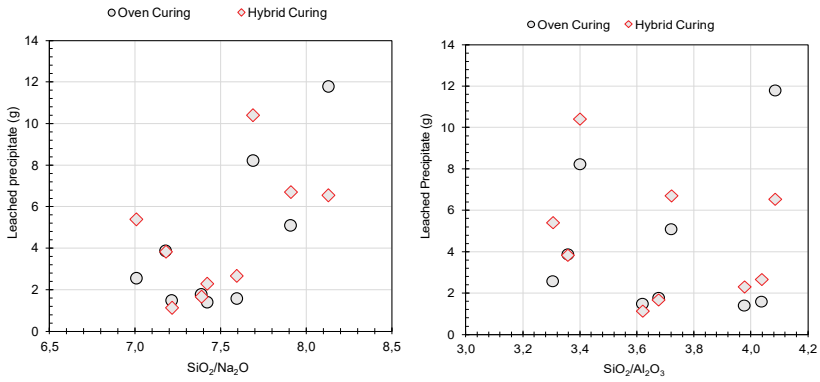

Figure 5 - Relationship between total alkali leaching from the sample and the alkali content in the mix (a) SiO_2/Na_2O and (b) SiO_2/Al_2O_3

Another critical factor affecting alkali leaching could be the temperature applied during the curing process. It was found that microwave curing did not significantly affect the total amount of leaching. In geopolymer binders, heat curing promotes the reaction and dissolution of oxides in the precursor, resulting in a faster geo-polymerization reaction [44]. Kani et al. [45] observed that alkali leaching could be reduced when the curing temperature was increased above 65°C. Heat curing can increase the gel formed with a higher density and a higher amount of captured Na^+.

Finally, an evaluation was done to characterize the chemical composition of the leached precipitate, and Figure 6 presents the XRD diffractograms for geopolymer binders. The leached precipitate was mainly a mix of sodium carbonate (Na_2CO_3) and quartz (SiO_2), which shows that the leaching was due to effloresce. This indicates that the main binding phase Na-A-S-H in the geopolymer is converted to carbonate Na_2CO_3 through carbonation. Thus, the dimensional change observed in Section 3.2 can also be related to carbonation-induced and plastic shrinkage. This may also cause a decrease in compressive strength since the main binder phase is carbonated and tends to leach from the sample.

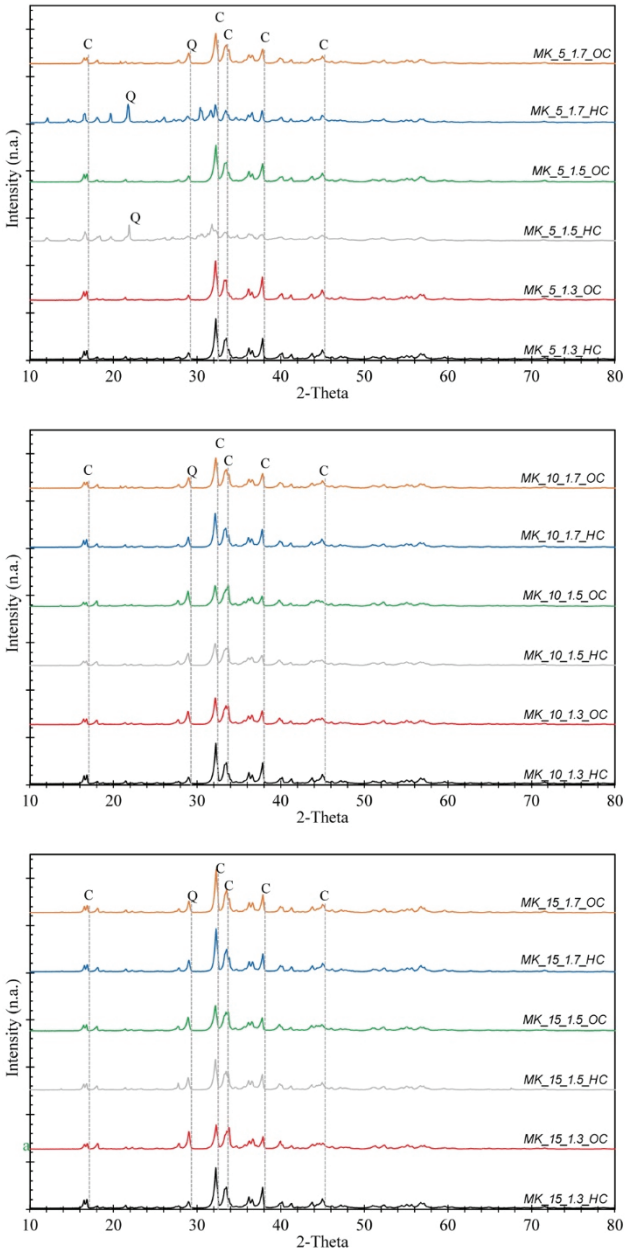

Figure 6 - X-ray diffractograms from leached contents obtained from geopolymer containing 5% silica fume by weight of cement (a) 5% silica fume replacement (b) 10% silica fume replacement (c) 15% silica fume replacement MK: metakaolin; OC: oven curing; HC: hybrid curing. C: sodium carbonate (PDF:70-8045): Q: quartz (PDF 82-0512).

4. CONCLUSION

This study aimed to develop a microwave curing technique to design a set-on-demand approach to improve the hardening rate in metakaolin-based geopolymer in a shorter time frame. The outcomes of the experimental evaluations indicated that only microwave curing reduced the compressive strength of metakaolin-based geopolymers. The curing scheme has been optimized to adapt heat and microwave curing to a hybrid system. Throughout the literature, the MW curing approach was only proposed for slag-based geopolymers, which can already react at room temperature. Herein, the challenge is to adapt this technology to low calcium oxide binders where heat curing is required. Hybrid curing (HC) resulted in a 75% decrease in curing time in metakaolin-based geopolymers. Even though this decrease seems insignificant in lab-scale cast specimens, HC will provide an important advantage in special applications such as 3D printing or precast elements.

- Only MW curing resulted in a significant decrease in compressive strength compared to the counterpart oven-cured samples. The reduction of compressive strength was more pronounced at lower molar ratios (MR: 1.3). This was attributed to the sudden evaporation of the water phase, limiting the further geo-polymerization reaction.
- The design of a hybrid curing approach where a portion of oven curing was replaced by MW resulted in a higher strength development than those only cured with MW. Similarly, the efficiency of hybrid curing was more pronounced in samples having MR of 1.5 and 1.7. The 28-day compressive strength of hybrid cured geopolymer mortars was 90% and 75% of the oven-cured counterpart samples for MRs 1.5 and 1.7, respectively.
- The results indicated a direct relationship between the SiO_2/Na_2O ratio and the early-age compressive strength of geopolymer mortar. The strength reduction was attributed to excess silica content that can interfere with geopolymerization.
- Implementing the hybrid curing approach increased the drying shrinkage of the geopolymer mortar, but it did not affect the alkali leaching in the material. The increased drying shrinkage was attributed to water loss because of the applied rapid microwave energy.
- The alkali leaching was found to be directly affected by the molar ratio of the alkaline solution, increasing the molar ratio and SiO2/Al2O3 ratio, thereby reducing the system's ion binding capacity.
- This optimization of hybrid curing decreased the duration of the required heat treatment of the mortar, leading to an advantage in special field applications such as 3D printing.

Acknowledgment

This research was conducted with financial assistance from the Scientific and Technical Research Council (TUBITAK) of Turkey (Project No: MAG-119N246) and Campus France (Project No: 44804RM).

Author Contributions

YAA and TA: conceptualizing the work, experimental analysis, data curation and analysis, methodology, drafting the plots and tables, and writing the original draft. PM: Developing the microwave concept, XRD data curation, and analysis. MAG: Developing the microwave concept and reviewing the original draft. WK, DK, and ZL: data analysis, review, and editing. ZBB: conceptualizing the work, funding acquisition, project management, administration, methodology, supervision, resources, and writing-review and editing. All authors contributed to the article and approved the submitted version.

Conflict of Interest

The authors declare no conflict of interest.

References

[1] K. Chen, Q. Liu, B. Chen, S. Zhang, L. Ferrara, W. Li, Effect of raw materials on the performance of 3D printing geopolymer: A review, Journal of Building Engineering 84 (2024) 108501. https://doi.org/10.1016/j.jobe.2024.108501.

[2] Y.H.M. Amran, R. Alyousef, H. Alabduljabbar, M. El-Zeadani, Clean production and properties of geopolymer concrete; A review, J Clean Prod 251 (2020) 119679. https://doi.org/10.1016/j.jclepro.2019.119679.

[3] N. Akhtar, T. Ahmad, D. Husain, A. Majdi, M.T. Alam, N. Husain, A.K.S. Wayal, Ecological footprint and economic assessment of conventional and geopolymer concrete for sustainable construction, J Clean Prod 380 (2022) 134910. https://doi.org/10.1016/j.jclepro.2022.134910.

[4] B. Zhang, Durability of low-carbon geopolymer concrete: A critical review, Sustainable Materials and Technologies 40 (2024) e00882. https://doi.org/10.1016/j.susmat.2024.e00882.

[5] P. Zhang, X. Han, S. Hu, J. Wang, T. Wang, High-temperature behavior of polyvinyl alcohol fiber-reinforced metakaolin/fly ash-based geopolymer mortar, Compos B Eng 244 (2022) 110171. https://doi.org/10.1016/j.compositesb.2022.110171.

[6] W. Tu, M. Zhang, Behaviour of alkali-activated concrete at elevated temperatures: A critical review, Cem Concr Compos 138 (2023) 104961. https://doi.org/10.1016/j.cemconcomp.2023.104961.

[7] M.C.G. Juenger, F. Winnefeld, J.L. Provis, J.H. Ideker, Advances in alternative cementitious binders, Cem Concr Res 41 (2011) 1232–1243. https://doi.org/10.1016/j.cemconres.2010.11.012.

[8] K. Sankar, A. Sutrisno, W.M. Kriven, Slag-fly ash and slag-metakaolin binders: Part II—Properties of precursors and NMR study of poorly ordered phases, Journal of the American Ceramic Society 102 (2019) 3204–3227. https://doi.org/10.1111/jace.16224.

[9] K. Sankar, P. Stynoski, G.K. Al-Chaar, W.M. Kriven, Sodium silicate activated slag-fly ash binders: Part I – Processing, microstructure, and mechanical properties, Journal of the American Ceramic Society 101 (2018) 2228–2244. https://doi.org/10.1111/jace.15391.

[10] K. Sankar, P. Stynoski, W.M. Kriven, Sodium silicate activated slag-fly ash binders: Part III—Composition of soft gel and calorimetry, Journal of the American Ceramic Society 102 (2019) 3175–3190. https://doi.org/10.1111/jace.16219.

[11] R. Bajpai, K. Choudhary, A. Srivastava, K.S. Sangwan, M. Singh, Environmental impact assessment of fly ash and silica fume based geopolymer concrete, J Clean Prod 254 (2020) 120147. https://doi.org/10.1016/j.jclepro.2020.120147.

[12] A. Graytee, J.G. Sanjayan, A. Nazari, Development of a high strength fly ash-based geopolymer in short time by using microwave curing, Ceram Int 44 (2018) 8216–8222. https://doi.org/10.1016/j.ceramint.2018.02.001.

[13] F. Puertas, S. Martínez-Ramírez, S. Alonso, T. Vázquez, Alkali-activated fly ash/slag cements, Cem Concr Res 30 (2000) 1625–1632. https://doi.org/10.1016/S0008-8846(00)00298-2.

[14] P. Chindaprasirt, U. Rattanasak, S. Taebuanhuad, Role of microwave radiation in curing the fly ash geopolymer, Advanced Powder Technology 24 (2013) 703–707. https://doi.org/10.1016/j.apt.2012.12.005.

[15] R. Prommas, T. Rungsakthaweekul, Effect of Microwave Curing Conditions on High Strength Concrete Properties, Energy Procedia 56 (2014) 26–34. https://doi.org/10.1016/j.egypro.2014.07.128.

[16] M. Nadeem, E. Ul Haq, F. Ahmed, M. Asif Rafiq, G. Hameed Awan, M. Zain-ul-Abdein, Effect of microwave curing on the construction properties of natural soil based geopolymer foam, Constr Build Mater 230 (2020). https://doi.org/10.1016/j.conbuildmat.2019.117074.

[17] J. Tan, J. Cai, L. Huang, Q. Yang, M. Mao, J. Li, Feasibility of using microwave curing to enhance the compressive strength of mixed recycled aggregate powder based geopolymer, Constr Build Mater 262 (2020). https://doi.org/10.1016/j.conbuildmat.2020.120897.

[18] E.T. Thostenson, T.W. Chou, Microwave processing: fundamentals and applications, Compos. Part A: Appl. Sci. Manuf. 30 (1999) 1055–1070.

[19] J. Somaratna, D. Ravikumar, N. Neithalath, Response of alkali activated fly ash mortars to microwave curing, Cem Concr Res 40 (2010) 1688–1696. https://doi.org/10.1016/j.cemconres.2010.08.010.

[20] S. Das, A.K. Mukhopadhyay, S. Datta, D. Basu, Prospects of microwave processing: An overview, 2009.

[21] Y. Sun, P. Zhang, J. Hu, B. Liu, J. Yang, S. Liang, K. Xiao, H. Hou, A review on microwave irradiation to the properties of geopolymers: Mechanisms and challenges, Constr Build Mater 294 (2021) 123491. https://doi.org/10.1016/j.conbuildmat.2021.123491.

[22] Z. Dong, H. Ma, W. Feng, Y. Nie, H. Shi, Achieving superior high-strength geopolymer via the synergistic effect of traditional oven curing and microwave curing, Constr Build Mater 357 (2022) 129406. https://doi.org/10.1016/j.conbuildmat.2022.129406.

[23] A.A. Shubbar, M. Sadique, P. Kot, W. Atherton, Future of clay-based construction materials – A review, Constr Build Mater 210 (2019) 172–187. https://doi.org/10.1016/j.conbuildmat.2019.03.206.

[24] E.T. Thostenson, T.-W. Chou, Microwave processing: fundamentals and applications, Compos Part A Appl Sci Manuf 30 (1999) 1055–1071. https://doi.org/10.1016/S1359-835X(99)00020-2.

[25] S. Muthukrishnan, S. Ramakrishnan, J. Sanjayan, Effect of microwave heating on interlayer bonding and buildability of geopolymer 3D concrete printing, Constr Build Mater 265 (2020) 120786. https://doi.org/10.1016/j.conbuildmat.2020.120786.

[26] A. Noushini, A. Castel, The effect of heat-curing on transport properties of low-calcium fly ash-based geopolymer concrete, Constr Build Mater 112 (2016) 464–477. https://doi.org/10.1016/j.conbuildmat.2016.02.210.

[27] A. Noushini, F. Aslani, A. Castel, R.I. Gilbert, B. Uy, S. Foster, Compressive stress-strain model for low-calcium fly ash-based geopolymer and heat-cured Portland cement concrete, Cem Concr Compos 73 (2016) 136–146. https://doi.org/10.1016/j.cemconcomp.2016.07.004.

[28] ASTM International, ASTM C305-14 Standard Practice for Mechanical Mixing of Hydraulic Cement Pastes andMortars of Plastic Consistency, West Conshohocken, 2014. https://doi.org/10.1520/C0305-14.2.

[29] B. Panda, C. Unluer, M.J. Tan, Investigation of the rheology and strength of geopolymer mixtures for extrusion-based 3D printing, Cem Concr Compos 94 (2018) 307–314. https://doi.org/10.1016/j.cemconcomp.2018.10.002.

[30] European Standarts, EN 196-1: Methods of testing cement - Part 1: Determination of strength, 2016.

[31] ASTM, ASTM C 596-18 Standard Test Method for Drying Shrinkage of Mortar Containing Hydraulic Cement, West Conshohocken, PA, USA, 2018.

[32] B. Li, A. Gao, Y. Li, H. Xiao, N. Chen, D. Xia, S. Wang, C. Li, Effect of silica fume content on the mechanical strengths, compressive stress–strain behavior and microstructures of geopolymeric recycled aggregate concrete, Constr Build Mater 384 (2023) 131417. https://doi.org/10.1016/j.conbuildmat.2023.131417.

[33] Q. Wan, F. Rao, S. Song, R.E. García, R.M. Estrella, C.L. Patiño, Y. Zhang, Geopolymerization reaction, microstructure and simulation of metakaolin-based geopolymers at extended Si/Al ratios, Cem Concr Compos 79 (2017) 45–52. https://doi.org/10.1016/j.cemconcomp.2017.01.014.

[34] M.S. Muñiz-Villarreal, A. Manzano-Ramírez, S. Sampieri-Bulbarela, J.R. Gasca-Tirado, J.L. Reyes-Araiza, J.C. Rubio-Ávalos, J.J. Pérez-Bueno, L.M. Apatiga, A. Zaldivar-Cadena, V. Amigó-Borrás, The effect of temperature on the geopolymerization process of a metakaolin-based geopolymer, Mater Lett 65 (2011) 995–998. https://doi.org/10.1016/j.matlet.2010.12.049.

[35] M. Mastali, P. Kinnunen, A. Dalvand, R. Mohammadi Firouz, M. Illikainen, Drying shrinkage in alkali-activated binders – A critical review, Constr Build Mater 190 (2018) 533–550. https://doi.org/10.1016/j.conbuildmat.2018.09.125.

[36] P. Duan, C. Yan, W. Zhou, W. Luo, Thermal Behavior of Portland Cement and Fly Ash–Metakaolin-Based Geopolymer Cement Pastes, Arab J Sci Eng 40 (2015) 2261–2269. https://doi.org/10.1007/s13369-015-1748-0.

[37] I. Khan, T. Xu, A. Castel, R.I. Gilbert, M. Babaee, Risk of early age cracking in geopolymer concrete due to restrained shrinkage, Constr Build Mater 229 (2019). https://doi.org/10.1016/j.conbuildmat.2019.116840.

[38] S. Wallah, Creep behaviour of fly ash-based geopolymer concrete, , Civ. Eng. Dimens. 12 (2) (2010) 73–78 12 (2010) 73–78.

[39] T. Yang, H. Zhu, Z. Zhang, Influence of fly ash on the pore structure and shrinkage characteristics of metakaolin-based geopolymer pastes and mortars, Constr Build Mater 153 (2017) 284–293. https://doi.org/10.1016/j.conbuildmat.2017.05.067.

[40] F. Škvára, S. Pavlasová, L. Kopecký, L. Myšková, L. Alberovská, 3rd International Symposium on Non-traditional Cement and Concrete, in: High Temperature Properties of Fly Ash-Based Geopolymers, 2008: pp. 741–750.

[41] Z. Zhang, J.L. Provis, A. Reid, H. Wang, Fly ash-based geopolymers: The relationship between composition, pore structure and efflorescence, Cem Concr Res 64 (2014) 30–41. https://doi.org/10.1016/j.cemconres.2014.06.004.

[42] P. Duxson, G.C. Lukey, F. Separovic, J.S.J. van Deventer, Effect of Alkali Cations on Aluminum Incorporation in Geopolymeric Gels, Ind Eng Chem Res 44 (2005) 832–839. https://doi.org/10.1021/ie0494216.

[43] M. Criado, A. Fernández-Jiménez, A. Palomo, Alkali activation of fly ash: Effect of the SiO2/Na2O ratio. Part I: FTIR study, Microporous and Mesoporous Materials 106 (2007) 180–191. https://doi.org/10.1016/j.micromeso.2007.02.055.

[44] N. Granizo, A. Palomo, A. Fernandez-Jiménez, Effect of temperature and alkaline concentration on metakaolin leaching kinetics, Ceram Int 40 (2014) 8975–8985. https://doi.org/10.1016/j.ceramint.2014.02.071.

[45] E. Najafi Kani, A. Allahverdi, J.L. Provis, Efflorescence control in geopolymer binders based on natural pozzolan, Cem Concr Compos 34 (2012) 25–33. https://doi.org/10.1016/j.cemconcomp.2011.07.007.

Turkish Journal of Civil Engineering, 2024, 65-86, Paper 788, ***Research Article***

Generational Transformation and Its Reflection on Project Success: The Gen-Z

Ali Ersen ÖZEN[1]
Gökhan DEMIRDÖĞEN[2]
Alperen Taha DEMIRBAĞ[3]
Hande ALADAĞ[4]
Zeynep IŞIK[5*]

ABSTRACT

Nowadays, Gen-Z members with a high ability to use high-tech products have just entered the labor market to take responsibility in construction projects. Gen-Z members must work together with other generations and different work styles. If the harmonization among generations is not managed properly, it will decrease the productivity of the construction industry. Therefore, this study aims to identify the Gen-Z characteristics and their impacts on the project success by using Structural Equation Modeling (SEM) method. SEM results showed that Gen-Z characteristics contribute to project success through communication. Therefore, communication-related practices must be overviewed and rearranged according to Gen-Z requirements. The findings will contribute to the in-company employee strategies and assist in adapting Gen-Z members into the construction industry to increase productivity.

Keywords: Construction industry, generation Z, innovation, performance management, human resource management.

Note:
- This paper was received on October 13, 2023 and accepted for publication by the Editorial Board on June 14, 2024.
- Discussions on this paper will be accepted by January 31, 2025.
- https://doi.org/10.18400/tjce.1375064

1 Technische Universität München, Germany
ge87lat@mytum.de - https://orcid.org/0009-0004-2595-2531

2 Department of Civil Engineering, Yildiz Technical University, Istanbul, Türkiye
gokhand@yildiz.edu.tr - https://orcid.org/0000-0002-2929-2399

3 Department of Civil Engineering, Yildiz Technical University, Istanbul, Türkiye
demirbag@yildiz.edu.tr - https://orcid.org/0000-0002-9631-1158

4 Department of Civil Engineering, Yildiz Technical University, Istanbul, Türkiye
haladag@yildiz.edu.tr - https://orcid.org/0000-0001-7627-8699

5 Department of Civil Engineering, Yildiz Technical University, Istanbul, Türkiye
zeynep@yildiz.edu.tr - https://orcid.org/0000-0002-7849-8633

* Corresponding author

1. INTRODUCTION

The size of the global construction industry is expected to achieve $14 trillion by 2025. However, compared to other industries, the construction industry, in which the labor productivity growth is less than 1%, is the only industry that cannot improve its productivity over the past 50 years [54]. One of the underlying reasons why labor productivity suffers is the shortage of qualified workers and experienced managers in that field. These human resources-related issues also trigger quality issues in the construction industry [70]. Besides these, the loss of company intellectual capital depending on the aging population is one critical problem threatening the construction industry [11]. Moreover, the construction industry is currently facing a loss of experienced labor due to Covid-19, as in all industries. After the Covid-19 pandemic, some employees and employers either decide to shift their career paths to new jobs or make retirement decisions [11]. Therefore, companies are forced to bring multi-generations (Baby boomers, Generation X, Y, and Z) together to achieve their organizational targets [42] and to create a favorable environment to enable knowledge transfer to each other over the years for ensuring the continuity of the company. However, having employees from multi-generations with different working styles necessitates human resource management carefully. For example, Generation X is senior representatives of companies or employers. They are more autonomous, skeptical, and self-directed and require a balanced work-life. From these generations, Generation Y wants to get more responsibility at work and to know more details about their work, whereas Gen Z is more demanding and harder to manage because of the lifelong learning expectation from their endeavors and desire to improve their skills [9].

There are a significant number of models that represent a spectrum of employee motivation and corresponding management styles, such as “Theory of Needs”, “Intrinsic versus Extrinsic Motivation” and “Theory X, Theory Y, and Theory Z” [55]. According to the “Theory X, Theory Y, and Theory Z” model, members of Generation X lack ambition and goals to work for income, while members of Generation Y are intrinsically motivated and have leadership qualities. Gen-Z members, on the other hand, are driven by self-realization, values, and welfare [55]. As understood from these theories, managers must change their structure developing style regarding the relationship between internal employees and the management into a more individual or generation-focused manner.

Currently, Gen-Z members are working together with other generations and will form the future construction industry for ongoing 50 years. Additionally, in some sources, changes in the construction industry labor market are attributed to changes in the demographics of the construction industry [70] that arise from generational differences. Therefore, managers should raise their awareness of Gen-Z employees to develop effective management styles and sustain harmonization among multi-generations in the workplace [56]. Accurate management styles or strategies can turn working with Gen-Z into an opportunity while mismanaging or being insensitive can jeopardize project success. Therefore, it is inevitable to develop a managerial method for this generation rather than an order to be established by trial and error. Within this context, [42] stated that if employers respond to the needs of employees from different generations, they can benefit from their increased productivity. [15] stated that devising new strategies according to the needs of Gen-Z is crucial to accommodate Gen-Z in the workplace since their expectations, values, and anticipations are different. From the perspective of human resources practices, this generational transformation needs to be

managed for overcoming both the bleak picture of employment practices and the poor image related to workforce relations [68]. According to the authors, every generation has its values, and understanding these values is crucial to conceive the employment relationship [24]. Therefore, human resource managers and project managers should concentrate on generational differences [67], [68].

The literature review showed that there is one study investigating the effect of Gen-Z on the construction industry. In this study, [11] it is aimed to develop strategies to integrate Gen-Z into the construction industry only with a literature review. Based on this background, this study aims to identify the characteristics of Gen-Z and understand the impact of Gen-Z on project success by using the Structural Equation Modeling (SEM) method. In this study, two hypotheses given below will be mainly investigated:

1. There is a direct relationship between Gen-Z characteristics and project success.

2. There is a direct relationship between the innovational impact of Gen-Z and project success.

The results of this study will be a crucial gain for the construction industry to accurately analyze the characteristics of Gen-Z. With the developing technologies and changes in labor sources, the efficient and productive work of different generations has become a matter of curiosity for companies. Thus, the results obtained from this study would pioneer the development of new methods and increase employee satisfaction and project success.

2. LITERATURE REVIEW ON PREVIOUS GEN-Z STUDIES

In the literature, various studies were performed to describe the attitudes and behaviors of Gen-Z in the workplace. However, their attitudes, values, and behaviors remain a mystery, especially in the construction industry. In line, research on the impact of Gen-Z is limited, especially in the context of the construction industry. Table 1 summarizes hitherto studies on Gen-Z in terms of their research topics and findings.

Table 1 - The literature review about Gen-Z.

Research topics	Findings	References
Main characteristics of Gen-Z	Positive, problem solver, innovator, out-of-the-box thinker, negative if the accommodation period is less than one year, assimilative for organizational values, ability to reach new markets, engaging automation design for work, and fast learner, self-confident, creative, career-focused, result-oriented and precision, better at IT knowledge, have powerful technical and language skills compared to other generations	[9], [56], [41]

Workplace attitudes of Gen-Z	Expectations related to the workplace can be different within Gen-Z individuals. In line, the authors emphasized that there is a diversity of Gen-Z's workplace motivations in the same generation cohort.	[9], [37]
	Gen-Z is attracted via flexible work practices, reward and recognition, compensation and benefits, feedback-seeking behavior, and volunteering work.	[2], [32]
	Gen-Z is more open to sharing their personal information with others. Moreover, they prefer to take advice from their friends, family members, or peers rather than superiors.	[36]
	Work environment, compensation, and work-related issues are the most important aspects of a job search situation.	[51]
Motivators/Expectations of Gen-Z in the Workplace	Gen-Z seeks financial stability and extrinsic regulation material. Furthermore, they are more committed employees, and their intrinsic motivation is higher than other generations.	[42]
	Gen-Z seeks transparency, self-reliance, flexibility, personal freedom, acknowledgment, respect for thoughts and ideas, development opportunities, building several parallel careers, flexible schedules, feedback, and maintaining a personal life.	[13]
	Finding the dream job, entrepreneurial initiative, creativity, innovation, opportunities to expand skills, career-minded, and taking delight.	[41]
Communication habits among Gen-Z members	Gen-Z creates its own documents/databases, uses the web for research, and uses e-mail/IM/text as the main communication method.	[13], [31]
Relationship between project management competencies and Gen-Z	Gen-Z traits are more related to project management with soft skills.	[41]
Relationship between organizational belonging and Gen-Z	The feeling of belonging to an organization is a mediation factor between a self-directed, boundaryless attitude and the Gen-Z turnover intention.	[12]

The literature review shows that numerous studies have dealt either with the main characteristics of the Gen-Z or the workplace attitudes of Gen-Z to make suggestions about managerial actions to attract, motivate and retain the Gen-Z. Since the main characteristics of Gen-Z and their workplace attitudes have been well discussed in the literature, there is a lack of rigorous literature to determine the project success impact of Gen-Z and its investigation specific to the construction industry.

3. IDENTIFICATION OF FACTORS AFFECTING PROJECT SUCCESS IMPACT OF GEN-Z

This study aims to identify the characteristics of Gen-Z and to understand the project success impact of Gen-Z using the Structural Equation Modelling (SEM) method. Therefore, indicators related to the characteristics of Gen-Z and project success were examined. Depending on the literature review, a questionnaire was created to implement the SEM method. In this section, factor structures and their variables were introduced. Table 2 demonstrates the model consisting of 6 factors, namely the Innovation Input Factor, Psychological Factor, Working Area Behavioural Factor, Communication Factor, Gen-Z Characteristics Factor, and Project Success Factor. These factors consist of a total of 23 different variables determined from the literature, which affect the interoperability of Gen-Z and other generations and determine the character of Gen-Z.

Table 2 - Definition of factors and variables.

Factors	Variables	Definitions	References
Working Area Behavioral Factor (WRK)	WRK1-Positive approach to new ideas	A positive attitude toward new ideas	[61], [21]
	WRK2-Knowing what they are good at	Knowing their predispositions and limits Ready for the challenges and testing themselves	
	WRK3-Realistic approach	Observed with a tendency of Gen-Z's addiction to social media	
Communication Factor (CMN)	CMN1-Ability to express themself	Shaped by watching the contents of the peers on the internet	[39], [7], [22], [59]
	CMN2-Setting an equal style in the communication method	Focusing on freedom and equality during communication	

	CMN3-Dialogue rather than discussion	Tendency to the dialogue due to libertarian and equal views of Gen-Z	
Psychological Factor (PSC)	PSC1-Social effects of growing up in a protective family	Parents of Gen-Z are more protective and achievement-oriented.	[59], [56], [2],[49]
	PSC2-Psychological support	The rates of anxiety and depression requiring psychological support are higher among Gen-Z.	
	PSC3-Support about awareness of the limits	Gen-Z members need psychological assistance to discover their limits in the business environment.	
	PSC4-Reliance on research rather than rumors	Gen-Z members are the most active users of the internet. They take note of the studies and proven facts rather than tacit knowledge.	
Gen-Z Characteristics Factor (GENZ)	GENZ1-Initial role	The members of Gen-Z regard success as making a difference. Also, they perceive themselves as initiator.	[41], [42], [56], [52], [34], [9]
	GENZ2-Ability to internalize client requests	Gen-Z has a positive approach to listening to other people's thoughts. Therefore, they are open to the ideas and requests of clients.	
	GENZ3-Do it yourself generation	The members of Gen-Z are ambitious and individualist.	
	GENZ4-Leadership abilities	The leadership abilities of the members of Gen-Z were found higher than neutral points.	
	GENZ5-Technology sophistication	Gen-Z has better IT knowledge than other generations.	

Innovation Input Factor (INV)	INV1-Freedom in working method	The members of Gen-Z demand more flexibility in their working methods to support their desire for work.	[9], [5], [56], [13], [1], [2],
	INV2-Original thinking ability	The members of Gen-Z are out-of-the-box thinkers against other generations.	
	INV3-Knowledge	They have more tendency to use web resources to invent or discover something.	
	INV4-Investment	Investment is one of the most important triggering factors for innovations.	
	INV5-Consultancy	Constant feedback requirement is one of the attributes of Gen-Z. It is also crucial for innovations.	
Project Success Factor (PSS)	PSS1-Decrease in project duration	Shortening the project length in the construction industry is one of the most decisive indicators of project success.	[26], [5], [50], [51] [7], [35], [16]
	PSS2-Decrease in project cost	Cost management of construction projects is essential in determining the income-expense balance of the project from a holistic perspective.	
	PSS3-Increase in client satisfaction	Sectors continue their existence by making, developing, and facilitating what people want. Nowadays, with the increasing level of modernity, consumer expectations are dynamically changing.	

4. RESEARCH METHODOLOGY

This study aims to identify the characteristics of Gen-Z and to understand the project success impact of Gen-Z using the Structural Equation Modelling (SEM) method. The SEM method is frequently used to investigate the relationships between dependent and independent variables. This method is defined as a combination of exploratory factor analysis, confirmatory factor analysis, and path analysis, as it includes observed and latent variables at the same time [66]. While confirmatory factor analysis tests whether the created models are validated on the data set, Path analysis is the analysis of many simultaneous regression equations among observed variables [20]. In other words, SEM shows direct or indirect relationships between latent variables. SEM method can be used to estimate the error

variance, to consider unobservable variables or phenomena, to present a holistic model, to test the model holistically, to perform operations on data sets that are not normally distributed and with missing data, and to allow simultaneous testing of the connection between dependent and independent variables [3]. Therefore, this study employed the SEM method to discover relationships between the characteristics of Gen-Z and project success.

4.1. Data Collection

A data set of the study was collected from 144 construction workers born between 1994-2010 (members of Gen-Z) by conducting face-to-face surveys. Participants were from different disciplines such as field engineers, architects, technical office engineers, and contract engineers. The relevant sample set was found to be sufficient to perform SEM analysis (sample set > 5 observations*23 variables = 115) [69]. The survey study consists of two separate parts. General information about the participants was collected in the first part of the questionnaire. In the second part, participants were asked to evaluate model indicators using a 1-5 Likert scale (1 represents I disagree, 5 represents I strongly agree).

4.2. Data Analysis

As stated above, the SEM analysis consists of a normality test, exploratory factor analysis, confirmatory factor analysis, and path analysis (structural analysis). In this study, IBM SPSS Statistics V21 and IBM SPSS AMOS V21 programs were used to perform statistical and SEM analyses.

4.2.1. Normality Test and Exploratory Factor Analysis

Before starting the analysis, the normality distribution test of the data sets was performed. It is stated in the literature that the Barlet test, Skewness and Kurtosis value, and one of the Liliegor tests can be used to test the normality distribution since the model goodness-of-fit indices will not give good results and the analysis results will be affected by this distribution if the data is not normally distributed. Within the scope of the study, Skewness and Kurtosis tests were used. This value is expected to be between -1.5 and +1.5 [63]. The Skewness and Kurtosis values of all variables considered within the scope of the study are within the value range specified in the literature [17].

If the researcher does not know the exact relationship between the observed and the unobservable variable and does not take factor groups from the literature, the researcher needs to perform exploratory factor analysis [65]. The survey questions used to create the variables under the factor groups in the study were determined as a result of the literature review. However, since the variables in question were not completely included in the study and the accuracy of the factor structures was not tested, exploratory factor analysis was performed, and the data analysis was started [62]. Thanks to factor analysis, the variables that are thought to be related can be grouped under a smaller number of unobservable variables.

Kaiser-Mayer-Olkin (KMO) measurement of sampling adequacy value and Bartlett's test of sphericity were checked to measure the correlations between the variables and the suitability of the factor analysis in exploratory factor analysis, respectively. The KMO value should be between 0 and 1. The closer the KMO value is to 1, the more suitable the sample is for factor

analysis. A KMO value of 0.8 and above is excellent, while a value below 0.5 is unacceptable [62]. In this context, the result of the KMO test was found to be 0.773. The Bartlett test, on the other hand, decides whether the correlation between the variables is sufficient. As a result of the Bartlett test, the significance value (p value) is expected to be below 0.05. In this context, the p value was found to be 0.00. This result proved that there is a relationship between the variables and the underlying structure [27].

Revealing the anti-image correlation matrix specific to the data set is one of the essential criteria for factor analysis. While performing the factor analysis, rotation was performed to show in which factor clusters the variables were collected more intensively. In this context, the varimax option was chosen because it was thought that there was a relationship between the factor structures [25].

Another crucial criterion for factor analysis is that the explained variance value should exceed 50% of the total variance. In this context, as a result of the exploratory factor analysis, it was determined that the relevant factor group explained 65,975% of the total variance, and it was found to be greater than 50%. Factor loadings above 0.2 are acceptable for modeling [14]. This limit is provided in the model [27].

Cronbach's Alpha values were checked to measure the reliability of the factor groups that emerged as a result of the exploratory factor analysis. In this context, this value is expected to be at least 0.7 [66]. However [40] stated that Cronbach's Alpha value can be acceptable if it is between 0,5 and 0,7. The findings showed that the results are admissible. Table 3 demonstrates a summary of the analysis results.

Table 3 - The exploratory factor analysis results

Factor Groups	**Code**	**Variable Definitions**	**Factor load**	**Cronbach Alpha Value**
Working Area Behavioral Factor (WRK)	WRK1	Positive approach to new ideas	0,835	0,808
	WRK2	Knowing what they are good at	0,825	
	WRK3	Realistic Approach	0,761	
Communication Factor (CMN)	CMN1	Ability to express themselves	0,803	0,894
	CMN2	Setting an equal style in communication method	0,887	
	CMN3	Dialogue rather than discussion	0,887	
Psychological Factor (PSC)	PSC1	Social effects of growing up in a protective family	0,828	0,738
	PSC2	Psychological support	0,870	
	PSC3	Support about awareness of the limits	0,660	
	PSC4	Reliance on research rather than rumors	0,593	

Generation Z Characteristics Factor (GENZ)	GENZ1	Initial role	0,699	0,830
	GENZ2	Ability to internalize client request	0,446	
	GENZ3	"Do it yourself" generation	0,730	
	GENZ4	Leadership Abilities	0,744	
	GENZ5	Technology sophistication	0,830	
Innovation Input Factor (INV)	INV1	Freedom in working method	0,649	0,783
	INV2	Original thinking ability	0,697	
	INV3	Knowledge	0,749	
	INV4	Investment	0,729	
	INV5	Consultancy	0,748	
Project Success Factor (PSS)	PSS1	Decrease in Project duration	0,850	0,797
	PSS2	Decrease in Project cost	0,800	
	PSS3	Increase in client's satisfaction	0,830	

According to Table 3, all factor groups' Cronbach's Alpha Values are over 0.7, meaning that they are all acceptable values.

4.2.2. Confirmatory Factor Analysis

Confirmatory factor analysis can also be named as the measurement model in literature [62]. Confirmatory factor analysis helps to reveal the relationship between the factor structures that are revealed as a result of exploratory factor analysis and to confirm the resulting structures. Within the scope of confirmatory factor analysis, the AMOS package program was used. Therefore, the errors that occur in the model should be revealed with standardized residuals, modification indices, and conformity tests. If the analysis results provide the conditions, a structural model is used to create the path model, and the structural analysis is performed [8].

"Covariance correction" and "regression correction" indices are items of modification indices [8]. In this context, both covariance correction indices and regression correction indices were checked. In the analysis performed under the covariance correction indices, the highest covariance values (9,504) were found among the error terms of GENZ2 and GENZ4. As a result of the regression analysis, the highest regression was found between GENZ2 and PSC3 variables (9,547). If the Chi-square test value is higher than 2 or 3, these values are used to improve the model by making corrections on the relevant variables [33], [30]. In this context, the result of the confirmatory factor analysis showed that the Chi-square test value is 1.288. Therefore, there is no need for correction on the model.

The fitness indices were examined to test the accuracy of the factor structures. There is no consensus in the literature for selecting certain fitness indices and using them as a confirmatory factor or structural model analysis evaluation criteria. In this context, in this

study, the Chi-square, the goodness-of-fit statistic, the goodness-of-fit index (GFI), the comparative fit index (CFI), and the root mean square of approximation (RMSEA) indices were used.

Chi-square the goodness-of-fit statistic is calculated by dividing the Chi-square value by the degree of freedom. The goodness-of-fit index that was described by Jöreskog and Sörbom in 1984 is another index to measure model fit. The formula for GFI is given in Eq. 1. According to the notation of the formula, $\Sigma\hat{}$ represents the estimated covariance matrice matrix for observed variables from the restricted model, S represents the covariance matrice from the unrestricted model, and tr( ) represents the sum of diagonal elements [48].

$$GFI = 1 - \frac{tr\left(\hat{\Sigma}^{-1}S - I\right)^2}{tr\left(\hat{\Sigma}^{-1}S\right)^2} \quad (1)$$

The CFI is used to measure relative improvement from the baseline model to the postulated model (Eq. 2). In Eq. 2, while Fk represents the postulate model, F0 represents the baseline model [61].

$$CFI = 1 - \frac{F_k}{F_0} \quad (2)$$

The RMSEA helps to measure discrepancy per degree of freedom. The equation of RMSEA is given in Eq. 3. In Eq. 3, F_k represents the discrepancy between the population covariance matrix and the implied covariance matrix, df_k denotes the degree of freedom [61].

$$RMSEA = \sqrt{\frac{F_k}{df_k}} \quad (3)$$

In this context, Table 4 demonstrates the results obtained from the AMOS software. The analysis results showed that all indices are within limits.

Table 4 - Control of conformity index results of confirmatory factor analysis.

Compatibility Indices	Literature	Results	Reference
χ2/df	<3	<3	[26]
GFI	0= no fit ; 1= perfect fit	0= no fit ; 1= perfect fit	[61]
CFI	0= no fit ; 1= perfect fit	0= no fit ; 1= perfect fit	[61]
RMSEA	<0,1	<0,1	[34]

Additionally, the construct reliability of the latent variables was measured via Construct Reliability (CR) analysis. This analysis helps to evaluate the inner quality of the model. The values of CR need to be higher than 0,7. The analysis results are shown in Table 5.

Table 5 - The composite reliability values (CR).

Working Area Behavioral Factor	Communication Factor	Psychological Factor	Generation Z Characteristics Factor	Innovation Factor	Project Success Factor
0,815	0,897	0,773	0,811	0,786	0,802

4.2.3. Path Analysis (Structural Model Analysis)

When the factor loadings and the goodness fit indices for the model were not improved with the change in the model through literature studies, and factor loadings and the goodness fit indices were within acceptable limits, the structural model analysis ended [45], [28]. More technically, in structural analysis, the quantification of the explained and unexplained variance between latent variables is performed [29]. The structural model emerges by combining one or more linear regression equations. The analysis results of coefficients are called the path for co-efficiency [8].

SEM analysis is used in the literature to analyse latent variables which cannot be measured directly. In this context, the relationship between the latent variables "Innovation Factors", "Psychological Factor", "Working Area Behavioral Factors", "Communication Factors", "Gen-Z Characteristic Factors", and "Project Success Factors" was analysed with IBM AMOS V21. As a result of the analysis, the fitness indices of the model remained within the allowed ranges (Table 6).

Table 6 - Control of conformity index results of structural model analysis.

Compatibility Indices	Literature	Results	Reference
CMIN/df	<3	1,267	[61]
GFI	0= no fit ; 1= perfect fit	0,857	[61]
CFI	0= no fit ; 1= perfect fit	0,951	[61]
RMSEA	<0,1	0,043	[34]

As a result of the structural analysis, the significance levels of the path coefficients were also tested with the t-test. All p-values below 0.05 were significant [8].

Before the SEM analysis, the model was used to analyse the relationship between factor groups and to measure the factor loads. After the SEM analyses, the model shows the factors and variables to measure the impact of Gen-Z Characteristics on innovations in the construction industry (Figure 1). The arrows represent the effecting direction of factors, and the numbers on the arrows are factor loads.

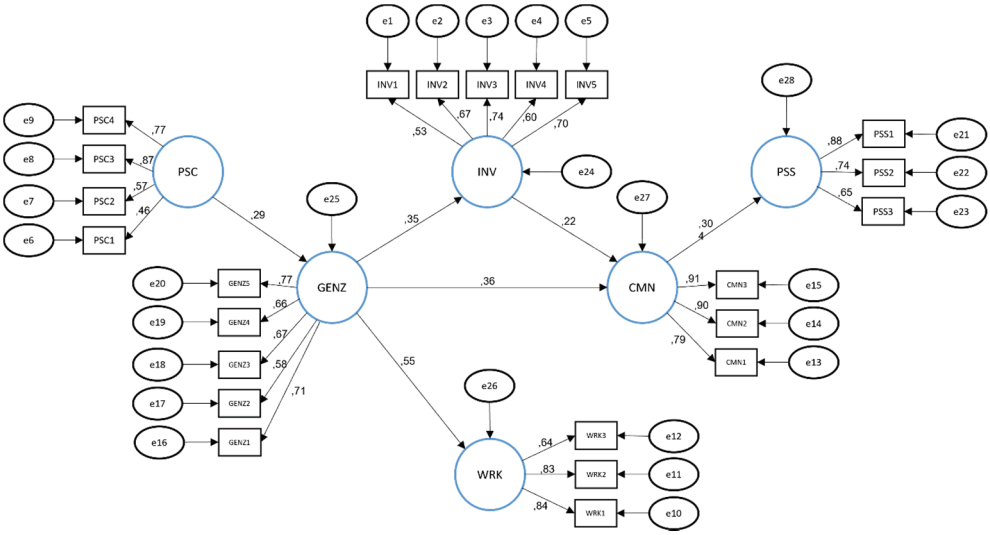

Figure 1 - Results of Structural Equation Model Analysis

As a result of the SEM analysis, it was determined that the "Innovation (INV)" factor group affects the "Communication (CMN)" factor group. It was observed that the "Psychological (PSC)" factor group affects the "Gen-Z Characteristic (GENZ)" factor group. The "Work Area Behavioral (WRK)" factor is affected by the "Gen-Z Characteristic (GENZ)" factor group. Finally, the "Communication (CMN)" factor group has a mediator role between the "Innovation (INV)", "Gen-Z Characteristic (GENZ)" and "Project Success (PSS)" factor groups.

The highest factor loads were found in the "Knowledge" variable (0.74) under the "Innovation factor", "Support about awareness of the limits" variable (0.71) under the "Psychological factor", "Psychological support" variable (0.87) under the "Working area behavior factor", "Setting an equal style in communication method" variable (0.90) under the "Communication factor", "Technology sophistication" variable (0.77) under the "Gen-Z Characteristic factor", and "Decrease in Project duration" variable (0.88) under the "Project success factor".

5. DISCUSSION

The study aimed to identify the characteristics of Gen-Z and to understand the impact of Gen-Z on project success by using the Structural Equation Modelling (SEM) method. The SEM analysis showed that communication management is the key to achieving project success. In other words, the "There is a direct relationship between Gen-Z characteristics and project success" and "There is a direct relationship between the innovational impact of Gen-Z and project success" hypotheses were rejected. However, their indirect impacts on "project success" were discovered via the "communication" factor.

The nature of construction projects requires a collaborative working environment in which different expertise is shared and combined to construct physical buildings. Within this context, teams are built up and dissolve during the building life cycle. Moreover, each team has its own project managers, who are engaged from different organizations and their complicated bureaucracy. Therefore, the harmony and interconnection between teams, in-team relationships (including intergenerational communication [42]), and expectation management of stakeholders are crucial to achieving project success in construction projects [19]. According to the results of this study, Gen-Z members who are internal project stakeholders demand more open communication to motivate themselves to conduct project-related activities since they have grown up in an era of social media and digital communication where collaboration and teaming are important. In other words, they demand open communication channels to express themselves in problem-solving and implementing innovative ideas. Thus, the Gen-Z members can feel that they are the part of the solution. However, the construction industry is less innovative, transparent, and highly bureaucratic than other industries. Therefore, neglecting the communication-related factors in the project will cause innovative ideas to vanish or the innovation impact of Gen-Z to vanish. Acknowledging and managing these differences is crucial to creating a positive work culture and improving motivation for integrating Gen-Z members into the construction industry [42].

As Figure 1 displays, Gen-Z individuals value sincere relations rather than hierarchical order. Hence, it will be beneficial to perform project meetings, team lunches, office debates, and team-building activities such as the blind retriever game, perfect square game, two truths-one lie game, et cetera. These activities will increase sincerity, communication, creative thinking, teamwork, and building relationships in construction projects. In construction projects, the selection of communication tools may also help to increase sincerity for Gen-Z members. Since they have more familiarity with mobile applications. In other words, apart from the e-mail communication as a channel, using more common and daily communication networks (WhatsApp, Telegram, et cetera.) can contribute to communication success in organizations. However, considering the majority of Gen-Z are distracted while using their smartphone for non-work-related activities [31] [53], the selection of workplace communication tool's effect on employee productivity comes to the forefront as a serious issue.

Furthermore, the global construction industry suffers from productivity losses. In this context, improving the performance and productivity of the labor force are key elements for the successful completion of construction projects [44]. Productivity is related to how efficiently resources are used to achieve organizational goals [44]. Therefore, the effective use of Gen-Z and their abilities will affect the future of construction industry. According to the study results, members of the Gen-Z demand support for using their "technology sophistication" in construction tasks. Therefore, Gen-Z, digital natives [64], can be utilized to improve the low digitalization level of the construction industry and productivity in construction projects. Considering technological advances such as BIM, IoT, AR, VR, and Robotics, adopting Construction 4.0 emerges as one of the necessities the construction industry should achieve. However, due to the conventional manufacturing type of the industry, it is challenging for construction companies to adopt Construction 4.0. Within this context, Gen-Z has impromptu technology that can fuel companies' growth and success [2]. However, while integrating Gen-Z into construction projects to increase innovation, "psychological support" needs to be given to them since Gen-Z members depend on support due to high anxiety and depression [59, 56]. This psychological support may include actions

to increase their motivation. Rather than a reward or punishment system, motivational sources such as an arrangement of working hours by themselves or participating in training may be more convenient to increase their job commitment.

Because of the fragmented structure of construction projects, high labor turnover is another issue in the construction industry. The high labor turnover may directly cause to need for coaching support to reduce Gen-Z members' job loss perception. Therefore, as individuals distance themselves from anxiety, work-related stress, and overwhelming workloads, productivity increases in Gen-Z can be observed. In other words, prioritizing the mental health and well-being of Gen-Z can influence the efficiency of the project [60]. However, fostering a supportive environment where they can freely express themselves by setting an equal dialog must be considered with the supportive working environment. Furthermore, the industry's poor image regarding workforce perception often results in hiring low-educated laborers, potentially leading to communication competence issues among employees. Therefore, communication should be prioritized to fill the gap and use the effectively in construction activities.

The analysis results interestingly showed that "working area behaviour" did not have a direct effect neither on the success of the project, or innovation input factor. The underlying reason behind this result can be that "WRK2-knowing what they are good at" and "WRK3-Realistic approach" discourage them to participate in innovations, and the reluctance endangers project success directly. Also, this finding confirms the importance of communication factors to courage them. The importance of WRK2 (knowing what they are good at) in the study shows that the awareness of the GENZ members and their potential in the job is high. Regarding the construction industry, construction projects are complex and contain a high degree of uncertainty. Within this context, the Gen-Z member's realistic approach can help perform due diligence on the project.

Psychological factors are one of the subcomponents of effective leadership (the second most essential indicator under the Gen-Z characteristics factor) in the project-based environment [57]. Also, this finding can be seen in the effect of the PSC factor on the Gen-Z characteristics factor. Another important finding in the literature is that psychological factors play an important role in entrepreneurship [38]. Entrepreneurship is related to leading change. Being entrepreneurship can be attributed to the initiator role and "Do it yourself" characteristics of Gen-Z. Therefore, it can be inferred that psychological factors affect Gen-Z characteristics.

As a consequence, employers should let Gen-Z employees share their knowledge and opinions. Communication among colleagues will help improve Gen-Z's mental health and well-being and support the innovativeness of companies and project success. Furthermore, when things go wrong, candid communications at the friend level rather than as a manager may be more helpful to explain themselves and allow them to correct themselves.

6. CONCLUSION

The construction industry's workforce comprises individuals from multiple generations. Among these, Gen-Z stands out due to its proficiency with high technology and entrepreneurial attributes. Leveraging the potential of Generation Z within the construction sector holds promise for addressing long-standing industry challenges. However, the

literature review analysis showed that the study has focused on the relationship between Gen-Z characteristics and project success. Within this context, 23 variables under 6 factors were identified at the end of the literature review. 144 surveys were collected, and the collected data were analyzed according to the SEM methodology to discover the factor groups and the relationship between factors. As a result of SEM analysis, the direct relationship between Gen-Z and project success was not found. Instead, it uncovered the mediating role of the "Communication" factor. Additionally, our findings underscore the significant influence of Gen-Z on fostering “Innovation” within the construction industry, while also shedding light on the impact of “Psychological” factors on Gen-Z.

As a result of the analysis, the below inferences can be made from the study:

- Granting Gen-Z members autonomy in their work methods can significantly enhance productivity [9, 13]. Conversely, prolonged working hours have been shown to decrease productivity and elevate stress levels [30]. Moreover, research suggests that remote work fosters creativity. Various strategies exist to promote work-life balance, such as part-time employment, flexible schedules, transportation assistance, and adaptable job arrangements, which construction companies can implement to boost productivity [6]. Within this context, reducing onsite work hours for construction workers not only mitigates health and safety risks but also enhances the innovative capacity and productivity of Gen-Z individuals [43]. Construction firms should leverage evolving technological opportunities and implement improvements beneficial to employees' mental well-being to incorporate these forward-looking strategies as much as possible.

- Gen-Z members should not solely rely on online information but also communicate with their more experienced colleagues to fulfill their practical information needs. In this context, brainstorming sessions can prove beneficial in enhancing the creativity and productivity of Gen-Z during idea-generation sessions [4]. Moreover, Gen-Z members are highly familiar with the use of new technologies. These brainstorming sessions might facilitate their sharing of technical knowledge with colleagues. Simultaneously, as experienced colleagues offer solutions to problems, this interaction could support the learning process of Gen-Z members.

- This study has shown that the counselling effect needed to psychologically support Gen-Z members is also a necessary input for innovation. Therefore, coaching, and mentoring programs can be helpful in uncovering talents. There are different types of coaching programs, such as external coaches and coaching in an organization, made by managers. In this study, the authors propose using internal coaching made by managers so that managers can optimize individual and organizational goals with employees by aligning them. Besides, managers can give constructive feedback about Gen-Z members’ progress at work. Thus, the positive impact of coaching programs on employee satisfaction, individual performance, and organizational goals can be realized [47].

- The members of Gen-Z are aware that they need investment to put their ideas into practice, and if their ideas are innovatively acceptable and viable, it is of great importance to support these ideas with investment. Therefore, construction companies should allocate funds in their budgets for their employees to innovate [18].

- Furthermore, understanding their areas of success can foster a greater appreciation for business life among Gen-Z members, motivating them to strive for continuous improvement in their work. In this regard, facilitating interdepartmental transfers can help unearth their potential and contribute to organizational learning [10]. For instance, if a Gen-Z member is dissatisfied with their current position or experiencing low productivity, assigning them tasks in a different department could potentially boost their effectiveness and creativity. Additionally, Norman's (1986) Gulf of Evaluation and Execution method, typically utilized in Information Systems (IS) development and evaluation, can be adapted to assess and enhance Gen-Z members' retention within organizations [23]. By applying this method, any disparities between employee intentions, particularly those of Gen-Z members, and organizational objectives can be identified. If misalignments are detected, it is essential to evaluate whether the Gen-Z members' expectations are beneficial to the organization. In such cases, organizational adjustments should be considered to align with their expectations effectively. For construction companies, implementing such a method can aid in pinpointing any mismatches between the intentions of employees, especially those belonging to Gen-Z, and the overarching objectives of the organization. Upon identifying such discrepancies, it becomes imperative to assess the extent to which the expectations of Gen-Z members contribute positively to the organization's goals. In instances where their expectations prove advantageous, it is crucial for construction firms to contemplate organizational adjustments that effectively align with these expectations. This alignment is essential for fostering a work environment conducive to the productivity and satisfaction of Gen-Z employees within the construction industry.
- The characteristics of Gen-Z are open to new ideas. However, since they think about events from their perspectives and reach conclusions this way, what they do or think does not appear as a result of other people's ideas or wishes, but as an inference from their perspectives. Therefore, two-way communication between Gen-Z members and experienced workers or managers should be used as a facilitator to convince them. If managers choose one-way communication, Gen-Z members will not be willing to share their ideas. In other words, managers or colleagues give them a chance to say something about their jobs and lives. This enablement also helps the engagement of Gen-Z. Besides these, sharing power with Gen-Z members can strengthen the sense of belonging [46].
- Managers must keep their social communication levels at equal level and ensure that two employees at the same level pay attention to this level, even if they are from different generations. Within this context, the expectations of Gen-Z members from organizations are different in terms of organizational structures. They are expected to work in horizontal organizational structures (deciding without getting manager approval) [43].

The model proposed as a result of SEM analysis can be used to integrate Gen-Z members into construction companies in a way that more innovation is obtained. Moreover, using the study outputs with some recommendations can increase the efficiency of Gen-Z in construction projects. Eventually, the proposed model can be used to measure the performance of the innovational impact of Gen-Z and their impact on project success in the construction industry. Especially since the effect of field workers on productivity is high in the construction sector, research can be conducted on how Gen-Z can become more productive than the workers working as other generations.

References

[1] Adams, R., Bessant, J., & Phelps, R. (2006). Innovation management measurement: A review. *International journal of management reviews*, 8(1), 21-47.

[2] Aggarwal, A., Sadhna, P., Gupta, S., Mittal, A., & Rastogi, S. (2020). Gen Z entering the workforce: Restructuring HR policies and practices for fostering the task performance and organizational commitment. *Journal of Public Affairs*, e2535.

[3] Aladag, H., Demirdogen, G. and Isik, Z. (2021), "Investigation of dispute factors and effects on construction projects arising from COVID-19 pandemic as a force majeure event", *Journal of the Faculty of Engineering and Architecture of Gazi University*, 36(3), 1214-1228.

[4] Al-Samarraie, H., & Hurmuzan, S. (2018). A review of brainstorming techniques in higher education. *Thinking Skills and creativity*, 27, 78-91.

[5] Aouad, G., Ozorhon, B., & Abbott, C. (2010 Aouad: Directions and implications for research and policy. *Construction innovation*. 10(4), 374-394.

[6] Apraku, K., Bondinuba, F. K., Eyiah, A. K., & Sadique, A. M. (2020). Construction workers work-life balance: A tool for improving productivity in the construction industry. *Social Work and Social Welfare*, 2, 45-52.

[7] Arashpour, M., & Arashpour, M. (2015). Analysis of workflow variability and its impacts on productivity and performance in construction of multistory buildings. *Journal of Management in Engineering*, 31(6), 1-9.

[8] Bacon, L. D. (1994). Using Amos for structural equation modeling in market research. *SPSS white paper*, 1-18.

[9] Bencsik, A., Horváth-Csikós, G., & Juhász, T. (2016). Y and Z Generations at Workplaces. *Journal of competitiveness*, 8(3), 90-106.

[10] Boone, T., & Ganeshan, R. (2008). Knowledge acquisition and transfer among engineers: Effects of network structure. *Managerial and Decision Economics*, 29(5), 459-468.

[11] N. Borg and N. Scott-Young, C. Naderpajouh, "Managing to Retain Generation Z in the Construction Industry," in *44th Australasian Universities Building Education Association Conference*, 2021, pp. 109–119.

[12] Botezat, E., Fotea, S. L., Marici, M., & Fotea, I. S. (2020). Fostering the Mediating Role of the Feeling of Belonging to an Organization Among Romanian Members of Gen-Z . *Studia Universitatis Vasile Goldiș Arad, Seria Științe Economice*, 30(4), 69-91.

[13] Bucovețchi, O., Slușariuc, G. C., & Činčalová, S. (2019). Generation Z-Key Factor For Organizational Innovation. *Quality-access to success*, 20.

[14] Child, D. (2006). *The essentials of factor analysis*. A&C Black.

[15] Chillakuri, B. (2020). Understanding Generation Z expectations for effective onboarding. *Journal of Organizational Change Management*, 33(7), 1277-1296.

[16] Dawes, J., Stocchi, L., & Dall'Olmo-Riley, F. (2020). Over-time variation in individual's customer satisfaction scores. *International Journal of Market Research*, 62(3), 262-271.

[17] Desgagné, A., & Lafaye de Micheaux, P. (2018). A powerful and interpretable alternative to the Jarque–Bera test of normality based on 2nd-power skewness and kurtosis, using the Rao's score test on the APD family. *Journal of Applied Statistics*, 45(13), 2307-2327.

[18] Doran,J. & Ryan,G.(2017).The role of stimulating employees' creativity and idea generation in encouraging innovation behaviour in Irish firms. *The Irish Journal of Management*, 36(1) 32-48.

[19] Faraji A, Rashidi M, Perera S, Samali B. Applicability-Compatibility Analysis of PMBOK Seventh Edition from the Perspective of the Construction Industry Distinctive Peculiarities. *Buildings*. 2022; 12(2):210.

[20] Fornell, C., Larcker, D.F., 1981. Structural equation models with unobservable variables and measurement error: algebra and statistics. *J. Mark. Res*. 18 (3), 382–388.

[21] Francis, T., & Hoefel, F. (2018). True Gen': Gen-Z and its implications for companies. *McKinsey & Company*, 12.

[22] Gaidhani, S., Arora, L., & Sharma, B. K. (2019). Understanding the attitude of Gen-Z towards workplace. *International Journal of Management, Technology and Engineering*, 9(1), 2804-2812.

[23] Gemino, A., & Wand, Y. (2004). A framework for empirical evaluation of conceptual modeling techniques. *Requirements Engineering*, 9, 248-260.

[24] Gifford, R., & Nilsson, A. (2014). Personal and social factors that influence pro-environmental concern and behaviour: A review. *International journal of psychology*, 49(3), 141-157.

[25] Goretzko, D., Pham, T. T. H., & Bühner, M. (2021). Exploratory factor analysis: Current use, methodological developments and recommendations for good practice. *Current Psychology*, 40(7), 3510-3521.

[26] Gunduz, M., & Yahya, A. M. A. (2018). Analysis of project success factors in construction industry. *Technological and Economic Development of Economy*, 24(1), 67-80.

[27] Howard, M. C. (2016). A review of exploratory factor analysis decisions and overview of current practices: What we are doing and how can we improve?. *International Journal of Human-Computer Interaction*, 32(1), 51-62.

[28] Iacobucci, D. (2009). Everything you always wanted to know about SEM (structural equations modeling) but were afraid to ask. *Journal of Consumer Psychology*, 19(4), 673-680.

[29] Ikediashi, D. I., Ogunlana, S. O., & Udo, G. (2013). Structural equation model for analysing critical risks associated with facilities management outsourcing and its impact on firm performance. *Journal of Facilities Management*, 11(4), 323-338.

[30] Jaiswal, A., & Arun, C. J. (2020). Unlocking the COVID-19 lockdown: work from home and its impact on employees.

[31] Janssen, D., & Carradini, S. (2021). Gen-Z workplace communication habits and expectations. *IEEE Transactions on Professional Communication*, 64(2), 137-153.

[32] Jayathilake, H. D., Daud, D., Eaw, H. C., & Annuar, N. (2021). Employee development and retention of Generation-Z employees in the post-COVID-19 workplace: a conceptual framework. Benchmarking: *An International Journal*, 28(7), 2343-2364.

[33] Kärnä, S., Junnonen, J. M., & Sorvala, V. M. (2009). Modelling structure of customer satisfaction with construction. *Journal of facilities management*, 7(2), 111-127.

[34] Kirpik, G. (2020). Entrepreneurship, professionalism, and leadership intention of Gen-Z : The case of Kahta. *SEISENSE Journal of Management*, 3(2), 58-72.

[35] Kog, Y. C., & Loh, P. K. (2012). Critical success factors for different components of construction projects. *Journal of construction engineering and management*, 138(4), 520-528.

[36] Lazányi, K., & Bilan, Y. (2017). Generetion Z on the labour market: do they trust others within their workplace?. *Polish Journal of Management Studies*, 16(1), 78-92.,

[37] Leslie, B., Anderson, C., Bickham, C., Horman, J., Overly, A., Gentry, C., & King, J. (2021). Gen-Z perceptions of a positive workplace environment. *Employee Responsibilities and Rights Journal*, 33(3), 171-187.

[38] Li, J., Qu, J., & Huang, Q. (2018). Why are some graduate entrepreneurs more innovative than others? The effect of human capital, psychological factor and entrepreneurial rewards on entrepreneurial innovativeness. *Entrepreneurship & Regional Development*, 30(5-6), 479-501.

[39] Loosemore, M. (1998). The influence of communication structure upon management efficiency. *Construction Management & Economics*, 16(6), 661-671.

[40] Ma, Z., Pi, G., Dong, X., & Chen, C. (2017). The situation analysis of shale gas development in China-based on Structural Equation Modeling. *Renewable and Sustainable Energy Reviews*, 67, 1300-1307.

[41] Magano, J., Silva, C. S., Figueiredo, C., Vitória, A., & Nogueira, T. (2021). Project management in engineering education: Providing Gen-Z with transferable skills. *Ieee Revista Iberoamericana De Tecnologias Del Aprendizaje*, 16(1), 45-57.

[42] Mahmoud, A. B., Fuxman, L., Mohr, I., Reisel, W. D., & Grigoriou, N. (2020). “We aren't your reincarnation!” workplace motivation across X, Y and Z generations. *International Journal of Manpower*, 42(1), 193-209.

[43] Maioli, E. (2017). New Generations and Employment â€“An Exploratory Study about Tensions Between the Psycho-social Characteristics of the Generation Z and Expectations and Actions of Organizational Structures Related with Employment (CABA, 2016). *Journal of Business*, 2(1), 01-12.

[44] Manoharan, K., Dissanayake, P., Pathirana, C., Deegahawature, D., & Silva, R. (2024). Assessing the performance and productivity of labour in building construction projects through the application of work-based training practices. *Construction Innovation*, 24(2), 558-583.

[45] Malkanthie A., (2015), Structural Equation Modeling with AMOS, Panadura,Sri Lanka: Nippon Graphics Pvt. Ltd.

[46] Markos, S., & Sridevi, M. S. (2010). Employee engagement: The key to improving performance. *International journal of business and management*, 5(12), 89.

[47] McCarthy, G., & Milner, J. (2013). Managerial coaching: challenges, opportunities and training. *Journal of Management Development*, 32(7), 768-779.

[48] Mulaik, S. A., James, L. R., Van Alstine, J., Bennett, N., Lind, S., & Stilwell, C. D. (1989). Evaluation of goodness-of-fit indices for structural equation models. *Psychological bulletin*, 105(3), 430-445.

[49] Onsongo, E. K., & Schot, J. (2017). Inclusive innovation and rapid sociotechnical transitions: the case of mobile money in Kenya.

[50] Ozorhon, B., & Oral, K. (2017). Drivers of innovation in construction projects. *Journal of construction engineering and management*, 143(4), 04016118.

[51] Pataki-Bittó, F. (2021). Work environment transformation in the post COVID-19 based on work values of the future workforce. *Journal of Corporate Real Estate*, 23(3), 151-169.

[52] Panwar, S., & Mehta, A. (2019). Fostering Leadership in Gen-Z : Onus on Whom?. IUP *Journal of Soft Skills*, 13(3), 65-70.

[53] Pandita, D. (2021). Innovation in talent management practices: creating an innovative employer branding strategy to attract generation Z. *International Journal of Innovation Science*, 14(3/4), 556-569.

[54] Park, J. K., & Lee, K. W. (2022). Efficiency Analysis of Construction Automation Using 3D Geospatial Information. *Sensors and Materials*, 34(1), 415-425.

[55] PMBOK (2021) A guide to the project management body of knowledge, *Project Management Institute*, 7th Ed., Pennsylvania, USA.

[56] Racolţa-Paina, N. D., & Irini, R. D. (2021). Gen-Z in the Workplace through the Lenses of Human Resource Professionals–A Qualitative Study. *Calitatea*, 22(183), 78-85.

[57] Redick, A., Reyna, I., Schaffer, C., & Toomey, D. (2014). Four-factor model for effective project leadership competency. *Journal of Information Technology and Economic Development*, 5(1), 53-68.

[58] Sange, R., & Srivasatava, R. K. (2012). Employee Engagement and Mentoring: An Empirical Study of Sales Professionals. *Synergy* (0973-8819), 10(1).

[59] Schroth, H. (2019). Are you ready for Gen Z in the workplace?. *California Management Review*, 61(3), 5-18.

[60] Shan, M., Li, Y. S., Hwang, B. G., & Chua, J. E. (2021). Productivity metrics and its implementations in construction projects: A case study of Singapore. *Sustainability*, 13(21), 12132.

[61] Shi, D., Lee, T., & Maydeu-Olivares, A. (2019). Understanding the model size effect on SEM fit indices. *Educational and psychological measurement,* 79(2), 310-334.

[62] Shuck, B. & Reio Jr, T. G., (2015). Exploratory factor analysis: implications for theory, research, and practice. *Advances in Developing Human Resources*, 17(1), 12-25.

[63] Tabachnick, B. G., Fidell, L. S., & Ullman, J. B. (2007). Using multivariate statistics, *Pearson Education*, 5, 481-498.

[64] Turner, A. (2015). Gen-Z : Technology and social interest. *The journal of individual Psychology*, 71(2), 103-113.

[65] Watkins, M. W. (2018). Exploratory factor analysis: A guide to best practice. *Journal of Black Psychology*, 44(3), 219-246.

[66] Weston, R., & Gore Jr, P. A. (2006). A brief guide to structural equation modeling. *The counseling psychologist*, 34(5), 719-751.

[67] Williams, K. C., & Page, R. A. (2011). Marketing to the generations. *Journal of behavioral studies in business*, 3(1), 37-53.

[68] Wilkinson, A., Johnstone, S., & Townsend, K. (2012). Changing patterns of human resource management in construction. *Construction Management and economics*, 30(7), 507-512.

[69] Wolf, E. J., Harrington, K. M., Clark, S. L., & Miller, M. W. (2013). Sample size requirements for structural equation models: An evaluation of power, bias, and solution propriety. *Educational and psychological measurement*, 73(6), 913-934.

[70] Yankov, L., & Kleiner, B. H. (2001). Human resources issues in the construction industry. *Management Research News*, 24(3/4), 101-105.

Turkish Journal of Civil Engineering, 2024, 87-106, Paper 789, ***Research Article***

Comparison of the Dynamic Characteristics of Tuned Liquid Column Dampers with Different Elbow Forms

Mert Can AYDEMIR[1]
Erdem DAMCI[2*]
Yener TAŞKIN[3]
Çağla ŞEKERCI[4]

ABSTRACT

This study aims to examine experimentally the damping performance of Tuned Liquid Column Dampers (TLCD) by considering different elbow forms. Experiments carried out within the scope of the study point out the dynamic characteristics of TLCD, which has 45 (open) and 90 (closed) degree-elbow forms with theoretical angular frequencies that are the same. Experiments consist of ±5 and ±10 mm harmonic excitation amplitude to observe the relationship between the damping ratio and head loss coefficient with the mass ratio of the TLCD. These experiments with an incremental mass ratio of 0.05% from 0.80% to 1.00% and with an incremental mass ratio of 0.10% from 1.00% to 1.20% had been carried out in detail. Mass and stiffness Modification Factors (MF) are suggested to minimize the difference between numerical and experimental results. Determined MFs are used to examine the earthquake performance of TLCD on a Single-Degree-of-Freedom (SDOF) system. It is shown that the open elbow has an advantage of approximately 25% over the close elbow under earthquake performance on the SDOF system.

Keywords: Tuned liquid column dampers, passive control, shaking table experiments, earthquake simulation.

Note:
- This paper was received on November 19, 2023 and accepted for publication by the Editorial Board on June 14, 2024.
- Discussions on this paper will be accepted by January 31, 2025.
- https://doi.org/10.18400/tjce.1393000

1 İstanbul University-Cerrahpaşa, Department of Civil Engineering, İstanbul, Türkiye
Istanbul Beykent University, Department of Civil Engineering, İstanbul, Türkiye
mertcan.aydemir@ogr.iuc.edu.tr - canaydemir@beykent.edu.tr - https://orcid.org/0000-0001-5341-5697

2 İstanbul University-Cerrahpaşa, Department of Civil Engineering, İstanbul, Türkiye
edamci@iuc.edu.tr - https://orcid.org/0000-0003-2295-1686

3 İstanbul University-Cerrahpaşa, Department of Mechanical Engineering, İstanbul, Türkiye
ytaskin@iuc.edu.tr - https://orcid.org/0000-0003-1923-2672

4 Doğuş University, Department of Civil Engineering, İstanbul, Türkiye
csekerci@dogus.edu.tr - https://orcid.org/0000-0001-7070-1804

* Corresponding author

1. INTRODUCTION

Passive dampers are used to reduce the effects of a certain level of vibration caused by strong wind or strong ground motions. Passive dampers can reduce the effects of these vibrations in the short term by increasing the energy absorption capacity of the structure to which they are applied, thereby increasing the occupant comfort for the building. One of the passive dampers, the TLCD with the same cross-sectional area in the horizontal and vertical columns, was introduced in the literature by Sakai [1], and its nonlinear mathematical model was described. Researchers [2-7] have carried out experimental and theoretical studies on U-shaped TLCD systems in the following years when numerical and parametric studies have been carried out on the optimum tuning ratio and head loss coefficient values for TLCD systems [8-13]. At the same time, these studies have shown that the TLCD effective length requirement can be easily achieved by choosing different cross-section ratios in the vertical and horizontal columns. Although it is generally accepted in the literature that the mass ratio varies between 0.05% and 5%, it has been shown that there is a correlation between this ratio and the performance of the TLCD, and that the optimum mass ratio is an important consideration in obtaining the optimum damping ratio [12]. It was concluded that the mass ratio should generally be less than 2% for TLCD to be effective and that TLCD efficiency increases as the mass ratio value increases [8]. However, this conclusion is not entirely correct for U-shaped TLCDs with a constant cross-sectional area. As the mass ratio value increases, the control performance of the TLCD decreases as it moves away from the optimum tuning ratio and length ratio values [12, 14]. The studies in the literature focus mainly on single-degree-of-freedom (SDOF) system models. To compare the control performance of passive dampers in Multi Degree of Freedom (MDF) systems, Bigdeli and Kim [15] compared the effects of different dampers on the damping of the structure on a three-story model. Some studies have investigated the relationship between the optimum head loss coefficient and the aperture ratio when controlling the vibrations occurring in the structure under the effect of stochastic loads and concluded that TLCD is more effective in reducing the acceleration and displacement values of the structure when the length ratio and mass ratio are high [16].

In another study on the seismic applications of single TLCD systems and multiple TLCD systems, a single-degree-of-freedom bridge model and a 10-story building model were used. According to the study, design parameters for single and multiple TLCD systems were determined using 72 different earthquake records. These parameters for STLCD were the tuning ratio, the damping ratio, and the ratio of the effective fluid length to the TLCD column width. These parameters for MTLCD are the central tuning ratio, the tuning bandwidth, and the number of TLCD groups. The results showed that the acceleration and displacement responses of the models were reduced by 47% [17]. In another study on multiple TLCD, the dynamic characteristics of the multiple TLCD system are numerically investigated. In addition, the advantages of this system are presented by comparing it with a single TLCD system. The study revealed that the multiple TLCD system has a specific frequency range and damping ratio value to reduce the peak responses under harmonic excitation. In addition, the study also states that more than 5 TLCDs do not show a significant change in improving system performance [18]. These studies have shown that Multiple TLCD performs better and is more effective than single TLCD during seismic events. Multiple TLCDs were found to have a certain optimum center distance ratio. However, placing more than a certain number of multiple TLCDs in the structure did not increase the effectiveness of the system.

In another study on the control performance of the structural system and TLCD [19], it was shown that the performance is related to the acceleration and displacement responses of the structure, depending on the structural system. Considering the acceleration responses of a shear wall system and a frame system with similar stiffness, it was stated that TLCD achieved more effective control performance in the shear wall system. Other theoretical and experimental studies carried out in recent years have developed different forms of TLCDs. The control performance of some new types of TLCDs has been compared with conventional types [20-23]. A pre-design formula was developed by Matteo et al. [24] using statistical methods to calculate the linear equivalent damping ratio of a TLCD, and later, this formula was experimentally investigated on a TSD system [25].

Other studies have examined the control performance of Liquid Column Vibration Absorbers (LCVA) on structures, which is a type of TLCD [26-28]. The dynamic characteristics and control performance of the LCVAs were investigated experimentally and theoretically.

One of the passive type damper derived from the configuration of TLCD is called the Pendulum type liquid damper, which has been experimentally and numerically studied in the literature [32-33].

Tuned liquid dampers (TLDs) are designed to passively control vibrations in structural systems. They consist of a container partially filled with liquid and utilize the liquid's sloshing dynamics to mitigate structural vibrations. The liquid's oscillatory movement generates a force that is directly correlated with its horizontal acceleration. The TLD's control performance and sloshing characteristics have been investigated in various studies under harmonic loads [34-36].

In this study, the effects of harmonic excitation amplitude, elbow form, and mass ratio on TLCD performance are investigated. For this purpose, the dynamic characteristics of two different TLCD designs with the same theoretical angular frequencies consisting of 45 (open elbow) and 90 (close elbow) degree elbow forms are presented. Experimentally obtained dynamic characteristics and damping ratios are compared with theoretical results. Additionally, time history analyses are carried out numerically on the SDOF system using experimentally obtained parameters. The control performance of TLCD is investigated by considering the elbow forms, and adjusted numerical analyses are performed.

2. TLCD SYSTEM DESIGN and EXPERIMENTAL SETUP

TLCDs with open elbow (OE) and close elbow (CE) forms of equal cross-sectional area in horizontal and vertical columns, using PVC material with an external diameter of 75 mm and an internal radius of 35.5 mm were used. For the vertical columns, transparent acrylic material of the same dimensions was preferred. Figure 1 shows the view of the OE and CE TLCDs, and Figure 2 shows the experimental models placed on the shaking table [29]. Frequency-mass relations, head loss coefficient-mass ratio relations, mass ratio-damping ratio relations, and resonance amplitudes for TLCDs with OE and CE were investigated by frequency scanning tests. A uniaxial shaking table controlled by a stepper motor with a stroke of ± 75 mm was used for this purpose. The dimensions and masses of OE and CE TLCD systems are shown in Table 1.

Table 1 - TLCD specifications

TLCD type	Mass (kg)	Outer width (L_1)	Clear width (B)
OE TLCD	1.554	286	211
CE TLCD	1.500	283	208

The equation of motion of the liquid in the TLCD shown in Figure 1 is given in Equation (1).

$$m_d \ddot{y}(t) + \frac{1}{2}\rho A \xi |\dot{y}(t)| \dot{y}(t) + 2\rho A g y(t) = -m_h \ddot{x}_g(t) \tag{1}$$

A is the cross-sectional area of the TLCD, m_d is the fluid mass (ρAL) in the TLCD, m_h is the mass of the fluid in the horizontal column of the TLCD, g is the acceleration of gravity, $\ddot{x}_g$ is the ground acceleration, *y, ẏ, and ÿ* are the displacement, velocity, and acceleration of the fluid in the TLCD, respectively. ρ and ξ represent the density of the fluid and the head loss coefficient, respectively.

The numerical solution of the differential equation is challenging due to the nonlinear terms in the dynamic equation associated with TLCD. Therefore, these terms are typically linearized using an equivalent linearization technique [37]. The error between the nonlinear and equivalent linear systems is expressed in Equation (2) as follows.

$$\varepsilon = \frac{1}{2}\rho A \xi |\dot{y}| \dot{y} - c_{eq} \dot{y} \tag{2}$$

The equivalent damping coefficient is determined through the minimization of the mean square error, leading to the derivation of the expression for the equivalent damping coefficient, assuming the Gaussian distribution of water surface velocity in the water column [9, 13].

$$c_{eq} = \sqrt{\frac{2}{\pi}} \rho A \xi \sigma_{\dot{y}} \tag{3}$$

$\sigma_{\dot{y}}$ denotes the standard deviation of the water surface velocity of the water column. In Equation (4), ζ_{eq} denotes the equivalent damping ratio of the TLCD in Eq. (1). The linearized dynamic equation is as follows.

$$m_d \ddot{y}(t) + 2 m_d \omega_d \zeta_{eq} \dot{y}(t) + m_d \omega_d^2 y(t) = -m_h \ddot{x}_g(t) \tag{4}$$

The tuning ratio χ, a critical parameter in TLCD control performance, is calculated using Equation (5).

$$\chi = \frac{\omega_d}{\omega_s} \tag{5}$$

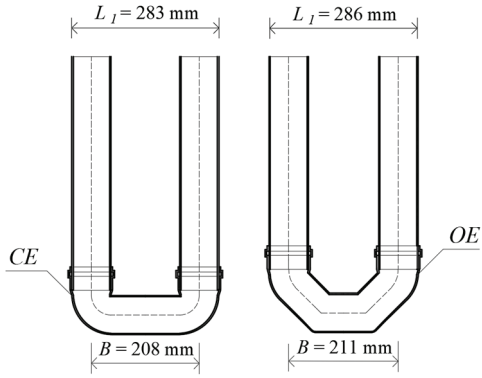

Figure 1 - Design of CE (left), and OE (right) TLCD.

Figure 2 - Views from shake table tests of CE TLCD (left), and OE TLCD (right).

ω_s denote the angular frequency of the structure model, and the angular frequency of the TLCD ω_d is obtained using Equation (6). Tuning ratio of approximately 1 is preferred for the control performance of the TLCD.

$$\omega_d = \sqrt{\frac{2g}{L}} \tag{6}$$

In Equation (6), g represents gravitational acceleration, and L represents the total liquid length in the vertical and horizontal columns. The mass ratio, which is the parameter that affects the control performance of the TLCD and the liquid length L in the system, is calculated using Equation (7).

$$\mu = \frac{m_d}{m_s} \times 100 \tag{7}$$

The mass ratio, mass of the liquid in the TLCD, and mass of the structure are denoted by μ, m_d, and m_s, respectively. In this study, m_s was assumed to be 170 kg.

The half-power bandwidth (3 dB) method is utilized to calculate the damping ratios of experimentally obtained frequency-amplitude curves using Equation (8).

$$\zeta = \frac{f_b - f_a}{2 f_n} \tag{8}$$

Here, f_n is the natural frequency of the TLCD, and f_a and f_b are the projections of the points on the frequency axes of the frequency-amplitude curve that intersect below the maximum by 3 dB.

In order to compare the damping performance of the elbow effect, the non-dimensional Dynamic Response Amplifier (DRA) of the TLCD systems is calculated by Equation (9). The equation is defined by the relationship between the damping ratio and frequency ratio.

$$\mathrm{DRA} = 1 \Big/ \sqrt{\left[1-(\omega/\omega_d)^2\right]^2 + \left[2\zeta(\omega/\omega_d)\right]^2} \tag{9}$$

ω represents the excitation frequency in Equation (9) [30]. Head loss is caused by fluid flow passing through the horizontal column due to the form of the elbows. The friction between the fluid and the inner walls of the TLCD is calculated by Equation (10), where ζ represents the damping ratio, and x_r is the amplitude of the resonance frequency.

$$\xi = 2L\sqrt{\pi}\left(\frac{\zeta}{x_r}\right) \tag{10}$$

3. DETERMINING DYNAMIC CHARACTERISTICS OF TLCDs

Harmonic tests for different amplitude-frequency relationships were performed to determine the dynamic response of TLCD systems considering OE and CE forms. These experiments were carried out for each elbow configuration as frequency scanning tests around the theoretical resonance frequency calculated for the relevant mass ratio. As the TLCD vibrated at the excitation frequency, the fluid oscillation in the transparent columns was measured using an attached ruler. Each harmonic test was settled to 50 cycles for the given excitation frequency to observe the steady-state oscillation in the TLCD column. The experiments were performed with amplitudes of ±5 mm and ±10 mm within a frequency range of 0.85 to 1.40. The objective is to examine the relationship between the damping ratio and amplitude. As a result of these experiments, the frequency response curves obtained for each mass ratio with TLCDs formed with OE and CE are shown in Figures 3-6. Figures 3 and 4 show the OE and CE frequency-response curves under ±5 mm harmonic excitation. In addition, Figure 5 and

Figure 6 show the frequency-response curve of the OE and CE under an amplitude of ±10 mm. The dynamic response of both the OE and CE TLCDs was obtained for mass ratios ranging from 0.80% to 1.20% through frequency scanning.

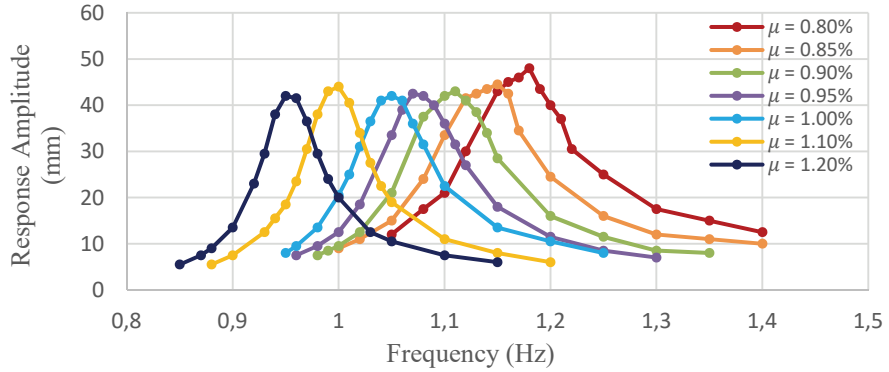

Figure 3 - OE TLCD frequency-response curves under ±5 mm harmonic excitation.

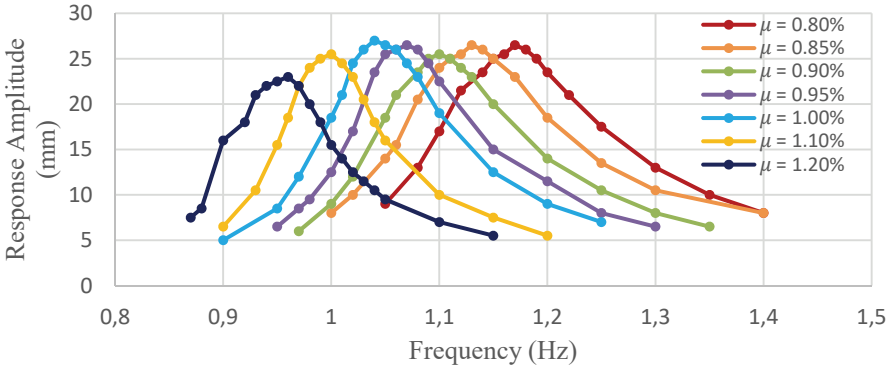

Figure 4 - CE TLCD frequency-response curves under ±5 mm harmonic excitation.

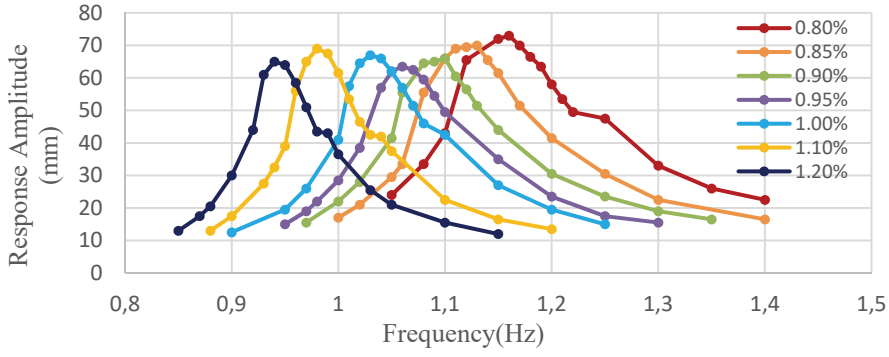

Figure 5 - OE TLCD frequency-response curves under ±10 mm harmonic excitation.

Figure 7 for the OE and Figure 8 for the CE give the frequency-mass ratio relationships under ±5 mm and ±10 mm amplitudes to determine the consistency between the experimental and theoretical results.

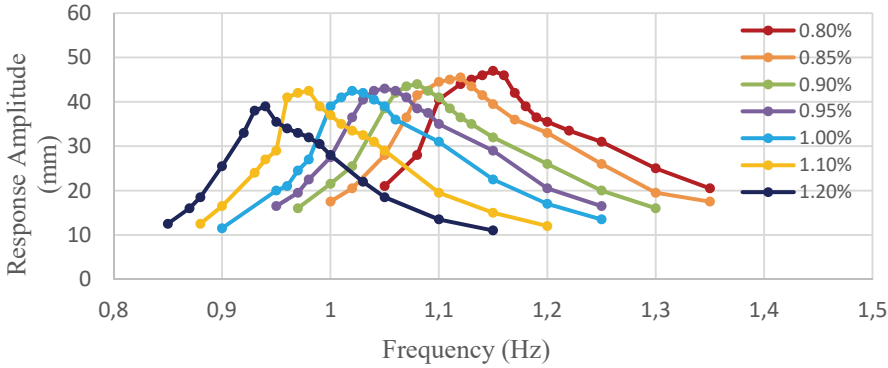

Figure 6 - CE TLCD frequency-response curves under ±10 mm harmonic excitation.

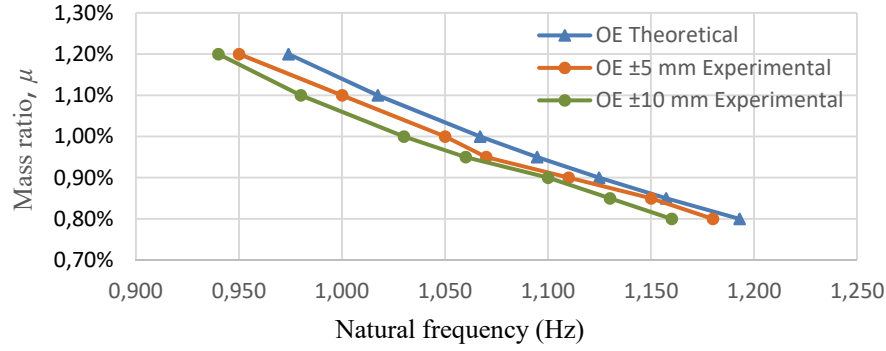

Figure 7 - OE TLCD frequency-mass ratio relation.

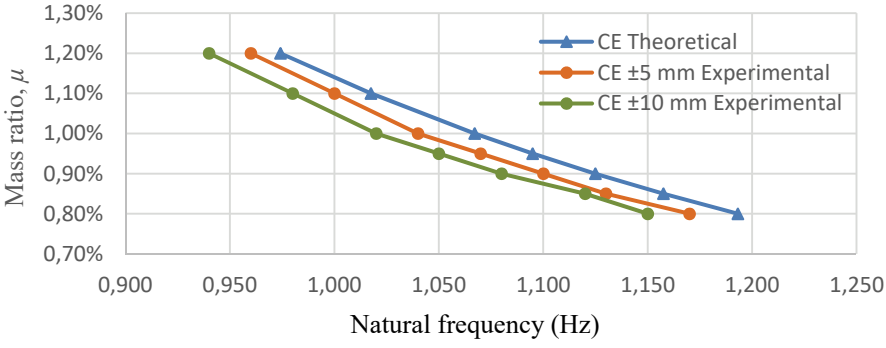

Figure 8 - CE TLCD frequency-mass ratio relation.

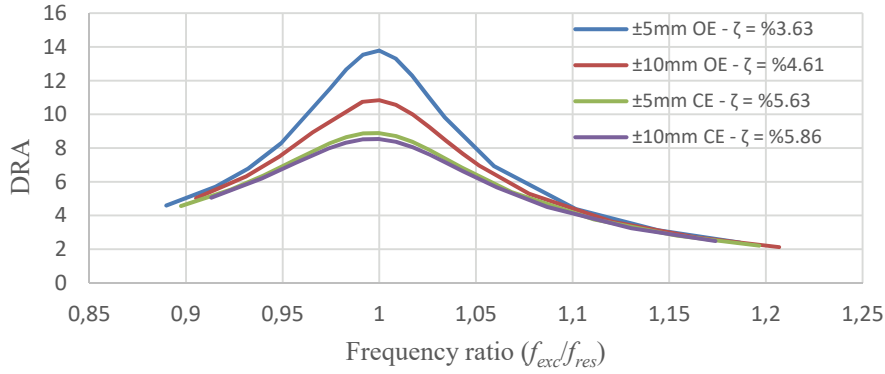

Figure 9 - DRA-frequency ratio relationship for mass ratio 0.80%.

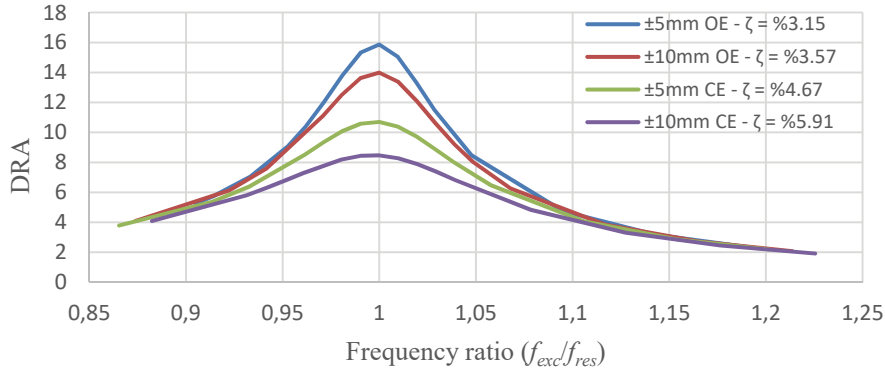

Figure 10 - DRA-frequency ratio relationship for mass ratio 1.00%.

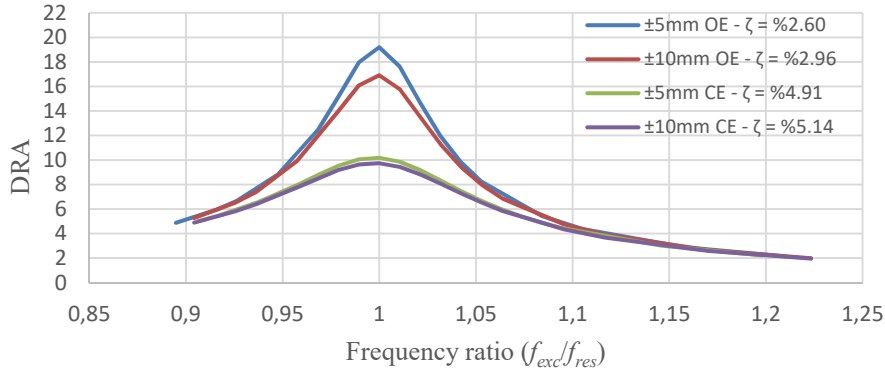

Figure 11 - DRA-frequency ratio relationship for mass ratio 1.20%.

The DRA-frequency ratio curves corresponding to the displacement responses of the system were calculated using Equation (9). DRA-frequency ratio curves were obtained for 0.80%, 1.00%, and 1.20% mass ratios to investigate the effect of OE and CE forms on the damping ratio under harmonic excitation amplitude. Figures 9 - 11 show the DRA-frequency ratio curves for mass ratios of 0.80%, 1.00%, and 1.20%, respectively.

TLCD systems were subjected to frequency scanning tests using a shake table at around resonance frequencies. As a result, Figure 12 shows the peak amplitude values at steady-state oscillation corresponding to the resonant frequencies for two different harmonic excitation amplitudes of TLCDs with OE and CE for different mass ratios.

Figure 13 represents the frequency response curve obtained for an OE form and a mass ratio of 1.20%, which was determined by the frequency scanning test under ±5mm harmonic excitation and between 0.85 Hz and 1.15 Hz. The response amplitude obtained for the system's resonance frequency was observed at 0.96 Hz, which is 41.5 mm. The 3 dB projection points on the frequency axis are calculated as f_a = 0.93 Hz and f_b = 0.98 Hz. As a result, the damping ratio obtained using Equation (8) is 2.6%.

The damping ratio-mass ratio relationships were calculated by applying the 3dB method to the frequency-amplitude curves obtained by the frequency scanning method for OE and CE TLCD systems, as shown in Figure 14. This figure presents the effect of the mass ratio, harmonic excitation amplitude, and elbow form on the damping ratio of the TLCD. The effect of elbow form on response amplitude compared to damping ratio response can be observed from Figures 12 and 14. Although in Figure 12, OE ±5 mm and CE ±10 mm tests give similar results, significant differences can be seen in Figure 14.

The head loss coefficient ξ is determined by the orifice opening ratio, where $\xi = 0$ represents full orifice opening, and $\xi = \infty$ indicates full orifice closure, and it is widely acknowledged in the literature that the head loss coefficient depends not only on the mass ratio but also on the response amplitude of the TLCD [17]. In addition, the head loss is known to be caused by the fluid flow passing through the orifice in the horizontal column of the TLCD, but it can also be due to the form of elbows and the friction between the fluid and the inner walls of the TLCD [31]. In this respect, the head loss coefficients corresponding to the mass ratios were obtained in this study to observe the effect of the elbow form. Figure 15 shows the head loss coefficient corresponding to each mass ratio obtained using Equation (10).

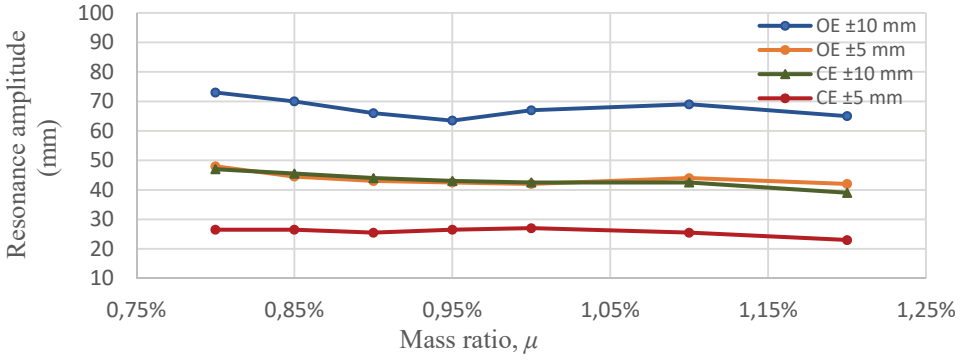

Figure 12 - Resonance amplitudes corresponding to the mass ratio of OE and CE TLCD.

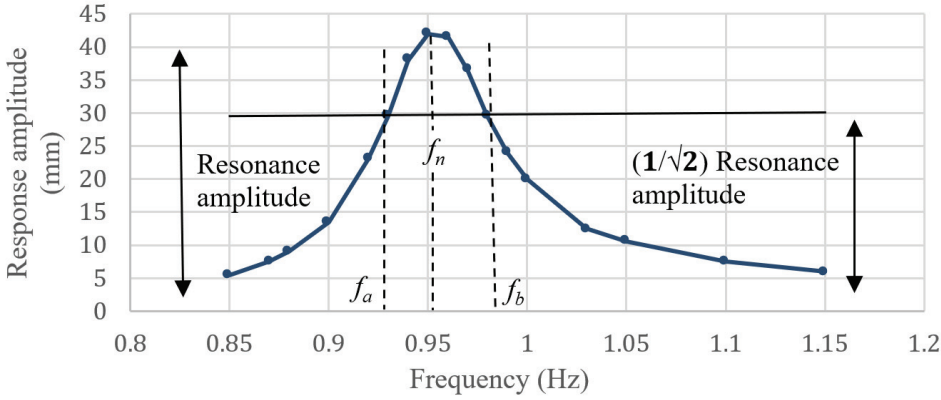

Figure 13 - 3dB method example of frequency response curve for a mass ratio of 1.20%.

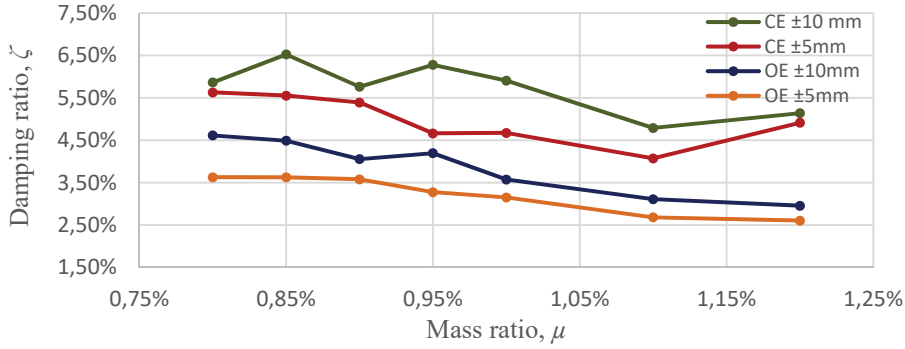

Figure 14 - Damping-mass ratio relation for OE and CE TLCD.

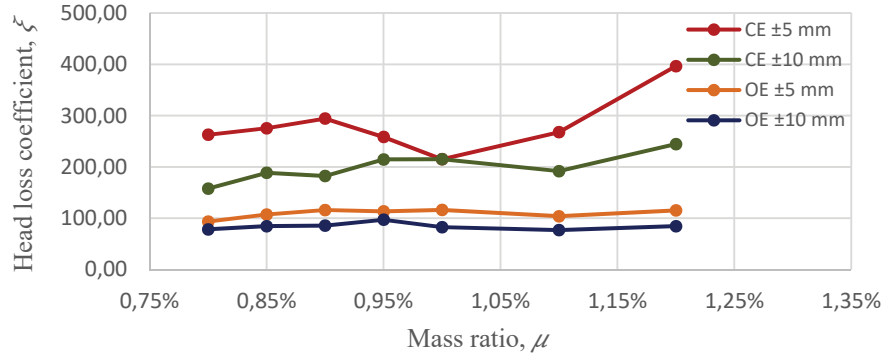

Figure 15 - Head loss coefficient-mass ratio relation for OE and CE TLCD.

4. ADJUSTING THE NUMERICAL ANALYSIS USING EXPERIMENTAL RESULTS

The vibration of a structure is damped by a TLCD through the gravitational restoring force exerted on the displaced fluid within the TLCD. At the same time, energy is dissipated through the viscous interaction between the TLCD fluid and its rigid walls. In addition, energy is lost through the orifices installed inside the TLCD container and elbows area [20, 26]. In this study, numerical analyses revealed that in representing the actual behavior by the equation of motion, an adjustment must be made in accordance with the experimentally determined harmonic behavior of the TLCD. A proposed set of coefficients, called Modification Factors (MF), is suggested to correlate the numerical results with the frequency-amplitude curves obtained from experimental results.

Figures 16 and 17 show numerical and experimental frequency-response curves for the mass ratio of 0.80% for the OE and CE, respectively. The equation proposed by Park et al. [20] with an equivalent damping ratio does not match the experimental results obtained in this study. Replacing the equivalent damping ratio with the experimental damping ratio, although the numerical response amplitude becomes closer to the experimental, resonance frequency shows a significant difference. The reason for this is that some of the liquid in the TLCD cannot participate in the motion due to friction and turbulence occurring in the elbows area. In this respect, mass (α) and stiffness (β) modification factors were obtained by considering experimental results. Equation (11) is used for α and β modification factors to minimize the difference between experimental and numerical results. As an example, using the calculated MF for OE and CE, it is found that the adjusted numerical results are now in good agreement with the experimental results, as shown in Figures 16 and 17. α and β coefficients are determined for the mass ratio of μ= 0.80% as 0.845 and 0.96 for the OE, and 0.975 and 0.95 for the CE, respectively.

$$\alpha m_d \ddot{y}(t) + 2m_d \omega_d \zeta_{eq} \dot{y}(t) + \beta\left(m_d \omega_d^2\right) y(t) = -m_h \ddot{x}_g(t) \tag{11}$$

The comparison of experimental and adjusted numerical results obtained for all mass ratios for CE and OE are shown in Figures 18 and 19, respectively. The mass and stiffness MFs related to this study might be applicable for the length ratio (B/L) resembling the specimens used in the experiments (0.34–0.6). The determined MFs for mass ratios are given in Table 2.

Table 2 - MFs according to mass ratios.

	OE		CE	
Mass ratio, μ (%)	α	β	α	β
0.80	0.845	0.960	0.974	0.950
0.85	0.850	0.965	0.930	0.950
0.90	0.848	0.968	0.941	0.950
0.95	0.8768	0.960	0.991	0.950
1.00	0.880	0.965	0.922	0.950
1.10	0.892	0.959	1.020	0.960
1.20	0.875	0.957	0.859	0.960

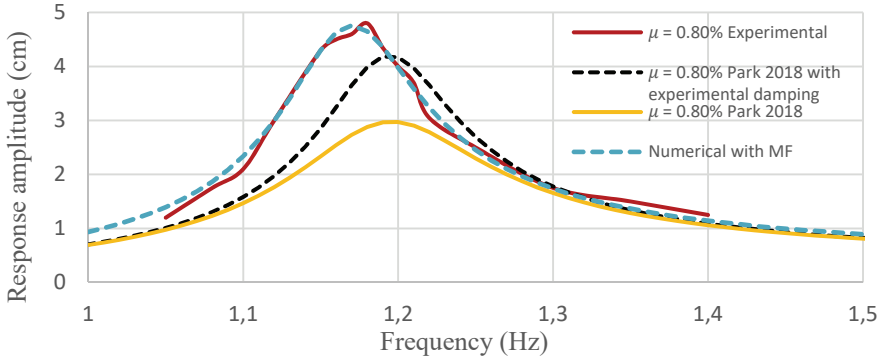

Figure 16 - Frequency-response curve for OE TLCD with a mass ratio of 0.80%.

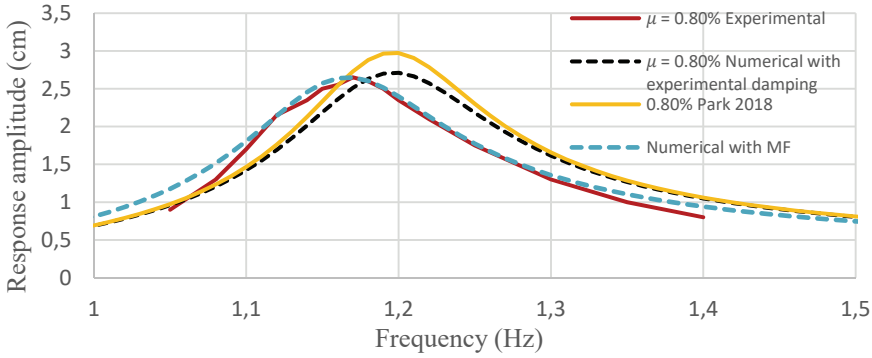

Figure 17 - Frequency-response curve for CE TLCD with a mass ratio of 0.80%.

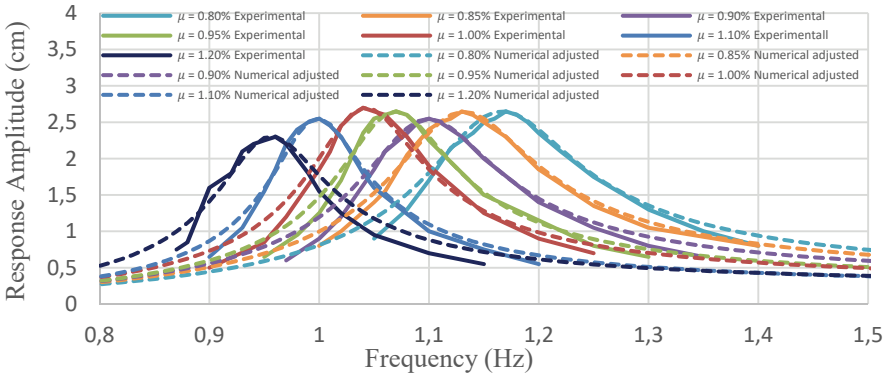

Figure 18 - Adjusted (numerical) and experimental frequency-response curves for CE TLCD.

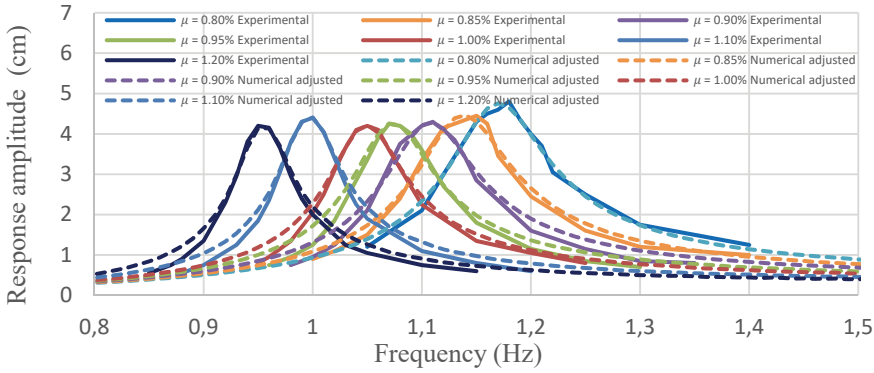

Figure 19 - Adjusted (numerical) and experimental frequency-response curves for OE TLCD.

5. NUMERICAL ANALYSIS OF A SDOF SYSTEM COUPLED WITH TLCD

A SDOF building model is represented to investigate the interaction between the structure and the TLCD. M_s, C_s, and K_s denote the mass, damping, and stiffness of the structure, respectively, as shown in Figure 20b. Horizontal component acceleration records of the 1999 Kocaeli earthquake that is shown in Figure 20a were obtained from the PEER Strong Ground Motion Database [38]. The damping ratio of the SDOF system is assumed to be 5%. M_s and C_s are assumed to be 101.9368 kg (total weight= 1 kN) and 5500 N/cm, respectively. The dynamic equation of the SDOF system coupled with TLCD is expressed in Equation (12). The time history analyses are conducted using the Newmark linear acceleration method [30] using Equation (12).

$$\begin{bmatrix} M_s + m_d & m_h \\ m_h & m_d \end{bmatrix} \begin{Bmatrix} \ddot{x} \\ \ddot{y} \end{Bmatrix} + \begin{bmatrix} C_s & 0 \\ 0 & 2m_d\omega_d\zeta_{eq} \end{bmatrix} \begin{Bmatrix} \dot{x} \\ \dot{y} \end{Bmatrix} + \begin{bmatrix} K_s & 0 \\ 0 & m_d\omega_d^2 \end{bmatrix} \begin{Bmatrix} x \\ y \end{Bmatrix} = -\begin{Bmatrix} M_s + m_d \\ m_h \end{Bmatrix} \ddot{x}_g \qquad (12)$$

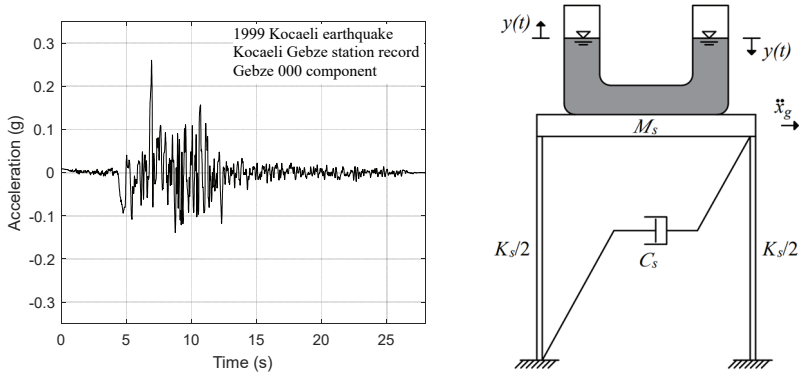

(a) (b)

Figure 20 - (a) Kocaeli Earthquake record, (b) Representation of modeling of TLCD installed on a SDOF system.

The OE and CE TLCDs were found to be successful in reducing the acceleration and displacement responses of the SDOF system. To show the control performance of OE and CE, the root-mean-square (RMS) ratio (r) of the acceleration values was calculated using Equation (13). As a result, the TLCD with an OE reduces the RMS ratio by 14.34%, while the CE reduces it by 11.53%.

$$r = \left(\frac{\mathrm{RMS}_{WOT} - \mathrm{RMS}_{WT}}{\mathrm{RMS}_{WOT}} \right) \times 100 \tag{13}$$

The Kocaeli Earthquake was applied to the SDOF system to examine the seismic performance of OE and CE TLCD systems. The acceleration and displacement responses of the SDOF system are shown in Figures 21 and 22, respectively.

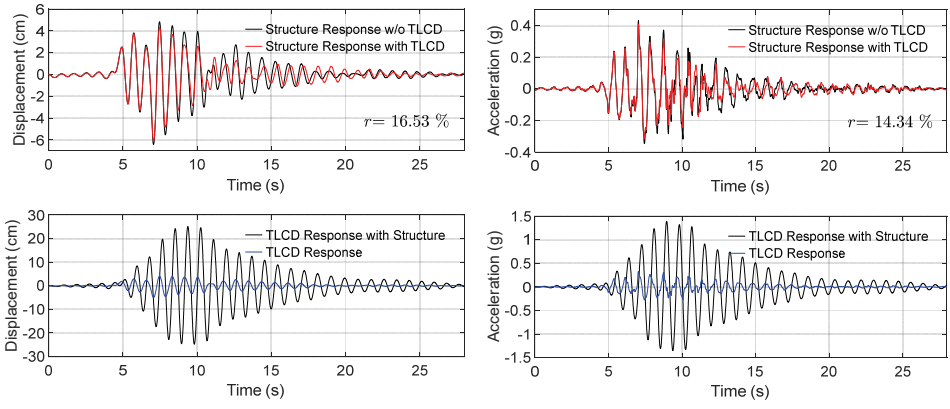

(a) (b)

Figure 21 - Time history curves for OE: (a) displacement response of SDOF system and TLCD, (b) acceleration response of SDOF system and TLCD

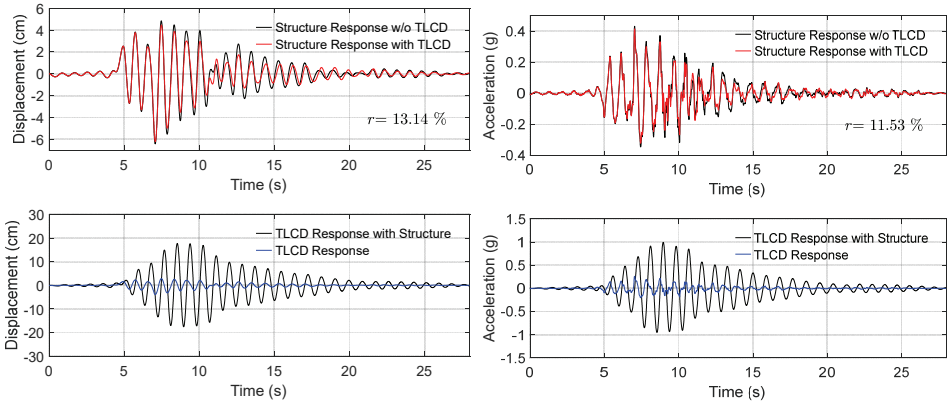

(a) (b)

Figure 22 - Time history curves for CE: (a) displacement response of SDOF system and TLCD, (b) acceleration response of SDOF system and TLCD

6. CONCLUSIONS

The dynamic characteristics and damping ratio of TLCDs with two different elbow forms with the same theoretical frequencies are investigated experimentally. The following findings are obtained by comparing the empirical and theoretical results for each mass ratio.

- Passive dampers are widely recognized for their ease of installation and ability to counteract vibrations caused by wind and strong ground motions without relying on active control. Therefore, additional damping may be required to avoid the dynamic effects of these external excitations. This study shows that additional damping can be provided to the structure by modifying the elbow shape of the TLCD without changing its dimensions, which does not require additional space.
- Empirical results indicated a decreasing trend in resonance amplitude as the mass ratio increased, while the response curves showed nonlinear behavior.
- As a result of the harmonic excitations, the maximum difference between the theoretical and experimental natural frequencies was obtained for each mass ratio when the harmonic excitation amplitude was ±10 mm. This value reached 4.624% for CE and 3.810% for OE TLCD designs.
- In the experiments performed for the harmonic excitation amplitude of ±5 mm, the maximum difference between the experimental and theoretical frequencies reached 2.612% and 2.530% for the CE and OE, respectively.
- It is inferred that the difference between the theoretical and experimental frequencies is due to the surface friction of the fluid in the TLCD. However, considering that the differences from the experimental results are within 5%, it can be interpreted that the results are in an acceptable range.
- Experimental natural frequencies obtained for OE and CE TLCD configurations with equal theoretical frequencies show that the largest difference between OE and CE TLCDs was 5.26% under ±5 mm harmonic excitation at a mass ratio of 1.20%. For ±10 mm harmonic excitation, the difference was 1.85% for a mass ratio of 0.90%.
- This study has experimentally demonstrated that the head loss coefficient depends not only on the opening ratio of the orifice but also on the form of the elbow, considering two types of TLCD designs with OE and CE forms.
- It was found that the elbow form significantly affects the damping ratio of the TLCD system when the same mass ratios are considered. It can be concluded that the damping performance of the TLCD with CE form is superior to that of the OE. This result is also related to the harmonic excitation amplitude. In the design of the TLCD, the excitation amplitude should also be considered an important parameter.
- Considering the earthquake performance of TLCD through the numerical analysis results, OE shows superiority over the CE. The comparison of the damping performance on acceleration and displacement time histories using RMS ratios shows that OE has an advantage of approximately 25% over CE.
- The equivalent damping proposed by Park et al. [20] has been compared with experimental results, revealing discrepancies. Adjustments to the motion equations have

been made using modification factors based on experimentally obtained damping ratios, aiming to minimize the difference between experimental and numerical results. Obtained MFs are valid for the length ratios of between 0.34 and 0.6.

- In this study, the control performance of TLCD is investigated by considering the elbow form, and adjusted numerical analyses are performed. Future studies are suggested to investigate the optimal elbow forms.

Symbols

A : Cross-sectional area of the TLCD

B : Effective horizontal length of the TLCD system

c_{eq} : The equivalent damping coefficient

C_s : Damping coefficient of SDOF system

g : Acceleration of gravity

L : Total length of liquid in the TLCD

L_1 : Out-to-outer length of the TLCD system

K_s : Stiffness of SDOF system

m_d : Liquid mass in the TLCD system

m_h : Mass of liquid in the horizontal column of the TLCD

m_s : Mass of structural model

M_s : Mass of SDOF system

RMS_{WOT} : RMS value of SDOF system without TLCD

RMS_{WT} : RMS value of SDOF system with TLCD

r : RMS ratio

t : Time

x : Displacement response of SDOF system

$\dot{x}$: Velocity response of SDOF system

$\ddot{x}$: Acceleration response of SDOF system

$\ddot{x}_g$: Ground acceleration

x_r : Amplitude of the resonance frequency

y : Displacement response of the fluid in the TLCD

$\dot{y}$: Velocity response of the liquid in the TLCD

$\ddot{y}$: Acceleration response of the fluid in the TLCD

α : Mass modification factor for liquid in the TLCD

β : Stiffness modification factor for the TLCD

ε : Error between the nonlinear system and equivalent linear system

ζ : Damping ratio

μ : Mass ratio

ξ : Head loss coefficient

ρ : Density of the liquid

$\sigma_{\dot{y}}$: Standard deviation of the water surface velocity of water column $\dot{y}$

χ : Tuning ratio

ω : Excitation frequency

ω_d : Angular frequency of TLCD

ω_s : Angular frequency of structure model

References

[1] Sakai, F., Takaeda, S., Tamaki, T., Tuned liquid column damper new type device for suppression of building vibration, Proc. Int. Con. on High-rise Buildings, Nanjing, China, 1989, 926-931, 1989.

[2] Kwok, K.C.S., Samali, B., Xu, Y.L., Control of wind induced vibration of tall structures by optimised tuned liquid column dampers, Proc. Asia-Pacific Conf. On Computational Mechanics, Hong Kong, 569-574, 1991.

[3] Samali, B., Kwok, K.C.S., Young, G., Xu, Y. L., Effectiveness of optimised tuned liquid column dampers in controlling vibration of tall buildings subject to strong ground motions, Proc. 2nd Int. Conf on Highrise Buildings, Nanjing, China, 402 -407, 1992.

[4] Samali, B, Kwok, K.C.S., Parsanejad, S., Xu, Y.L., Vibration control of buildings by tuned liquid column dampers, Proc. 2nd hzt. Conf on Highrise Buildings, Nanjing, China, 425-430, 1992.

[5] Xu, Y.L., Samali, B., Kwok, K.C.S., Control of along-wind response of structures by mass and liquid dampers, Journal of Engineering Mechanics- ASCE, 118 (1), 20-39, 1992.

[6] Xu, Y.L., Kwok, K.C.S., Samali, B., The effect of tuned mass dampers and liquid dampers on cross-wind response of tall/slender structures, Journal of Wind Engineering and Industrial Aerodynamics, 10, 33-54, 1992.

[7] Aydın, E., Öztürk, Kebeli, Bati, M., Kavaz, Y., Kilic, B., Effects of Tuned Liquid Column Damper Properties on The Dynamic Response of Structures, ASCE-EMI 2019 International Conference, 2019.

[8] Gao, H., Kwok, K.C.S., Samali, B., Optimization of tuned liquid column dampers. Engineering Structures, 19(6), 476–86, 1997.

[9] Yalla, S.K., Kareem, A., Optimum absorber parameters for tuned liquid column dampers, Journal of Structural Engineering, 126(8), 906–15, 2000.

[10] Wu, J.C., Chang C.H., Lin, Y.Y., Optimal design of non-uniform tuned liquid column dampers in horizontal motion, Journal of Sound and Vibration, 326, 104–22, 2009.

[11] Shum, K.M., Closed form optimal solution of a tuned liquid column damper for suppressing harmonic vibration of structures, Engineering Structures, 31, 84–92, 2009.

[12] Hochrainer, M.J., Ziegler, F., Control of tall building vibrations by sealed tuned liquid column dampers, Structural Control Health Monitoring, 13, 980–1002, 2006.

[13] Balendra, T., Wang, C.M., Cheong H.G., Effectiveness of tuned liquid column dampers for vibration control of towers, Engineering Structures, 17(9), 668-678, 1995.

[14] Min, K.W., Kim H.S, Lee S.H, Kim H., Ahn S.K., Performance evaluation of tuned liquid column dampers for response control of a 76-story benchmark building, Engineering Structures, 27, 1101-1112, 2005.

[15] Bigdeli, Y., Kim, D., Damping Effects of the Passive Control Devices on Structural Vibration Control: TMD, TLC and TLCD for Varying Total Masses, KSCE journal of Engineering, 20, 301-308, 2016.

[16] Balendra, T., Wang, C.M., Rakesh, G., Vibration control of various types of buildings using TLCD, Journal of Wind Engineering and Industrial Aerodynamics, 83, 197–208, 1999.

[17] Sadek, F., Mohraz B., Lew, H.S., Single- and multiple-tuned liquid column dampers for seismic applications, Earthquake Engineering and Structural Dynamics, 27, 439– 63, 1998.

[18] Gao, H., Kwok, K.S.C., Samali, B., Characteristics of multiple tuned liquid column dampers in suppressing structural vibration, Engineering Structures, 21, 316–331, 1999.

[19] Hitchcock, P.A., Glanville, M.J., Kwok, K.C.S., Watkins, R.D., Samali, B., Damping properties and wind-induced response of a steel frame tower fitted with liquid column vibration absorbers, Journal of Wind Engineering and Industrial Aerodynamics, 83,183-196, 1999.

[20] Park, B.J., Lee, Y.J., Park, M.J., Ju, Y.K., Vibration control of a structure by a tuned liquid column damper with embossments, Engineering Structures, 168 290–299, 2018.

[21] Gur, S., Roy K., Mishra, S.K., Tuned liquid column ball damper for seismic vibration control, Structural Control and Health Monitoring, 22, 1325–1342, 2015.

[22] Lee, S.K., Min, K.W., Lee, H.R., Parameter identification of new bidirectional tuned liquid column and sloshing dampers, Journal of Sound and Vibration, 330 (7), 1312-1327, 2011.

[23] Lee, H.R., Min, K.W., Reducing Acceleration Response of a SDOF Structure with a Bi-Directional Liquid Damper, Procedia Engineering, 14, 1237-1244, 2011.

[24] Matteo, A.D., Iacono, F.L., Navarra, G., Pirrotta, A., Direct evaluation of the equivalent linear damping for TLCD systems in random vibration for pre-design purposes, International Journal of Non-linear Mechanics, 63, 19-30, 2014.

[25] Matteo, A.D., Iacono, F.L., Navarra, G., Pirrotta, A., Experimental validation of a direct pre-design formula for TLCD, Engineering Structures, 75, 528-538, 2014.

[26] Hitchcock, P.A., Kwok, K.C.S., Watkins, R.D., Samali, B., Characteristics of liquid column vibration absorbers (LCVA)-I, Engineering Structures, 19 (2), 126-134, 1997.

[27] Balendra, T., Wang, C.M., Rakesh, G., Effectiveness of TLCD on various structural systems, Engineering Structures, 21, 91–305, 1999.

[28] Chang, C.C., Hsu C.T., Control performance of liquid column vibration absorbers, Engineering Structure*s*, 20 (7), 580-586, 1998.

[29] Damcı, E., Şekerci, Ç., Development of a Low-Cost Single-Axis Shake Table Based on Arduino, Experimental Techniques, 43, 179-198, 2019.

[30] Chopra. A. K., Dynamics of structures: theory and applications to earthquake engineering, 4th Edition, Pearson Education, USA, ISBN: 978-0-13-285803-8, 2011.

[31] Wu, J.C., Shih, M.H., Lin, Y.Y., Shen, YC., Design Guidelines for tuned liquid column damper for structure responding to wind, Engineering Structures, 27, 1893-1905, 2005.

[32] Aydın, E., Öztürk, Kebeli, Y.E., Gültepe, G., An Experimental Study on the Effects of Different Pendulum Damper Designs on Structural Behavior, 17th World Conference on Seismic Isolation, 2022.

[33] Sarkar, A., Gudmestad, O.T., Pendulum type column damper (PLCD) for controlling vibrations of a structure – Theoretical and experimental study, Engineering Structures, 49, 221-233, 2013.

[34] Aydın, E., Öztürk, B., Dutkiewicz, M., Çetin, H., Okkay, O., Ohancan, U., Şirin, Y.E., Experiments of tuned liquid damper (TLD) on the reduced shear frame model under harmonic loads, EPJ Web of Conference, 143, 02001, 2017.

[35] Zhang, Z., Numerical and experimental investigations of the sloshing modal properties of sloped-bottom tuned liquid dampers for structural vibration control, Engineering Structures, 204, 2020.

[36] Ashasi-Sorkhabi, A., Malekghasemi, H., Ghaemmaghami, A., Mercan, O., Experimental investigations of tuned liquid damper-structure interactions in resonance considering multiple parameters, Journal of Sound and Vibration, 388, 141-153, 2017.

[37] Wen, Y.K., Design Equivalent Linearization for Hysteretic Systems Under Random Excitation, Journal of Applied Mechanics, 47(1), 150-4, 1980.

[38] PEER Ground Motion Database - PEER Center. http://ngawest2.berkeley.edu/ (Accessed, 9th May 2024).

Turkish Journal of Civil Engineering, 2024, 107-137, Paper 790, ***Research Article***

Performance Investigation of Diatomite Modified Asphalt Mixtures for Different Diatomite Ratios and Grinding Sizes

Mustafa Taha ASLAN[1*]
Erol İSKENDER[2]
Atakan AKSOY[3]

ABSTRACT

Modification of asphalt mixtures has become almost mandatory today due to increased stresses in pavements, shortening of load cycle times, and decreases in binder quality. For this reason, many additives can be added to bitumen or asphalt mixture. Industrial material wastes can also be among these additives. When diatomite material is used as a performance enhancer in asphalt mixtures, it significantly improves the main performance indicators of the asphalt mixture. However, low temperature cracking of diatomite-modified asphalt mixtures is still controversial in the literature. This study evaluated the asphalt mixture in terms of low-temperature cracking, water damage, and rutting, depending on the diatomite grinding size (gradation) and addition ratio. Three different sizes of diatomite additives (106, 212 and 300-micron maximum diameter) were used at three addition ratios (5, 10 and 15% by weight of bitumen). According to the test results, it was seen that the mechanical properties of asphalt mixtures were significantly affected by the addition ratios and diatomite sizes, and the use of 300-micron maximum diameter diatomite at the rate of 10% and 15% was more effective. However, according to the BBR test results, the use of diatomite additives with a maximum size of 106 μm at 5% slightly increased the low temperature cracking resistance.

Keywords: Asphalt mixture, diatomite, grinding size, cracking, low temperature cracking.

Note:
- This paper was received on November 9, 2023 and accepted for publication by the Editorial Board on July 11, 2024.
- Discussions on this paper will be accepted by January 31, 2025.
- https://doi.org/10.18400/tjce.1387917

1 Karadeniz Technical University, Faculty of Technology, Dep. of Civil Engineering, Trabzon, Türkiye
aslanmustafataha@gmail.com - http://orcid.org/0000-0002-0453-788X

2 Karadeniz Technical University, Faculty of Technology, Dep. of Civil Engineering, Trabzon, Türkiye
eiskender@ktu.edu.tr - http://orcid.org/0000-0001-7934-839X

3 Karadeniz Technical University, Department of Civil Engineering, Trabzon, Türkiye
aaksoy@ktu.edu.tr - http://orcid.org/0000-0001-5232-6465

* Corresponding author

1. INTRODUCTION

Diatomite is a mineral that is a low-cost mineral, easy to produce, and does not cause environmental pollution. The European region is very rich in diatomite reserves. Turkey is the country with the highest diatomite reserves after America and China. The diatomite reserves in the United States, China and Turkey represented around 250, 150 and 44 million metric tons, respectively, in 2022 [1].

The distinctive characteristics of diatomite have resulted in its adoption in various industrial uses, with the primary applications encompassing liquid filtration and serving as a bulking agent, as seen in the context of paint production. Additionally, diatomite finds utility in insulation, particularly in the production of fire-resistant bricks, as well as in fine abrasion applications, such as toothpaste and various polishing products. Furthermore, it is employed as an effective pesticide in certain scenarios [2].

One of the applications of diatomite is in the asphalt pavement industry. Incorporating diatomite into asphalt can have multiple advantages. This method can utilize natural resources to their fullest potential and enhance the asphalt's overall performance. Additionally, preparing a diatomite-modified asphalt mixture is a straightforward process that doesn't require any specialized equipment. Moreover, the construction process for this type of pavement is identical to that of regular asphalt, making it an economically feasible option [3].

Relevant research has indicated that the incorporation of diatomite can greatly enhance the resistance of bitumen to high-temperature rutting and thermal oxidative aging [4,5]. Furthermore, it is stated that diatomite exhibits superior performance compared to hydrated lime and fly ash in enhancing asphalt mixture properties [6–9]. The improvement of asphalt performance through diatomite is primarily attributed to physical adsorption, as the exceptional adsorption capacity of diatomite effectively inhibits the thermal and oxidative aging of asphalt binders [10]. Diatomite effectively adsorbs low molecular weight compounds and low polarity aromatic molecules in bitumen, while exhibiting limited adsorption capacity towards asphaltene and resin [11]. Diatomite possesses robust adsorption and hardening characteristics on bitumen leading to significant enhancement in bonding performance, strength, stiffness, and anti-aging properties of asphalt mixtures [12].

In research conducted on diatomite-modified asphalt mixtures, emphasis has been placed on the high-performance characteristics of the modified mixtures. The study showed that diatomite outperformed higher performance than kaolin, Na-bentonite, and Ca-bentonite in view of the high-temperature performance, low-temperature performance, and temperature sensitivity of asphalt mixtures [13]. Also, diatomite-modified asphalt mortar exhibited excellent rutting and water damage resistance [14,15]. In another study, it was stated that diatomite had the potential to enhance the water damage resistance of asphalt mixtures based on freeze-thaw splitting tests [16]. Diatomite possessed strong adsorption capacity, which reduced the contact and binding opportunities of water with aggregates, consequently improving the water stability of asphalt mixtures [3]. The impact of diatomite on the low-temperature performance of asphalt mixtures using various testing methods was studied and it was concluded that diatomite-modified asphalt mixtures exhibited better low-temperature performance compared to matrix asphalt mixtures [17]. In another investigation, it was highlighted that the addition of diatomite improved the crack resistance and fatigue properties of asphalt mixtures based on beam bending tests and four-point bending fatigue tests [18].

Diatomite can be used in combination with other additives, fibers, or fillers to improve the final mechanical properties, aging properties, and anti-icing performance of the asphalt mixture [7, 19-24]. It is understood from the literature that the general performance of diatomite-modified asphalt mixtures is high. Therefore, diatomite has the potential to be used as an additive in asphalt mixtures. However, some studies have observed that diatomite modification reduces the asphalt mixture's fatigue performance [25] and low-temperature cracking resistance [17]. Some studies have stated that the diatomite additive is almost ineffective in terms of low-temperature cracking [4].

In a study by Wang et al., a clean asphalt production method was investigated to reduce the damage to the environment and human body. In this context, diatomite and modified-attapulgite were multi-modified. The results of the BBR test on asphalt mixtures proved that the additives slightly reduced the low temperature properties of asphalt pavements [26].

In a study, it was found that rubber and diatomite modification of asphalt mixtures can improve the high temperature stability and low temperature cracking resistance of asphalt mixtures, but especially the effect of improving the low temperature cracking resistance is weaker than that of SBS modified ones. This was attributed to the fact that rubber and diatomite particles mainly form a physical bond in asphalt mixtures and the effects of this bond are weaker than the chemical modification of SBS [27].

In a study where basalt fiber was used to overcome the inadequacies of diatomite modified asphalt mixtures in low temperature performances, in addition to the control (unmodified) mixture, the mixture modified with diatomite at 15% of the asphalt binder ratio; asphalt mixture modified with basalt fiber additive at the rate of 0.3% of the mixture weight by dry method; diatomite modified with 15% of the bitumen by wet method and basalt fiber modified with 0.3% of the asphalt mixture by dry method. To mix diatomite into bitumen, the bitumen was heated at 135°C for 4 hours and then mixed in a high-speed mixer for 15 minutes. Basalt fiber was added to the heated aggregate and mixed for 5 minutes. Diatomite-modified bitumen was added to the basalt aggregate mixture and mixed thoroughly. The asphalt mixture samples were subjected to low temperature cracking test at -5°C and 4-point beam bending test at 20°C. The results showed that the combination of diatomite and basalt fiber compensated well for the vulnerability of asphalt mixtures to low temperatures [24].

In a study by Li et al., surface modified diatomite and bio-oil were used at 0, 5, 10, 15% by mass of bitumen and the modification processes were carried out with a high-speed mixer at 155°C at a shearing speed of 4500 rpm for 60 minutes. As a result of the BBR test, it was observed that hybrid modification can improve the low temperature behaviour of asphalt mixtures [28].

In a study carried out by Aksoy et al., it was aimed to find the optimum ratios of diatomite filler additive, which is extracted as waste for a sustainable future and the environment, that could potentially be used in asphalt plants, and therefore modification processes were carried out at different ratios. Asphalt mixtures were modified by wet method. Diatomite additives were used at 5% and 10% by weight of bitumen. Asphalt mixture samples were evaluated in terms of rutting resistance by repeated load creep test and the highest rutting resistance was obtained with 5% diatomite ratio in unconditioned samples and 10% diatomite ratio in conditioned samples [29].

The main uses of diatomite additives were summarised above, and it was observed that diatomite modified asphalt mixtures were effective in terms of high temperature, rutting and

water damage resistance, but ineffective in terms of low temperature cracking resistance. The reason for this weakness of diatomite modified asphalt pavements in low temperature performance is thought to be the physical bonding of diatomite with the asphalt mixture. It was observed that the use of diatomite-basalt fiber increased the resistance of the asphalt mixture to low temperature cracking. As seen in the literature research, it is important to determine the optimum diatomite ratio. In addition, no study investigating the size effect using diatomite at different grinding sizes has been found in the literature and it is thought that the size effect of diatomite additives used in this study will contribute to the literature.

1.1. Objectives and Scope

More current and precise information is needed on the effects of diatomite modification on low-temperature cracking. The overall performance of diatomite-modified asphalts depends on many factors such as the type of diatomite used, mixing ratio, other additives and conditions of use. The potential of diatomite modification to improve the performance of asphalt mixtures has been demonstrated in many studies. However, these studies generally did not distinguish between different types of diatomite or focused on a limited number of properties. This deficiency raises the possibility that different diatomite types or gradations may have different effects on asphalt mixture performance. The main purpose of this study is to evaluate the effects of grinding size and addition ratio of diatomite on asphalt mixture performance. For this purpose, diatomite additives obtained in three different grinding sizes were added to bitumen at three different addition ratios and the asphalt mixture samples produced were evaluated by repeated creep test, water damage test and indirect tensile test. The modified binders were evaluated by bending beam rheometer (BBR) test, penetration, and softening point tests.

2. MATERIAL AND METHOD

2.1. Material

The study used 50-70 penetration grade asphalt cement, whose properties are shown in Table 1, and limestone aggregate in Table 2. According to the Turkish Highways Technical Specification [30], aggregate gradation suitable to produce dense-graded asphalt concrete was determined. Aggregate gradation curve is given in Figure 1.

Table 1 - Pure bitumen properties

Test	Test method	Result	Specification limits
Specific gravity (25°C)	ASTM D70	1.011	
Softening point (°C)	TS EN 1427	52	46-54
Flash point (°C)	TS EN ISO 2592	240	≥ 230
Penetration (25°C) 0.1mm	TS EN 1426	63	50-70
Ductility (25°C)	ASTM D-113	100+ (cm)	
Solubility (%)	TS EN 12592	99.8	≥ 99

Table 2 - Limestone Aggregate Properties

Aggregate properties	Test method	Result	Specification limit
Specific gravity (coarse aggregate)	ASTM C 127		
Bulk		2.707	
Apparent		2.733	
Specific gravity (fine aggregate)	ASTM C 128		
Bulk		2.763	
Apparent		2.776	
Los Angeles abrasion (%)	TS EN 1097-2	26.70	≤27
Water absorption (%)	TS EN 1097-6	0.90	≤2
Soundness (MgSO4) (%)	TS EN 1367-2	2.4	≤16
Flakiness (%)	BS 812	9.71	≤25
Stripping resistance (no additive) (%)	TS EN 12697-11	60-65	≥60
Plasticity index for sandy aggregate	TS-1900-1	NP	NP
Organic matter for sandy aggregate	TS EN 1744-1	Negative	Negative

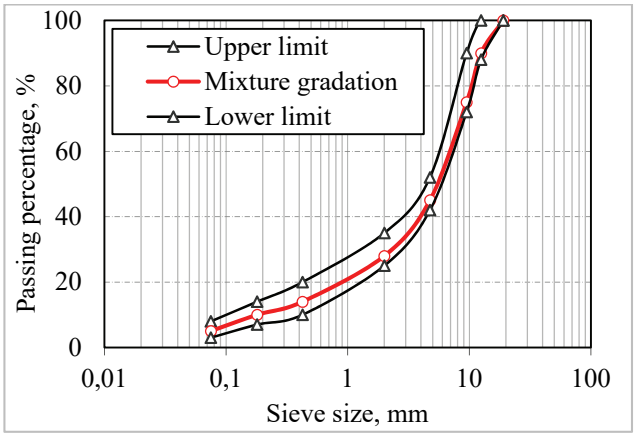

Figure 1 - Aggregate gradation curve

Three diatomite additives obtained from Bentaş Bentonit Mining Industry and Trade Joint Stock Company and coded as D1 (First type diatomite), D2 (Second type diatomite), and D3 (Third type diatomite) were used in the study. Properties of agents were given in section 2.2.2 in detail.

2.2. Method

2.2.1. Preparation of Diatomite Modified Bitumen

Direct and indirect (wet) methods can be used to prepare the diatomite-modified asphalt mixture. When the direct blending method is used, diatomite is added to the asphalt and aggregate mixture as mineral powder. When the indirect method is used, diatomite-modified asphalt binder is prepared before preparing the mixture [31]. It is stated that the two blending methods lead to approximately the same blending effect [32]. The wet method was used in this study. Diatomite additives were added to the bitumen at the rates of 5%, 10%, and 15% by weight (according to the asphalt mixture weight, respectively: 0.243%; 0.485%; 0.728%), and asphalt mixtures were prepared with diatomite-modified bitumen.

There have been some studies which were researched the diatomite-bitumen modification; in a study, 50/70 penetration grade bitumen was used and diatomite was added to the bitumen at the rates of 5%, 10%, 15% and 20% by weight. For the preparation of diatomite modified asphalt, the shearing temperature was chosen as 150°C, the shearing speed was 3000 rpm, and the shearing time was 120 minutes for the preparation of diatomite-modified asphalt [4]. In another study, 70/100 penetration grade bitumen was used and diatomite was added to the bitumen as 0.1%, 0.2% and 0.3% according to the total asphalt mixture weight. Mixture preparation temperature was taken as 150°C, the shearing speed was 4000 rpm, and the shearing time was 40 minutes [33]. In another study, 80/100 penetration grade bitumen was used in the asphalt mixture and 14% diatomite was added to the asphalt cement. The shearing temperature was 160°C, the shearing speed was 5000 rpm, and the shearing time was 40 minutes [17].

In the current study, diatomite-modified bitumen was processed at 4000 rpm at 160 °C. It was prepared with a mixing time of 40 minutes at shear speed.

2.2.2. Chemical Properties

XRF (X-ray fluorescence) main oxide analysis results of diatomite additives are shown in Table 3. XRD (X-ray diffractometer) graphs of diatomite additives are given in Figure 2, 3, 4. EDS (Energy Dispersive Spectrometry) layered images of diatomite additives are presented in Figures 5, 6 and 7. EDS Map sum spectra of the additives are presented in Figures 8, 9 and 10; and SEM (Scanning Electron Microscopy) images are presented in Figures 11, 12 and 13. When Figures 2, 3 and 4 are analysed; it is clear that; the densest diatomite contribution in terms of minerals according to XRD results of diatomite additives is in D1 diatomite with 5000 levels. In Figure 3, it is observed that the quartz peak and anorthite peak are intense. It is also understood that the amount of paragonite is also high. It is understood that D2 diatomite has low anorthite content compared to D3 diatomite; but it is rich in Na mineral. Among the 3 samples, it is observed that the amount of quartz and anorthite in D1 is high and D1 is the richest contribution in terms of mineral. As the maximum grain size decreased, different residual phases in the samples appeared. The SEM/EDS data showed that the elements distribution in D1, D2, D3 are mostly rich in terms of C, O, Si however the Fe, Ca, K, Mg contents showed differences on the diatomite samples due to the particle size difference. The overall contents of element distribution can be estimated by D1, which has a finest particle size with 1.5wt% Mg, 3.8wt% Al, 1.0wt% Ca and 1.4 wt% Fe. The surface of all samples has a non-uniform microstructure with voids and pores. The density of the D1 surface is higher than the other samples since the particle size of D3 is the lowest.

Table 3 - Main oxide analysis results of diatomite additives

	Unit	D1	D2	D3
SiO_2	%	73.955	74.099	74.199
Al_2O_3	%	8.989	8.437	8.832
Fe_2O_3	%	2.899	2.839	3.032
MgO	%	2.485	3.049	2.649
CaO	%	2.270	1.852	2.434
Na_2O	%	0.207	0.109	0.164
K_2O	%	1.256	1.002	1.274
TiO_2	%	0.511	0.460	0.518
P_2O_5	PPM	0.206	0.139	0.199
MnO	%	0.102	0.054	0.149
SO_3	%	0.014	0.016	0.018
Cl	PPM	94	83	-
BaO	%	0.032	0.017	0.041
CuO	%	0.194	0.319	0.294
NiO	%	0.227	-	0.009
SrO	%	0.038	0.029	0.046
V_2O_5	%	0.0739	0.077	0.072
ZnO	%	-	-	0.008
ZrO_2	%	0.028	0.018	0.033

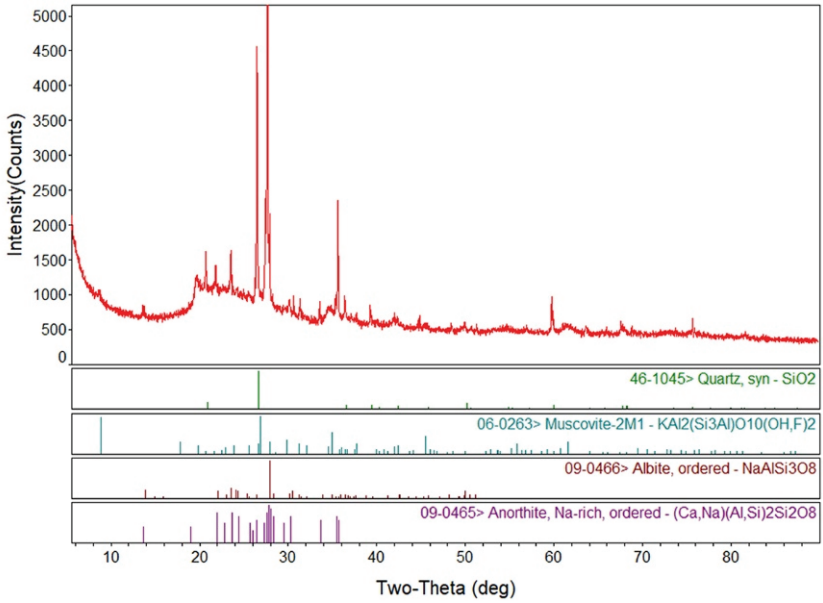

Figure 2 - XRD test result of D1 diatomite

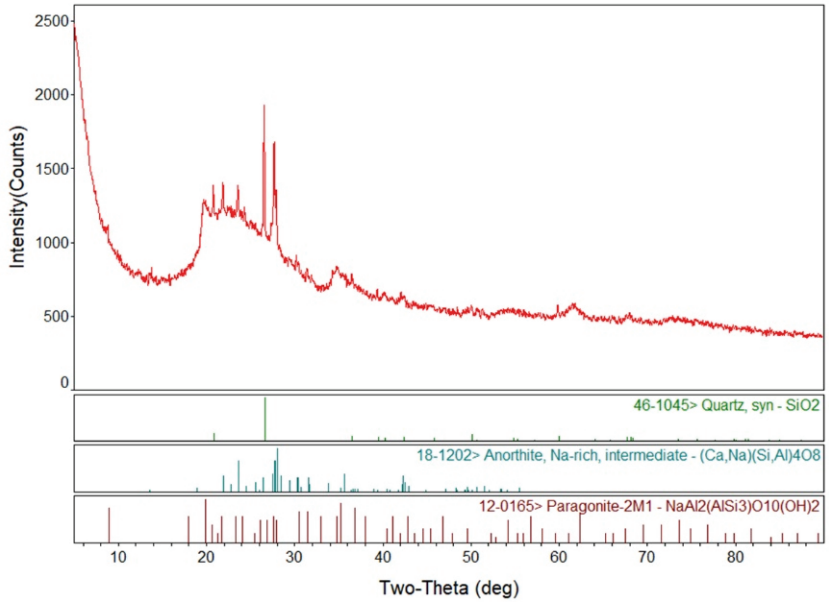

Figure 3 - XRD test result of D2 diatomite

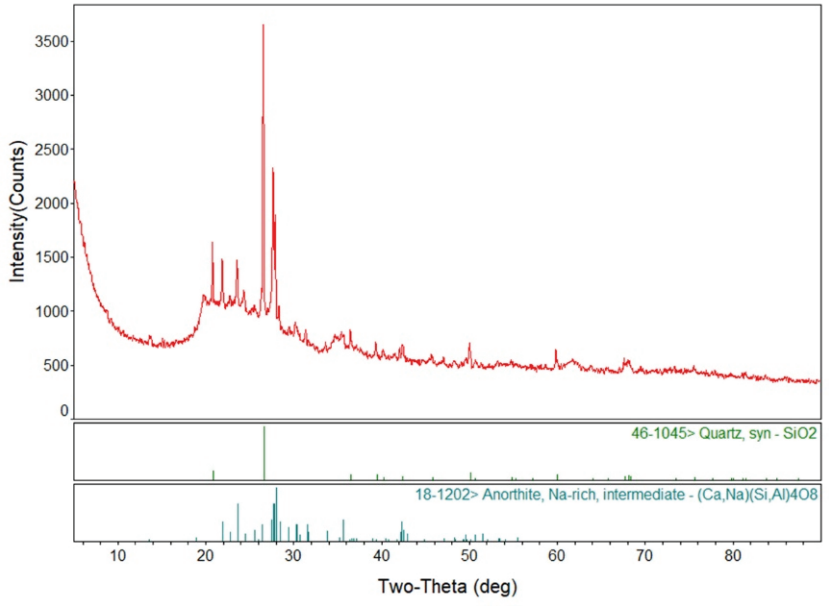

Figure 4 - XRD test result of D3 diatomite

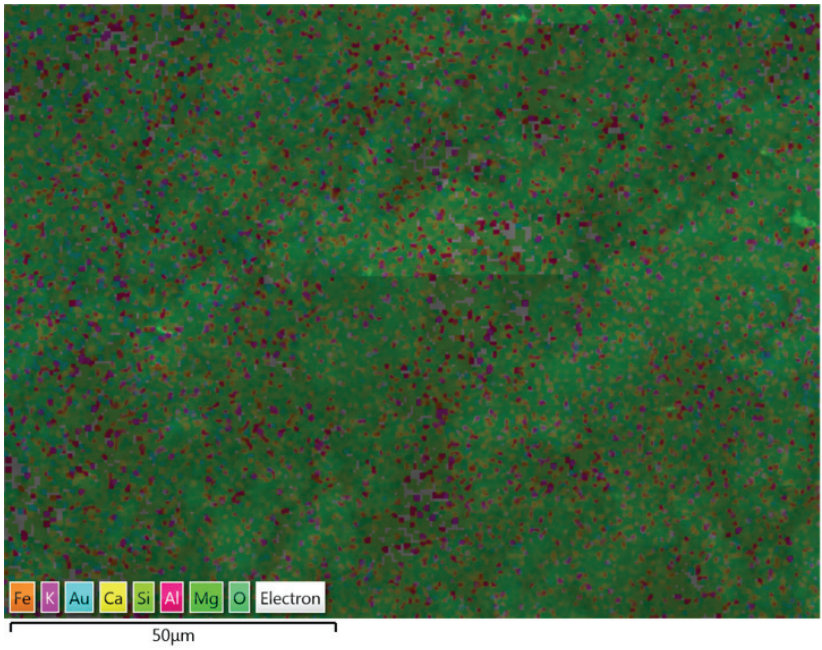

Figure 5 - EDS layered image of D1 diatomite

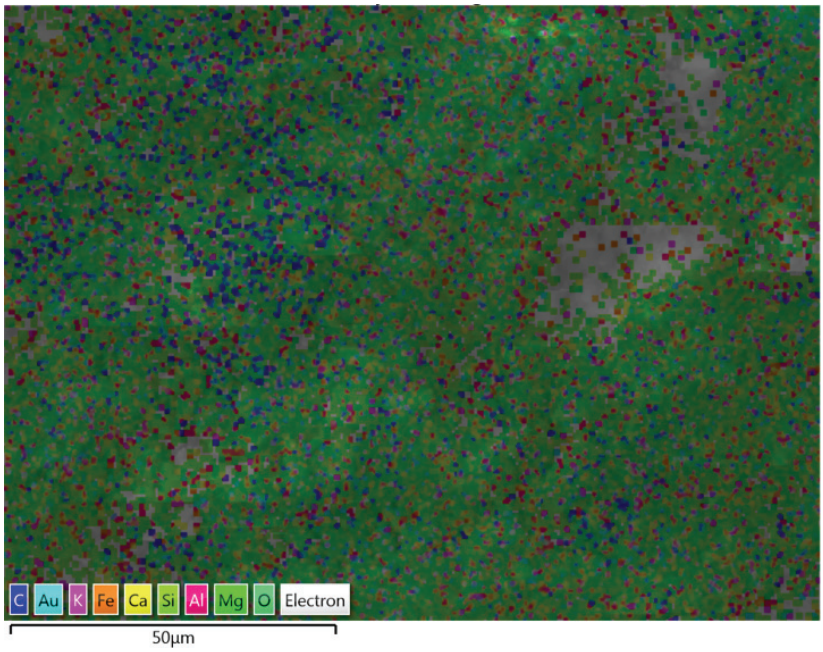

Figure 6 - EDS layered image of D2 diatomite

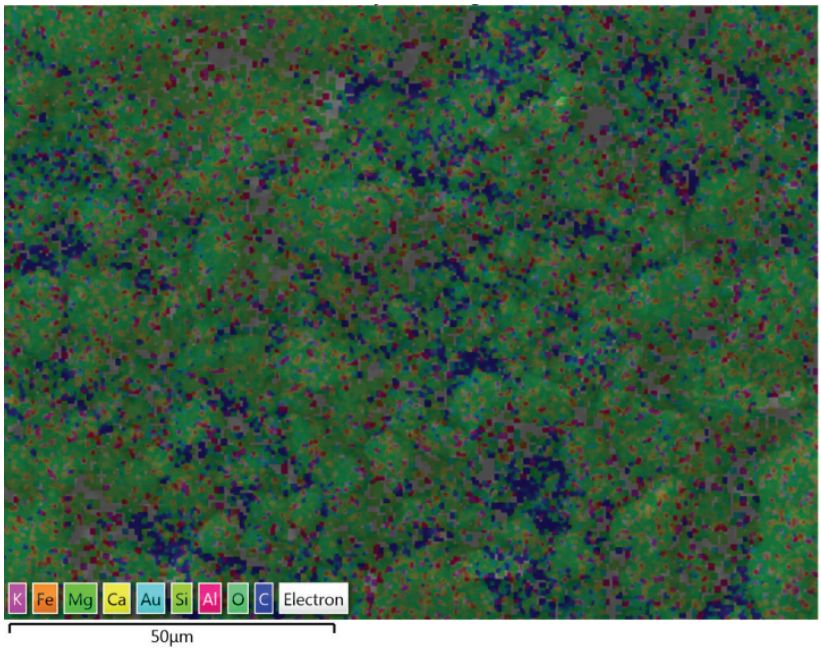

Figure 7 - EDS layered image of D3 diatomite

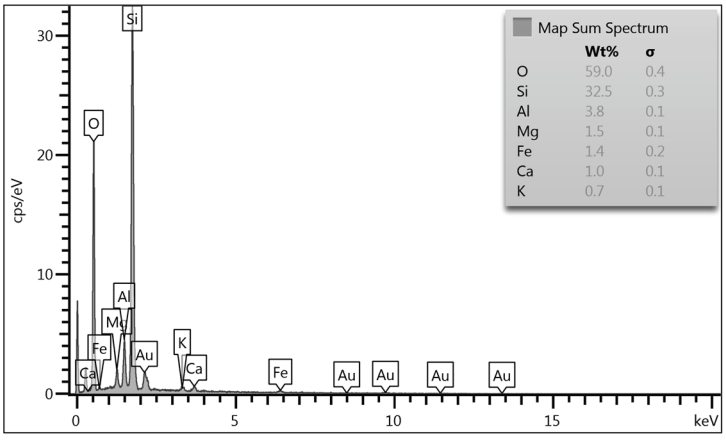

Figure 8 - EDS map sum spectrum of D1 diatomite

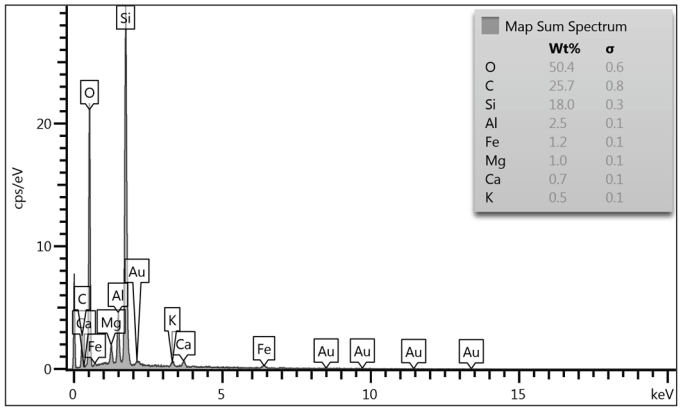

Figure 9 - EDS map sum spectrum of D2 diatomite

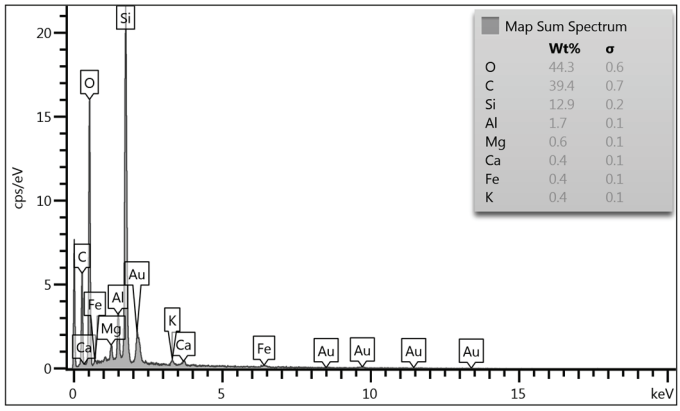

Figure 10 - EDS map sum spectrum of D3 diatomite

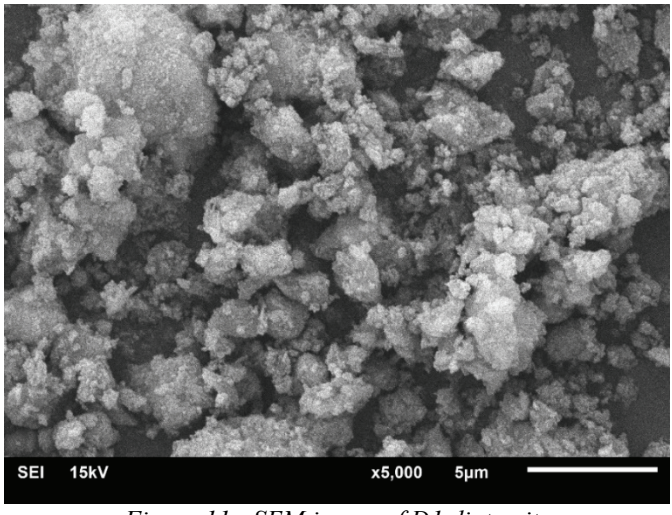

Figure 11 - SEM image of D1 diatomite

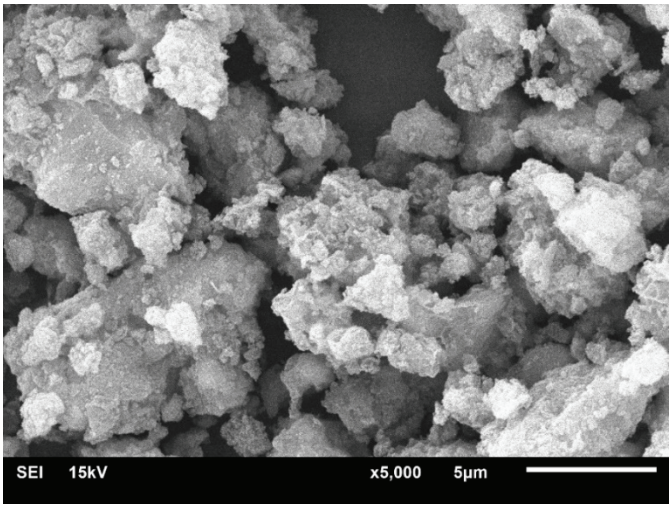

Figure 12 - SEM image of D2 diatomite

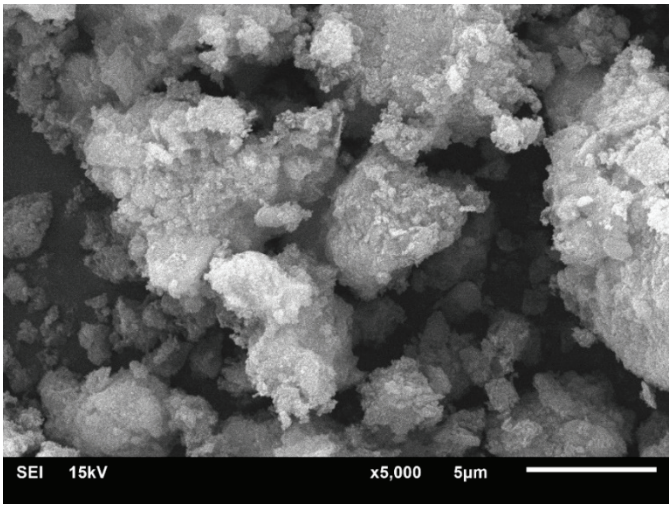

Figure 13 - SEM image of D3 diatomite

2.2.3. Mix Design Properties

Gradation analysis results of diatomite additives are shown in Table 4. From Table 4, it can be seen that D1 diatomite is in the finest gradation and D3 diatomite is in the coarsest gradation. 50% of D1, D2 and D3 diatomite are thinner than 9.46 microns, 111.35 microns, and 190 microns, respectively. At the same time, the maximum diatomite size is also in the same order. The low-temperature tensile strengths of D1-modified asphalt mixtures were lower than those of D2 and D3 diatomite used at the same inclusion rates. The higher surface area of D1 diatomite may have increased the stiffness of the mixture by absorbing more

asphalt cement. This may have had a negative impact on the low temperature strength of asphalt mixtures. The higher tensile strength of D2 and D3 diatomite confirms this idea.

In accordance with the Highway Technical Specification [30], the dense graded asphalt mixture design was made with pure bitumen according to the Marshall method. The bitumen content giving 4% air void was taken as the optimum bitumen content and calculated as 5.10%. It was observed that other mixture properties also met the specification limits in the calculated bitumen content (Table 5). Control mixtures and diatomite-modified mixtures were produced at the calculated bitumen content.

Control and diatomite-modified asphalt mixtures were investigated for low-temperature cracking, water damage, and rutting problems. Conditioned and unconditioned samples were used in the experimental processes.

Table 4 - Gradation analysis results of diatomite additives

D1 diatomite additive material		D2 diatomite additive material		D3 diatomite additive material	
Sieve size, µm	Gradation, (% Passing)	Sieve size, µm	Gradation, (%Passing)	Sieve size, µm	Gradation, (%Passing)
106	100	212	100	300	100
80	98.4	150	99.1	212	68.2
60	97.1	106	95.1	206	54.6
40	94.3	80	88.4	150	52.1
30	90	60	79.6	106	44.5
20	85.4	40	68.8	80	31.4
10	76.2	30	51.9	60	23.0
5	52.2	20	42.1	40	17.2
2	25.1	10	30.9	30	12.6
2	4.7	5	18.7	20	11.1
		2	10.1	10	9.2
		2	2.9	5	6.6
				2	3.7
				2	1.9

Asphalt mix design was made according to 4% air voids and the suitability of parameters such as VMA and VFA was checked. The air voids of the asphalt mix briquettes produced for the experimental studies were calculated by density measurements and given in Table 6 as the average of 15 samples. The air voids of diatomite modified asphalt mixtures increased by 0.07% - 0.13% compared to control mixtures. However, the air voids of diatomite modified asphalt mixtures varied slightly among themselves.

Table 5 - Asphalt concrete design results

Design parameters	Specification limits	Mixture values
Number of blows per face	75	75.00
Density, gr/cm3		2.44
Marshall stability, kg	Least 900	1189
Air voids, V_h, %	3-5	4.00
Voids filled with asphalt, $V_{f,}$ %	65-75	71.64
Flow, mm	2-4	3.48
Bitumen content, %	4-7	5.10
VMA (Voids in Mineral aggregate), %	14-16	14.37

Table 6 - Air void ratios of asphalt mixture briquettes

Mixture	Control	D1			D2			D3		
		5%	10%	15%	5%	10%	15%	5%	10%	15%
Air voids (%)	3.99	4.08	4.10	4.12	4.07	4.07	4.11	4.06	4.09	4.11

2.2.4. Penetration and Softening Point Tests

Penetration test determines the consistency of asphalt as well as the class of solid asphalt. As penetration increases, adhesion increases, viscosity and solidity decrease. Asphalt cement is semi-solid at room temperature. It is not possible to predict viscosity at high viscosities. However, the binding ability of asphalt on the road surface depends on the consistency. As the consistency of the asphalt cement increases, the aggregates in the mixture bind more strongly to each other. The penetration of bitumen is defined as the distance in 0.01 mm at which a standard needle penetrates vertically into asphalt cement for a certain time (5 s) under a certain load (100 g) at room temperature [34]. Penetration test standards of bituminous binders are determined by TS EN 1426 [35].

The sensitivity of asphalt to temperature changes can be determined most simply by the "ring and ball" method. Penetration values of some asphalt types at 25°C may be the same. However, when the temperature is increased, a difference in properties can be observed. This is determined by the softening point test. The asphalt sample is placed in a ring of standard thickness and diameter. A ball of standard diameter and weight is placed on the sample and heated rapidly in water. The temperature at which the asphalt in the ring collapses to a certain depth (when it touches the bottom) with the weight of the ball is considered as the temperature at which the asphalt softens (softening point). The softening point test of bituminous binders is determined by TS EN 1427 [36].

The penetration index (PI) is used to get an idea of the temperature sensitivity of bitumen. An increase in the penetration index indicates a decreased sensitivity of the bitumen sample to temperature. The PI value of bitumen is usually between -2 and +2. If this value is close to +2, the temperature sensitivity of bitumen is considered to be low, and if it is close to -2,

it is considered to be high [37]. Asphalt mixtures containing bitumen with higher PI have a higher resistance to low temperature cracking and permanent deformation [38]. PI is usually determined by the classical method given in Eq. 1 [39].

$$PI = \frac{1952-500\times\log(Pen25)-20\times SP}{50\times\log(Pen25)-SP-120} \quad (1)$$

where Pen25 is the penetration value of bitumen at 25°C and SP is the softening point of bitumen.

2.2.5. Bending Beam Rheometer (BBR) Test

BBR is performed on aged bitumen samples according to ASTM D6648 [40] to determine the behaviour of bitumen at low temperature. BBR simply indicates the amount of creep or deflection the binder undergoes at a given temperature and under a constant load. Asphalt becomes too hard at low temperatures to rely on the results obtained with DSR. Therefore, a bending beam rheometer has been developed to monitor asphalt at low temperatures. The test is usually carried out at sub-zero temperatures (the test criterion is usually taken as the temperature at which the stiffness of the binder is 300 MPa) and the deflection of a beam-shaped asphalt bar under constant load is monitored over time. In this test, bitumen samples aged by RTFO and PAV tests are used. Thus, the asphalt is tested after mixing and paving operations. The test is carried out under computer control and the instantaneous time-deformation and time-creep stiffness graphs are plotted by the computer to calculate the creep stiffness "S" and creep rate "m" at the end of 60 seconds [41, 34]. The deflection of a bitumen beam of a given size at a given time (t) is measured and the (t) of the bitumen is calculated from the classical beam theory using Equation (2). On the other hand, the creep rate is related to the variation of (t) with time (t). For practical reasons, the software of the BBR device establishes a logarithmic relationship between (t) and t in the form of Equation (3). The m-value, which is the slope of the graph of log (t) - log t at a given time t, can be calculated using Equation (4), which is the derivative of Equation (3) with respect to log t [42].

$$S_{(t)} = \frac{P\times L^3}{4\times b\times h^3\times\delta_{(t)}} \quad (2)$$

$$logS_{(t)} = A + Blogt + C(logt)^2 \quad (3)$$

$$m(t) = \left|\frac{d[\log S_{(t)}]}{d(logt)}\right| = B + 2C\log t \quad (4)$$

where: $S(t)$ is the flexural creep stiffness at time $t$in MPa, $m(t)$ is the creep rate at time t, P is the measured test load in mN, L is the span length in mm, h is the depth of the specimen in mm, $\delta(t)$ is the deflection of test specimen at time t, and A, B, C are regression coefficients.

In the Superpave bitumen specification, an upper limit of 300 MPa is imposed on (t) in order to keep the bitumen hardness below a certain level [43]. However, an increase in the m-value means that the hardness of the bitumen changes quite rapidly and therefore shows better stress relaxation capability [44]. Due to this fact, a lower limit of 0.300 for the m-value was

introduced in the Superpave bitumen specification to ensure that the bitumen has an adequate stress relaxation capability [43]. It is assumed that bitumen with an m-value above this limit can quickly dissipate stresses caused by thermal changes [42].

2.2.6. Conditioning Method

Performance tests of asphalt mixtures were conducted on conditioned and unconditioned-control (unmodified) and diatomite-modified asphalt mixtures. The conditioning system was applied according to the AASHTO T 283 [45] method. Three identical Marshall briquettes were used for each mixture option created according to additive type, ratio, and conditioning. According to the method, the samples are divided into two groups. While the samples in one of the groups are not conditioned, the samples in the other group are first saturated with water in the range of 70% to 80% with a vacuum pycnometer. The water saturated samples are tightly wrapped with plastic film and placed in a plastic ziplock bag containing 10±5ml water. Then the samples are kept at -18±3°C for at least 16 hours. The samples taken out of the freezer are placed in a water bath at 60±1°C for 24±1 hours without waiting. After these procedures, the samples are considered conditioned, and the plastic bag and film are removed [45].

2.2.7. Indirect tensile strength (ITS) test

The indirect tensile strength (ITS) test is among the most widely accepted tests for investigating the behaviour of asphalt mixtures at low temperature [46]. The ITS test was developed by the Strategic Highway Research Program (SHRP). Because the test is simple, can be done with inexpensive equipment, and gives essential information, it has been adopted by researchers and practitioners. With the test, creep stiffness can also be obtained besides the low-temperature resistance of asphalt mixtures. The ITS values obtained when the test was performed at low temperatures represent the low-temperature resistance of the pavement under real road conditions [47]. Samples are placed horizontally between two loading bars that can move parallel to each other in the vertical plane. While the bars compress the briquette at a constant speed of 50 mm/min, the sample cracks in the vertical plane due to the indirect tensile stresses. The largest load causing cracking is recorded in the device as tensile strength. At the same time, the deformation of the sample can be recorded until it cracks. The test can be performed at different temperatures. This study selected a temperature of 0°C, and the test was repeated with three identical samples. The failure strength (ITS) was calculated using equation (5) by using the recorded maximum load that caused crack formation in the sample during the test.

$$ITS = \frac{2000\,P}{\pi\,D\,t} \tag{5}$$

where ITS = indirect tensile strength (kPa), P = maximum load (N),t = thickness of specimen (mm), and$D$ = diameter of specimen (mm).

2.2.8. Moisture Damage Test

The weakening or breaking of the bonds between the aggregate surface and the bituminous binder due to water or moisture is called water damage or moisture susceptibility [48]. The fact that asphalt pavement is sensitive to moisture; in other words, its low water damage resistance reduces the adhesion and cohesion resistance of the pavement, may cause significant deterioration in the pavement such as stripping, ravelling, water infiltration, and may trigger other types of deterioration [49].

Moisture susceptibility of asphalt mixture samples can be evaluated with tensile strength ratio (TSR) test. TSR, determined according to the AASHTO T 283 standard, is the most accepted test method used to determine the resistance of compacted asphalt mixture samples against deterioration caused by water. The test aims to determine the indirect tensile strength of unconditioned and conditioned that have undergone a series of conditioning processes, compacted asphalt mixture samples. TSR is the ratio of ITS of conditioned and unconditioned samples and is calculated according to Equation 6 [50]. If the tensile strength ratio of the samples is 80% or more, it is resistant to moisture susceptibility [51, 52].

$$TSR = \frac{ITS_{conditioned}}{ITS_{unconditioned}} \quad (6)$$

2.2.9. Repeated Creep Test

The repeated creep test offers valuable information about the susceptibility of asphalt mixtures to rutting when changes in temperature occur [53,54]. The test system allows the simulation of application conditions by providing options such as variable temperature, stress or load, loading period, and conditioning loading. The repeated application of load to the asphalt mixture sample (loaded and unloaded periods) allows for the advantages provided by the elasticity properties of the mixture to be observed (the effect of returning deformations can also be taken into account). The loading number or cumulative deformation that ends the test can be selected. During the test, the number of loadings and the amount of deformation are automatically recorded [55].

It is recommended that the repeated creep test be performed at relatively low-stress levels (cannot usually exceed 206.9 kPa) and low temperature (cannot usually exceed 40˚C); otherwise, it is stated that the sample will fail prematurely [56].

In the research, repeated creep tests were performed on conditioned and unconditioned samples according to EN-12697-25 (A) [57] test standard. In this study, three samples from each mixture were tested. The conditioning was carried out following the AASHTO T 283 method. The tests were conducted at 40°C temperature, under the tension of 95 kPa, at a frequency of 0.5 Hz and 20000 loading cycles. In this test, the conditioning stress was 3 kPa; conditioning stress time 2 min; loading duration was 500 milliseconds and unloading duration was 500 milliseconds.

3. TEST RESULTS AND EVALUATION

3.1. Penetration and Softening Point Tests Evaluation

Table 7 shows the penetration, softening point and penetration index values on control and diatomite-modified asphalts. When all penetration values were analysed, it was observed that they were within the specification limits. It was observed that the penetration values decreased by minimum 9.36% and maximum 21.81% in diatomite modified asphalt mixtures compared to control (virgin) asphalt mixtures. It was observed that the penetration value decreased as the diatomite content increased in all diatomite modified asphalt mixtures. When the softening point values given in Table 7 are analysed, it is seen that all of the diatomite modified asphalts are higher than the control (virgin) mixtures. According to the penetration and softening point values, it was observed that the high temperature performance of diatomite modified asphalt mixtures improved due to the porous structure of diatomite. This result was confirmed in a study by Wang et al. [26], which showed that the softening point values of diatomite modified asphalt mixtures increased and penetration values decreased compared to control (virgin) asphalt mixtures. This was attributed to the decrease in the overall fluidity of the modified asphalt due to the absorption of the light components of asphalt into the porous structure of diatomite.

When the PI values in Table 7 are analysed, it is seen that the PI values of all diatomite modified asphalt mixtures are higher than the control (virgin) bitumen, therefore, the modification of diatomite additive to asphalt increases the temperature sensitivity of the mixtures. It was observed that the highest PI value and the least sensitive mixture to temperature was observed in 15% D3 mixtures with 1.681.

Table 7 - Penetration and softening point test results of control and diatomite-modified bitumen

	Control	D1			D2			D3		
		5%	10%	15%	5%	10%	15%	5%	10%	15%
Penetration 25°C, 100 g, 5 s (0.1 mm)	63.1	57.7	53.2	52.8	55.6	53.5	52.5	54	53.2	51.8
Softening point (°C)	52.4	57.1	58.6	60.2	57.7	58.7	61.2	60.4	61.5	62.9
PI	-0.043	0.796	0.902	1.207	0.828	0.937	1.390	1.306	1.483	1.681

3.2. Bending Beam Rheometer (BBR) Test Evaluation

The S value obtained by the BBR test is shown in Table 8 and the m value is shown in Table 9. When S values are analysed, it is observed that all values are within the specification limits (≤ 300 MPa) at -12°C. However, S values at -18°C were not within the specification limits. It was observed that the S value increased as the diatomite additive ratio increased. When the m values in Table 9 are analysed, it is seen that the specification limit value at -18°C is met only for 5% D3 modification; it is not met for samples with other ratios and control (virgin) asphalt. At -12°C, it was observed that all asphalt binders met the specification limits. When Table 8 and Table 9 are analysed together, it is observed that the S value increases and the m

value decreases as the diatomite additive ratio increases at -12°C. This result shows that modification of diatomite alone is ineffective in the resistance to low temperature cracking.

In a study by Li et al., it was confirmed that diatomite modified asphalt mixtures may weaken the low temperature properties of asphalt mixtures, but their low temperature behaviour can be significantly improved when used with bio-oil [28].

Table 8 - Creep stiffness values of control and diatomite-modified asphalts

Diatomite content (%)	0		5		10		15	
Temperature (°C)	-12	-18	-12	-18	-12	-18	-12	-18
Control (MPa)	118.0	324.1						
D1 (MPa)			121.8	325.7	149.7	353.2	160.5	439.5
D2 (MPa)			122.6	327.2	146.9	353.4	161.3	446.4
D3 (MPa)			124.7	320.1	146.5	349.8	165.1	451.5

Table 9 - Creep rate values of control and diatomite-modified asphalts

Diatomite content (%)	0		5		10		15	
Temperature (°C)	-12	-18	-12	-18	-12	-18	-12	-18
Control (m-value)	0.382	0.283						
D1 (m-value)			0.390	0.275	0.388	0.271	0.381	0.267
D2 (m-value)			0.396	0.291	0.390	0.277	0.382	0.273
D3 (m-value)			0.401	0.305	0.394	0.278	0.388	0.281

3.3. Strength of Mixtures at Low Temperature

The strength of asphalt mixtures at low temperatures was determined by indirect tensile strength test at 0°C. Experimental results are given in Figure 14. The test results showed that increasing the diatomite ratio increased the tensile strength of the modified mixtures. The smallest tensile strengths were obtained with D1 diatomite at a 15% addition rate (2494 kPa). Increasing the diatomite ratio in D1 and D2, diatomite caused a decrease in their tensile strength. Compared to the control mixture, it was observed that 5% diatomite modification reduced the tensile strength of the asphalt mixture, resulting in mixtures that are more sensitive to low temperatures.

Indirect tensile strength (ITS) test is currently the most widely used method to characterise thermal cracking susceptibility in asphalt pavements [58]. When the diatomite ratio was increased to 10%, a 9.7% improvement in the cracking resistance of D3 modified mixtures was observed compared to the control mixtures. Mixtures with D1 diatomite showed lower low temperature resistance than control mixtures. D2 modified mixtures showed tensile strengths equal to or lower than the control mixtures, while D3-modified mixtures showed tensile strengths equal to or higher than the control mixtures.

3.4. Moisture Damage Evaluation

The resistance of the produced diatomite-modified asphalt mixtures to water damage was determined according to the AASHTO T283 method. The indirect tensile strength test was performed on three identical briquettes at 25°C, and the tensile strength values were averaged and given in Figure 15 for unconditioned samples and Figure 16 for conditioned samples.

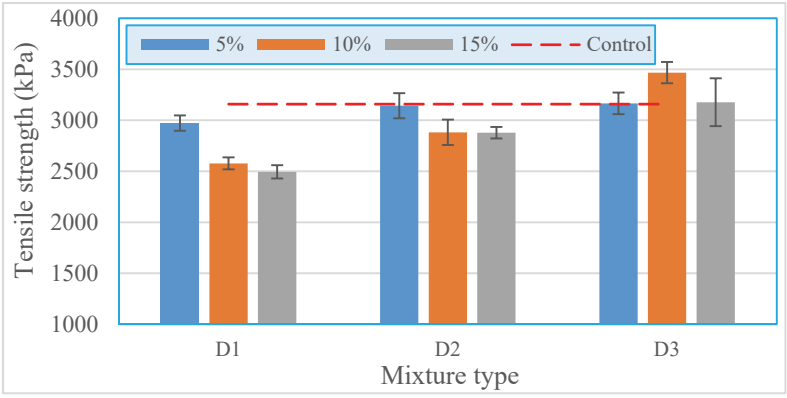

Figure 14 - Comparison of tensile strength of control and diatomite modified asphalt mixes

At 25°C, the tensile strength of diatomite-modified mixtures was generally higher than the control mixture. The conditioned diatomite-modified asphalt mixture samples showed higher tensile strength than the conditioned control samples. In unconditioned samples, D2 diatomite was equivalent to the control mixtures, while D1 and D3 diatomite showed a higher performance than the control mixtures. Increasing the diatomite ratio in the asphalt mixture generally led to a decreasing trend in tensile strength. This trend could be seen more clearly in the conditioned mixtures (Figure 16).

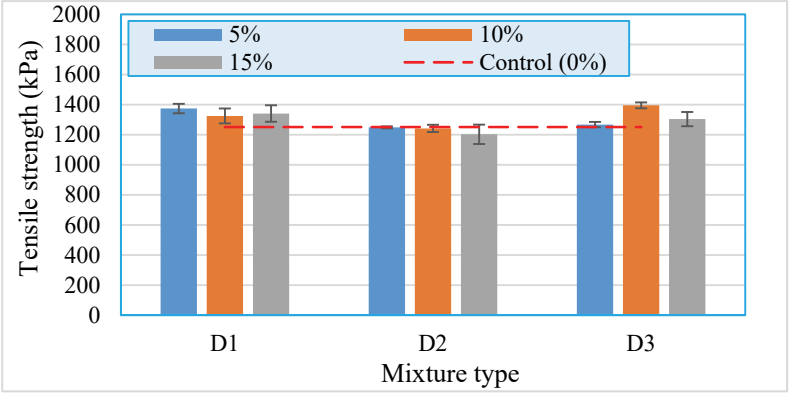

Figure 15 - Tensile strength of unconditioned asphalt mixtures at 25°C

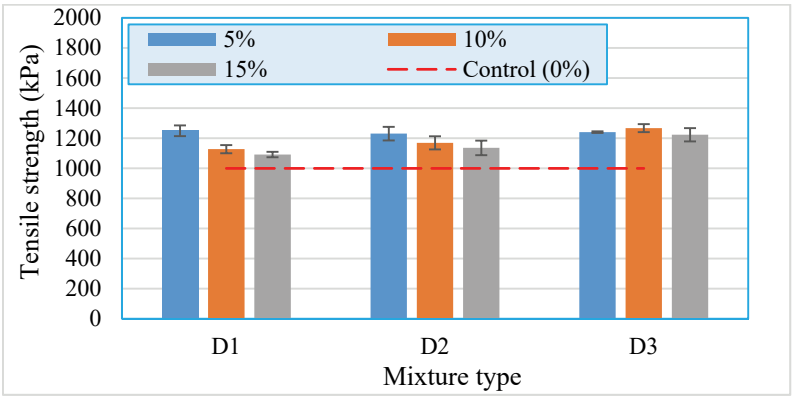

Figure 16 - Tensile strength of conditioned asphalt mixture at 25°C

While higher tensile strengths were obtained in low-concentration modifications (5% inclusion rate), lower tensile strengths were observed in high concentrations (15%). Although there is no significant difference between diatomite types in terms of tensile strength, D3-modified asphalt mixture samples showed the highest tensile strength in both conditioned and unconditioned samples at 10% inclusion rate. In conditioned mixtures, the highest tensile strength was obtained with D3 diatomite and the lowest tensile strength with D1 diatomite at the same inclusion rates. When the conditioned mixtures were evaluated, it was seen that the tensile strength of D3-modified asphalt mixtures increased by 22% or more at all inclusion rates compared to the control mixtures. This increase remained at 13% in D2-modified asphalt mixtures.

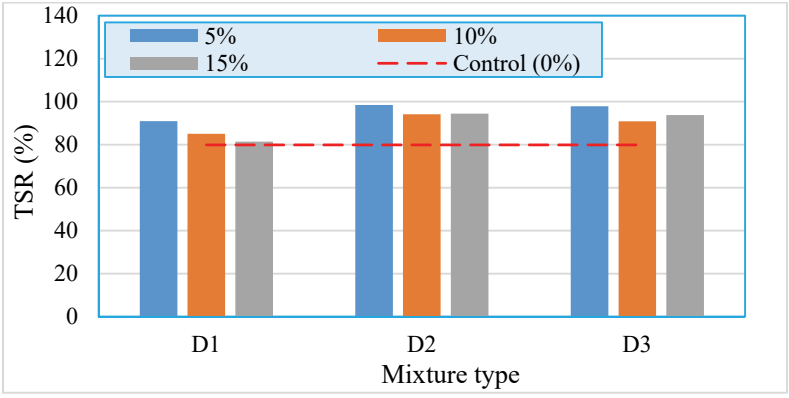

Figure 17 - Tensile strength ratio

The tensile strength ratios of asphalt mixture samples are given in Figure 17. All of the diatomite modified asphalt mixtures showed higher tensile strength than the control mixtures

and 80%. It has been observed that the TSR value of the asphalt mixture can be increased by 22% with diatomite modification. There was a tendency for the water damage resistance of diatomite modified asphalt mixtures to decrease as the diatomite ratio increased. Higher TSR values were obtained at 5% diatomite ratio compared to 10% and 15% adding ratios. D2 and D3 diatomites showed higher water damage resistance compared to D1 diatomite.

3.5. Rutting Evaluation

The rutting behavior of control and diatomite modified asphalt mixtures was investigated by repeated creep tests at 40°C. The deformation curves of unconditioned samples are shown in Figure 18, and those of conditioned samples are shown in Figure 19. It was observed that D3 diatomite showed the highest deformation in unconditioned mixtures and suffered higher deformation compared to the control mixture. As the diatomite inclusion rate increased, the deformation resistance of asphalt mixtures decreased, and the highest deformation resistance was obtained with D1 diatomite at a 5% inclusion rate. With 5% D1 modification, a 17% decrease in permanent deformation was observed compared to the control mixture. It was understood that as the diatomite ratio increased, the slopes in the second region of the creep curves of the asphalt mixture samples increased; however, the tertiary region did not form in any sample in the number of load repetitions applied.

The positive effect of diatomite modification could be better observed in conditioned mixtures. Unlike unconditioned mixtures, as the diatomite ratio increased, the amount of deformation decreased. While the highest deformation resistance was achieved with D2 diatomite at a low inclusion rate (5%), the highest deformation resistance was achieved with D3 diatomite at medium (10%) and high (15%) inclusion rates. With D3 diatomite, a 37% reduction in deformation was achieved compared to the control mixtures at a 15% usage rate.

Considering the experimental results of both unconditioned and conditioned mixtures, it is understood that diatomite modification can have a positive effect on increasing the deformation resistance of asphalt mixtures. Since asphalt mixtures are exposed to natural conditioning under application conditions, the positive effect of diatomite modification in terms of rut resistance may be better revealed. Based on earlier research, it has been confirmed that diatomite can enhance the performance of asphalt mixes at elevated temperatures because of its extensive surface area and porous structure. Furthermore, it can adsorb small amounts of bitumen, leading to an overall increase in the complex shear modulus of the asphalt. This, in turn, enhances the mixture's resistance to rutting [59].

The optimum diatomite content in the modified asphalt mixture rises as the amount of diatomite increases. This is due to the diatomite's capacity to absorb light oil in the asphalt, leading to an increase in the stickiness of the asphalt. The energy required for bending strain encompasses both stress and strain, making it a more appropriate measure for assessing the cold-weather performance of the asphalt mixture. Based on the results of the low-temperature bending test, the most favourable diatomite dosage is achieved at 13-14%. This is when the bending stiffness modulus and bending strain energy reach their peak levels. Considering the equivalent brittle point, the optimum diatomite dosage is 13% [60].

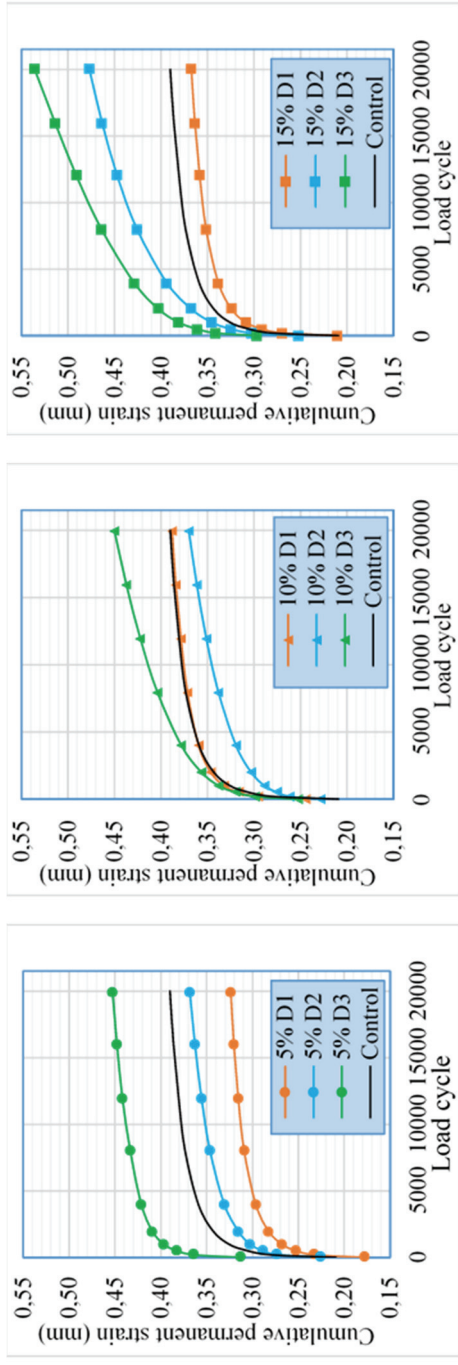

Figure 18 - Creep curves of unconditioned asphalt mixture samples

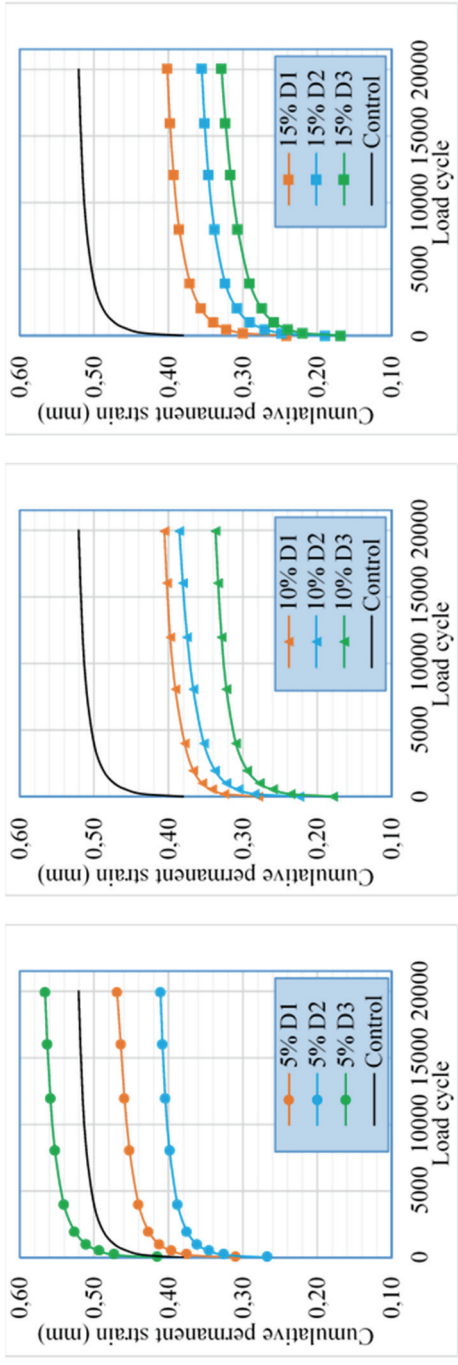

Figure 19 - Creep curves of conditioned asphalt mixture samples

D1, D2, and D3 diatomites used in this study show similar properties in terms of their chemical composition. However, D1 diatomite was ground in the finest gradation, and D3 diatomite was ground in the coarsest gradation. When the mechanical test results of asphalt mixtures are evaluated, it is understood that D2 and D3 diatomites show better results than D1 diatomites. D1 diatomite creates a larger surface area with its fine structure and requires a higher amount of bitumen to cover the particles. The bitumen film around the particles becomes thinner for the same amount of bitumen. The thinness of the bitumen film reduces the flexibility of the mixture and causes harder mixtures to form. It is thought that the lower low-temperature cracking resistance of the D1-modified asphalt mixture is related to the surface area size of the diatomite. As the diatomite ratio increases, the surface area increases, and the tensile strength decreases slightly, confirming this idea.

It is thought that fiber addition may be effective in increasing tensile strength at low temperatures more significantly. The previous studies have emphasized that there is an improvement in the tensile strength of diatomite-fiber modified asphalt mixtures [61]. It is also stated that there is a significant increase in the fatigue life of basalt fiber-diatomite-modified asphalt mixtures compared to diatomite-modified asphalt mixtures [62].

The porous structure of diatomite helps to form a stronger adhesion between the bitumen film and diatomite particles. This strong adhesion increases the asphalt mixture's resistance to water damage. However, when the bitumen film thickness decreases too much, the effect of adhesion may decrease. Therefore, the maximum size and gradation of diatomite have a significant impact in terms of water damage as well as in low temperatures.

When all performance test results are evaluated, it is understood that the use of D3 diatomite in the range of 10-15% provides higher mechanical properties. If thinner form diatomites such as D1 are to be used, the additive ratio should be chosen lower.

It is considered that the ineffective/low-effective results emphasized in the evaluation of low-temperature performances of diatomite-modified asphalt mixtures in previous studies may be related to the gradation of the diatomite used. It becomes clear that the diatomite ratio must be determined meticulously according to gradation.

4. CONCLUSION

The study investigated basic performance indicators such as low-temperature cracking, water damage, and deformation behaviors of asphalt mixtures at different grinding and inclusion rates of diatomite additive. Three grinding sizes and three inclusion ratios were selected. As a result of the study, the following results were obtained.

Increasing the inclusion rate of diatomite negatively affected the low-temperature cracking resistance of the asphalt mixture. This result coincides with a study by Liu et al. [63], which proved that 15% diatomite utilisation rate showed higher cracking resistance than 10%. In general, as the inclusion rate increased, the tensile strength of the asphalt mixture decreased. The increase in the maximum size of diatomite and the coarsening of its gradation positively affected the cracking resistance of the asphalt mixture. The highest tensile strength was obtained with D3 diatomite whose maximum size is 300 microns. However, D1 diatomite-added asphalt mixtures with a maximum size of 106 microns showed lower cracking resistance than the control mixtures.

Diatomite-modified asphalt mixtures showed higher water damage resistance than control mixtures at all sizes and inclusion rates of diatomite additive. Although there is no significant difference, increasing the maximum size of diatomite increased the TSR value. However, increasing the addition rate tended to decrease the TSR value, and the highest TSR values were obtained at a 5% addition rate.

The deformation behaviour of diatomite-modified asphalt mixtures could not be clearly observed in unconditioned mixtures, and misleading results emerged. In conditioned mixtures, high deformation resistance of diatomite modified mixtures was revealed. Increasing the diatomite ratio and maximum size increased the deformation resistance. The highest deformation resistance was achieved at a 15% inclusion rate of D3 diatomite.

This result coincides with the finding of Du et al. [64] on SBS and diatomite modified asphalt mixtures that the temperature stability of the asphalt pavement increased more than the SBS modified ones at an optimum diatomite usage rate of 13% and the rutting resistance of the asphalt pavement improved more.

When all tests are evaluated, it is understood that it would be appropriate to use D2 and D3 diatomites at rates of 10%-15%. In the evaluations made within the scope of the study, it was concluded that the maximum size of diatomite above 200 microns was more effective. In the literature search, no studies on diatomite modified asphalt pavements with different grinding sizes and different types were found.

It is recommended to investigate compatible fiber types, sizes and ratios to improve low temperature cracking. In future studies, the effect of diatomite grind size on fiber-diatomite multiple modification can be investigated. It would also be useful to evaluate the effect of diatomite modification on the fatigue resistance of asphalt and to investigate the effect of surface modified diatomite additives on asphalt pavement performance.

Symbols

D	Diameter of specimen (mm)
D1	First type diatomite
D2	Second type diatomite
D3	Third type diatomite
EDS	Energy dispersive spectrometry
ITS	Indirect tensile strength
NP	Non-plastic
P	Maximum load (N)
PPM	Parts per million
Rpm	Revolutions per minute
SEM	Scanning electron microscopy

SHRP Strategic highway research program

TSR Tensile strength ratio

XRD X- Ray diffractometer

XRF X- Ray fluorescence

Acknowledgments

For their contribution to the material supply in this study; we would like to thank Bentas Bentonite Company. The authors would also like to thank Assoc. Prof. Canan Aksoy for her contribution to this article.

References

[1] U.S. Department of the Interior, Mineral Commodity Summaries 2023, U.S. Geological Survey, Reston, Virginia, USA., 2023.

[2] Cameron., N. G., Diatoms, Encyclopaedia of Quaternary Science (Second Edition), Elsevier, 522-525, 2013.

[3] Jiang, L., Liu, Q. L., Application of Diatomite Modified Asphalt. Applied Mechanics and Materials, 477-478, 959–963, 2013.

[4] Cong, P., Chen, S., Chen, H., Effects of Diatomite on the Properties of Asphalt Binder. Constr. Build. Mater., 30, 495–499, 2012.

[5] Cong, P., Liu, N., Tian, Yu., Zhang, Y., Effects of Long-term Aging on the Properties of Asphalt Binder Containing Diatoms. Constr. Build. Mater., 123, 534–540, 2016.

[6] Cheng, Y., Tao, J., Jiao, Y., Tan, G., Guo, Q., Wang, S., Ni, P., Influence of the Properties of Filler on High and Medium Temperature Performances of Asphalt Mastic. Constr. Build. Mater., 118, 268–275, 2016.

[7] Cheng, Y., Li, L., Zhang, Y., Lv, Z., Zhu C., Quantitative Analysis of Effect and Interaction of Diatomite and Basalt Fiber on Asphalt Performance. J. Mater. Civ. Eng., 31 (12), 04019306, 2019.

[8] Cheng, Y. C., Tao, J. L., Jiao, Y. B., Guo, Q. L., Li, C., Influence of Diatomite and Mineral Powder on Thermal Oxidative Ageing Properties of Asphalt. Adv. Mater. Sci. Eng., 2015, 1-10, 2015.

[9] Wang, H., Li, H., Zhang, H., Zhang, X., Guo, B., Yu, B., Liu, L., Tian, Y., Experimental Study on the Aging Behavior of Modified Asphalt with Different Types of Fine Solid Wastes Under Different Aging Conditions. Constr. Build. Mater., 291, 123308, 2021.

[10] Zhang, P., Guo, Q., Tao, J., Ma, D., Wang, Y., Aging Mechanism of a Diatomite-modified Asphalt Binder Using Fourier-transform Infrared (FTIR) Spectroscopy Analysis. Materials, 12 (6), 988, 2019.

[11] Song, Y., Che, J., Zhang, Y., The Interacting Rule of Diatomite and Asphalt Groups. Pet. Sci. Technol., 29 (3), 254–259, 2011.

[12] Tian, Y., Sun, L., Li, H., Zhang, H., Harvey, J., Yang, B., Zhu, Y., Yu, B., Fu, K., Laboratory Investigation on Effects of Solid Waste Filler on Mechanical Properties of Porous Asphalt Mixture. Constr. Build. Mater., 279, 122436, 2021.

[13] Chen, X. L., Sun, Y. S., Han, Y. X., Zhang, B., The Research on the Performance of Asphalt Mastics Modified by Mineral Fillers. Advanced Materials Research, 158, 287–297, 2010.

[14] Mohd Shukry, N. A., Abdul Hassan, N., Abdullah, M. E., Hainin, M. R., Yusoff, N. I. M., Mahmud, M. Z. H., Putra Jaya, R., Warid, M. N. M., Mohd, Satar, M. K. I., Influence of Diatomite Filler on Rheological Properties of Porous Asphalt Mastic. Int. J. Pavement Eng., 21 (4), 428–436, 2018.

[15] Mohd Shukry, N. A., Hassan, N. A., Abdullah, M. E., Hainin, M. R., Md Yusoff, N. I., Jaya, R. P., Mohamed, A., Effect of Various Filler Types on the Properties of Porous Asphalt Mixture. IOP Conf. Ser.: Mater. Sci. Eng., 342, 012036, 2018.

[16] Aslan, S., Aktas, B., Use of Diatomite and Pumice as Stabilizers in Stone Mastic Asphalt Mixtures. Rev. Constr., 17 (3), 531–541, 2019.

[17] Yi-qiu, T., Lei, Z., Xing-you, Z., Investigation of Low-temperature Properties of Diatomite-modified Asphalt Mixtures. Constr. Build. Mater., 36, 787–795, 2012.

[18] Yang, C., Xie, J., Zhou, X., Liu, Q., Pang, L., Performance Evaluation and Improving Mechanisms of Diatomite-modified Asphalt Mixture. Materials, 11 (5), 686, 2018.

[19] Sun, Y. S., Chen, X. L., Han, Y. X., Zhang, B., Research on Performance of the Modified Asphalt by Diatomite-cellulose Composite. Advanced Materials Research, 158, 211–218, 2010.

[20] Wu, C., Li, L., Cheng, Y., Gu, Z., Lv, Z., Wang, R., Guan, B., Effect of Diatomite and Basalt Fibers on Pavement Performance and Vibration Attenuation of Waste Tires Rubber-modified Asphalt Mixtures. Math. Probl. Eng., 2020, 1–13, 2020.

[21] Jin, J., Tan, Y., Liu, R., Zheng, J., Zhang, J., Synergy Effect of Attapulgite, Rubber, and Diatomite on Organic Montmorillonite-modified Asphalt. J. Mater. Civ. Eng., 31(2), 04018388, 2019.

[22] Wei, H., He, Q., Jiao, Y., Chen, J., Hu, M., Evaluation of Anti-icing Performance for Crumb Rubber and Diatomite Compound Modified Asphalt Mixture. Constr. Build. Mater., 107, 109-116, 2016.

[23] Baldi-Sevilla, A., Montero, M. L., Aguiar, J. P., Loría, L. G., Influence of Nanosilica and Diatomite on the Physicochemical and Mechanical Properties of Binder at Unaged and Oxidized Conditions. Constr. Build. Mater., 127, 176-182, 2016.

[24] Davar, A., Tanzadeh, J., Fadaee, O., Experimental Evaluation of the Basalt Fibers and Diatomite Powder Compound on Enhanced Fatigue Life and Tensile Strength of Hot Mix Asphalt at Low Temperatures. Constr. Build. Mater., 153, 238-246, 2017.

[25] Huang, W. T., Wang, D. Y., He, P. Y., Long, X., Tong, B., Tian, J., Yu, P., Rheological Characteristics Evaluation of Bitumen Composites Containing Rock Asphalt and Diatomite. Appl. Sci.-Basel, 9 (5), 1023, 2019.

[26] Wang, H., Liu, Q., Wu, S., Lv, Y., Wan, P., Gong, X., Liu, G., Study of Synergistic Effect of Diatomite and Modified Attapulgite on Reducing Asphalt Volatile Organic Compounds Emission. Constr. Build. Mater., 400, 132827, 2023.

[27] Tan, B., Su, Y., Fan, Y., Zhang, W., Li, Q., Preparation and Road Performance Study of Rubber–Diatomite Composite Modified Asphalt Mixture. Materials, 16, 7359, 2023.

[28] Li, Y., He, T., Tang, J., Performance Evaluation of Asphalt Binders Incorporating Surface-Modified Diatomite and Bio-Oil: A Value-Added Utilization of Natural Resource. Case Stud. Constr. Mater., e02988, 2024.

[29] Aksoy, A., Aslan, M. T., Iskender, E., Ayyildiz, D., Sengul, C. E., Evaluation of Asphalt Pavement Performance for Different Diatomite Content. Journal of Engineering and Architecture Faculty of Eskisehir Osmangazi University, 31(3), 893-904, 2023.

[30] Highway Technical Specification, General Directorate of Highways, Ankara, (2013).

[31] Zhou, Z., Experimental Study on Mix Design of Diatomite Modified Asphalt Mixture. Master's Thesis, Jilin University, Changchun, China, 2018.

[32] Yin, H. Y., Research on the Modification Mechanism of Diatomite and Dry Mixing of Diatomite-Modified Asphalt Miture. Master's Thesis, Chongqing Jiaotong University, Chongqing, China, 2012.

[33] Guo, Q., Li, L., Cheng, Y., Jiao, Y., Xu, C., Laboratory Evaluation on Performance of Diatomite and Glass Fiber Compound Modified Asphalt Mixture. Mater. Des., 66, 51-59, 2015.

[34] Orhan, F., Bituminous Mixtures Laboratory Studies, Superstructure Development Branch Directorate, General Directorate of Highways, Ankara, 2012.

[35] TS EN 1426, Bitumen and Bituminous Binders - Determination of Needle Penetration, 2015.

[36] TS EN 1427, Bitumen and Bituminous Binders - Determination of the Softening Point - Ring and Ball method, 2015.

[37] Kok, B.V., Yılmaz, M., Akpolat, M., Evaluation of the Conventional and Rheological Properties of SBS+Sasobit Modified Binder. Constr. Build. Mater. 63, 174–179, 2014.

[38] Yaacob, H., Mughal, M. A., Jaya, R. P., Hainin, M. R., Jayanti, D. S., Wan, C. N. C., Rheological Properties of Styrene Butadiene Rubber Modified Bitumen Binder. Jurnal Teknologi, 78 (7–2), 121–126, 2016.

[39] Hunter, R. N., Self, A., Read, J., The Shell Bitumen Handbook. ICE Publishing, London, 2015.

[40] ASTM D6648, Standard Test Method for Determining the Flexural Creep Stiffness of Asphalt Binder Using the Bending Beam Rheometer (BBR), ASTM International, West Conshohocken, PA, USA, 2016.

[41] Lu, X., Isacsson, U. L. F., Ekblad, J., Influence of Polymer Modification on Low Temperature Behaviour of Bituminous Binders and Mixtures. Mater. Struct., 36, 652-656, 2003.

[42] Kumandas, A., Cavdar, E., Sahan, N., Kok, B. V., Pancar, E. B., Oruc, S., Investigation of Rutting and Low Temperature Cracking Behavior of Reactive Ethylene Terpolymer and Waste Cooking Oil Modified Bitumen. Turk. J. Civ. Eng., 35(4), 2024.

[43] AASHTO M 320, Standard Specification for Performance-Graded Asphalt Binder, American Association of State Highway and Transportation Officials, Washington, DC, USA, 2023.

[44] Asphalt Institute, Use of the Delta Tc Parameter to Characterize Asphalt Binder Behavior, State-of-the-Knowledge, IS-240, Asphalt Institute Technical Advisory Committee, Lexington, KN, USA, 2019.

[45] AASHTO T 283-21, Standard Method of Test for Resistance of Compacted Asphalt Mixtures to Moisture-Induced Damage, 2021.

[46] Hoare, T. R., Hesp, S. A., Low-temperature Fracture Testing of Asphalt Binders: Regular and Modified Systems. Transp. Res. Rec., 1728(1), 36-42, 2000.

[47] Ishaq, M. A., Giustozzi, F., Correlation Between Rheological Tests on Bitumen and Asphalt Low Temperature Cracking Tests. Constr. Build. Mater., 320, 21, 126109, 2022.

[48] Fakhri, M., The Effects of Nano Zinc Oxide (ZnO) and Nano Reduced Graphene Oxide (RGO) on Moisture Susceptibility Property of Stone Mastic Asphalt (SMA). Case Stud. Constr. Mater., 15, e00655, 2021.

[49] Hamedi, G. H., Investigating the Use of Nano Coating Over the Aggregate Surface on Moisture Damage of Asphalt Mixtures. Int. J. Civ. Eng., 16, 659-669, 2018.

[50] Hamedipour, A. M., Shafabakhsh, G., Sadeghnejad, M., The Impact of Nano-TiO_2 Particles on the Moisture Susceptibility and Fracture Toughness of HMA under Mixed-Mode I/II Loading and Various Crack Geometry and Temperatures. J. Mater. Civ. Eng., 35(3), 04022444, 2023.

[51] Deb, P., Singh, K. L., Accelerated Curing Potential of Cold Mix Asphalt Using Silica Fume and Hydrated Lime as Filler. Int. J. Pavement Eng., 1-21, 2022.

[52] Yousefi, A. A., Haghshenas, H. F., Underwood, B. S., Harvey, J., Blankenship, P., Performance of Warm Asphalt Mixtures Containing Reclaimed Asphalt Pavement, an Anti-stripping Agent, and Recycling Agents: A Study Using a Balanced Mix Design Approach. Constr. Build. Mater., 363, 129633, 2023.

[53] Delgadillo, R., Nonlinearity of Asphalt Binders and The Relationship with Asphalt Mixture Permanent Deformation. Ph.D. Thesis, University of Wisconsin - Madison, Madison, USA, 2008.

[54] Centeno, M., Sandoval, I., Cremades, I., Alarcon, J., Assessing Rutting Susceptibility of Five Different Modified Asphalts in Bituminous Mixtures Using Rheology and Wheel Tracking Test, Transp. Res. Rec., 08-0705, 2008.

[55] Aksoy, A., Iskender, E., Creep in Conventional and Modified Asphalt Mixtures. Proc. Inst. Civ. Eng. Transp., 161(4), 185-195, 2008.

[56] Tapkin, S., Çevik, A., Uşar, U., Prediction of Rutting Potential of Dense Bituminous Mixtures with Polypropylene Fibers via Repeated Creep Testing by Using Neuro-Fuzzy Approach. Periodica Polytechnica Civil Engineering, 56(2), 253-266, 2012.

[57] BS EN 12697-25, Bituminous mixtures, Test Methods Cyclic Compression Test, 2016.

[58] Krcmarik, M., Characteristics and Prediction of The Low Temperature Indirect Tensile Strengths of Michigan Asphalt Mixtures, Master's Thesis, Michigan State University, USA, 2013.

[59] Yue, Y., Moustafa, A., Dong, L., Ahmed, K., Josephine, M., Tangbing, C., Evaluation of the Properties of Asphalt Mixes Modified with Diatomite and Lignin Fiber: A Review. Materials, 12 (3), 400, 2019.

[60] Zhang, Y. B., Zhu, H., Wang, G., Chen, T., Evaluation of Low Temperature Performance for Diatomite Modified Asphalt Mixture. Advanced Materials Research, 413, 246-251, 2011.

[61] Cheng, Y., Yu, D., Tan, G., Zhu, C., Low-Temperature Performance and Damage Constitutive Model of Eco-Friendly Basalt Fiber–Diatomite-Modified Asphalt Mixture under Freeze–Thaw Cycles. Materials, 11(11), 2148, 2018.

[62] Zhu, C., Luo, H., Tian, W., Teng, B., Qian, Y., Ai, H., Xiao, B., Investigation on Fatigue Performance of Diatomite/Basalt Fiber Composite Modified Asphalt Mixture. Polymer, 14(3), 414, 2022.

[63] Liu, H. B., Liu, H., Wei, H. B., Chai, C., Zhu, B., Laboratory Evaluation on the Road Performance of Diatomite Modified Porous Asphalt Mixture. In Jour. of Phys.: Confer. Seri., 2047(1), 012028. IOP Publishing, 2021.

[64] Du, T., Song, P., Liu, L., Experimental Study on Activated Diatomite Modified Asphalt Pavement in Deep Loess Area. Processes, 10(6), 1227, 2022.

Turkish Journal of Civil Engineering (formerly Teknik Dergi)
Manuscript Drafting Rules

1. The whole manuscript (text, charts, equations, drawings etc.) should be arranged in Word and submitted in ready to print format. The article should be typed on A4 (210 x 297 mm) size paper using 10 pt (main title 15 pt) Times New Roman font, single spacing. Margins should be 40 mm on the left and right sides and 52.5 mm at the top and bottom of the page.
2. Including drawings and tables, articles should not exceed 25 pages, technical notes 10 pages.
3. Your contributed manuscript must be sent over the DergiPark system. (http://dergipark.gov.tr/tekderg)
4. The text must be written in a clear and understandable language, conform to the grammar rules. Third singular person and passive tense must be used, and no inverted sentences should be contained.
5. Title must be short (10 words maximum) and clear, and reflect the content of the paper.
6. Sections should be arranged as: (i) abstract and keywords, (ii) title, abstract and keywords in the other language, (iii) main text, (iv) symbols, (v) acknowledgements (if required) and (vi) references.
7. Both abstracts should briefly describe the object, scope, method and conclusions of the work and should not exceed 100 words. If necessary, abstracts may be re-written without consulting the author. At least three keywords must be given. Titles, abstracts and keywords must be fitted in the first page leaving ten line space at the bottom of the first page and the main text must start in the second page.
8. Section and sub-section titles must be numbered complying with the standard TS1212.
9. Symbols must conform to the international rules; each symbol must be defined where it appears first, additionally, a list of symbols must be given in alphabetic order (first Latin, then Greek alphabets) at the end of the text (before References).
10. Equations must be numbered and these numbers must be shown in brackets at the end of the line.
11. Tables, drawings and photographs must be placed inside the text, each one should have a number and title and titles should be written above the tables and below the drawings and photographs.
12. Only SI units must be used in the manuscripts.
13. Quotes must be given in inverted commas and the source must be indicated with a reference number.
14. Acknowledgement must be short and mention the people/ institutions contributed or assisted the study.
15. References must be numbered (in brackets) in the text referring to the reference list arranged in the order of appearance in the text. References must include the following information:

    If the reference is an article: Author's surname, his/her initials, other authors, full title of the article, name of the journal, volume, issue, starting and ending pages, year of publication.

    Example : Naghdi, P. M., Kalnins, A., On Vibrations of Elastic Spherical Shells. J. Appl. Mech., 29, 65-72, 1962.

    If the reference is a book: Author's surname, his/her initials, other authors, title of the book, volume number, editor if available, place of publication, year of publication.

    Example : Kraus. H., Thin Elastic Shells, New York. Wiley, 1967.

    If the reference is a conference paper: Author's surname, his/her initials, other authors, title of the paper, title of the conference, location and year.

    If the source is a thesis: Author's surname, his/her initials, thesis title, level, university, year.

    If the source is a report: Author's surname, his/her initials, other authors, title of the report, type, number, institution it is submitted to, publication place, year.
16. Discussions to an article published in Turkish Journal of Civil Engineering (formerly Teknik Dergi) should not exceed two pages, must briefly express the addressed points, must criticize the content, not the author and must be written in a polite language. Authors' closing remarks must also follow the above rules.
17. A separate note should accompany the manuscript. The note should include, (i) authors' names, business and home addresses and phone numbers, (ii) brief resumes of the authors and (iii) a statement "I declare in honesty that this article is the product of a genuinely original study and that a similar version of the article has not been previously published anywhere else" signed by all authors.
18. Copyright has to be transferred to UCTEA Turkish Chamber of Civil Engineers. The standard copyright form signed by the authorised author should therefore be submitted together with the manuscript.

CONTENTS

RESEARCH ARTICLE

UCTEA Turkish Chamber of Civil Engineers
TMMOB İnşaat Mühendisleri Odası
Necatibey St. No: 57, Kızılay, Ankara / Türkiye
Tel: +90.312.294 30 00 - Faks: 294 30 88
www.imo.org.tr